

# **A Cylindrically Symmetric, Magnetic Trap for Bose-Einstein Condensate Atom Interferometry Applications**

Robert A. Horne II  
Chesapeake, VA

B.S., Old Dominion University, 2007

A Dissertation presented to the Graduate Faculty  
of the University of Virginia in Candidacy for the Degree of  
Doctor of Philosophy

Department of Physics

University of Virginia  
August, 2015



## ABSTRACT

This dissertation documents a second Bose-Einstein Condensate production apparatus at the University of Virginia. The apparatus produces condensates of  $^{87}\text{Rb}$  atoms to be used as the wave source for atom interferometry experiments. Additionally, a new magnetic trap was developed which provides a harmonic potential with cylindrical symmetry and also supports the atoms against gravity. This trap is based on a time-orbiting potential. To characterize the trapping potential, a condensate was loaded into the trap and perturbed by suddenly changing the confinement field during loading. This had the effect of inducing harmonic oscillations which were measured at varying trap parameters. We expect that this trap will be useful for the implementation of a compact atom interferometer-based gyroscope. Finally, an asymmetric Bragg splitting pulse was developed which allowed for the implementation of two simple interferometers. These interferometers developed a phase which depended on the recoil frequency of  $^{87}\text{Rb}$  and served as a proof of principle for this new apparatus.



## ACKNOWLEDGMENTS

So many people have supported me throughout graduate school and I can honestly say that this dissertation would not have been completed without them. I would like to thank a few of them by name, but in no way is this list exhaustive. Many others have also contributed to this endeavor and for that I am truly grateful.

First, I would like to thank my advisor Professor Cass Sackett, for the many years of his understanding and patient guidance. He has taught me many things throughout my time in grad school, not the least of which was physics. I am eternally grateful for the opportunities he has given me and for the knowledge he has passed along.

I would also like to thank Professors Tom Gallagher, Bob Jones, and Patrick Hopkins for their willingness to serve on my dissertation committee as well as for their feedback on my work. I would be remiss if I did not also thank Professors Lou Bloomfield and Brad Cox for being on my research committee over the years and for their feedback as well.

I am also indebted to my labmates both past and present. I thank John Burke and Jeremy Hughes for helping me get acclimated to the lab. I especially thank Bob Leonard for many years of stimulating conversations and for his early work on the new BEC apparatus. I would like to acknowledge Jiraphat (Joe) Tiamsuphat and Vanessa Leung for their early contributions as well. Tanwa (Oat) Arpornthip for his help in getting the new lab set up and his contributions to the experiment. A special thanks to Eun Oh for the many hours we spent together working on the experiment and for our occasional trips to El Puerto. Thanks also to Adam Fallon, Eric Ihmof, Will Snyder, and Kyle Stolcenberg for their contributions.

I would also like to thank the physics department staff for everything they do to make our lives as grad students easier. I especially want to thank Dawn Shifflett for her encouragement and assistance particularly over the past year. I would also like to thank David Wimer and B.H. Kent from the machine shop for their advice in making some of the parts described in this dissertation. Their knowledge was irreplaceable. I also would like to thank Rick Marshall for being an invaluable resource and for enlightening me to the joys of teaching.

I would like to recognize the support and encouragement of my undergraduate advisor, Professor Charles Sukenik. He opened many doors for me and introduced me to the world of scientific research and atomic physics.

I would also like to thank my friends. They have been a huge support and I honestly wouldn't have made it through this program without them. I especially want to thank Dan Perry and Martin Lehman for sharing the experience of the first two years of grad school together, which I feel will serve to bond us always. I would also like to thank my friends back home for their encouragement in both the good and bad times. I especially want to thank Adam Perry, Jake Dunlow and Jed Sweigart.

Finally, I would like to thank my family. They have always encouraged me to pursue my education and none of this would have been possible without them. Thank you all for always believing in me.

# CONTENTS

<b>Figures</b>	<b>x</b>
<b>Tables</b>	<b>xi</b>
<b>1 Introduction</b>	<b>1</b>
1.1 Interference . . . . .	1
1.2 Interferometry . . . . .	1
1.3 Matter Waves . . . . .	3
1.4 Applications . . . . .	3
1.5 Previous Work . . . . .	6
1.6 Scope . . . . .	12
<b>2 Bose-Einstein Condensation</b>	<b>15</b>
2.1 Experimental Setup . . . . .	16
2.1.1 Vacuum System . . . . .	16
2.1.2 Laser Setup . . . . .	17
2.2 Condensate Production . . . . .	23
2.2.1 Magneto-Optical Trap . . . . .	23
2.2.2 Compressed Magneto-Optical Trap . . . . .	25
2.2.3 Optical Molasses . . . . .	25
2.2.4 Optical Pumping . . . . .	26
2.2.5 Magnetic Trap . . . . .	27
2.2.6 Transfer to Science Cell . . . . .	29
2.2.7 RF Evaporation . . . . .	31
2.2.8 Time-Orbiting Potential Trap . . . . .	32
2.2.9 Imaging . . . . .	35
2.2.10 Condensate . . . . .	36
<b>3 Magnetic Trap</b>	<b>39</b>
3.1 Design . . . . .	40
3.2 Construction . . . . .	48
3.2.1 Coil Chip Production . . . . .	50
3.2.2 Waveguide Support Structure . . . . .	52

---

3.2.3	Electrical Connections . . . . .	55
3.2.4	Thermal Characterization . . . . .	56
3.3	Electronics . . . . .	61
3.3.1	Signal Generation . . . . .	61
3.3.2	Voltage Controlled Current Source . . . . .	64
3.4	Characterization . . . . .	66
3.5	Conclusions . . . . .	70
<b>4</b>	<b>Interferometry</b> . . . . .	<b>71</b>
4.1	Asymmetric Splitting/Recombination . . . . .	71
4.1.1	Theory . . . . .	72
4.1.2	Implementation . . . . .	80
4.1.3	Results . . . . .	84
4.2	Ramsey Interferometer . . . . .	86
4.2.1	Theory . . . . .	88
4.2.2	Results . . . . .	90
4.3	Ramsey-Bordé Interferometer . . . . .	96
4.3.1	Theory . . . . .	97
4.3.2	Implementation . . . . .	102
4.3.3	Results . . . . .	103
4.4	Recoil Frequency Measurements . . . . .	103
4.5	Conclusions . . . . .	105
<b>5</b>	<b>Conclusions</b> . . . . .	<b>107</b>
5.0.1	Future Directions . . . . .	107
<b>A</b>	<b>DB Copper Coil Chip</b> . . . . .	<b>113</b>
<b>B</b>	<b>Waveguide Mechanical Drawings</b> . . . . .	<b>117</b>
<b>C</b>	<b>Magnetic Trap Drive Circuit</b> . . . . .	<b>129</b>
	<b>References</b> . . . . .	<b>145</b>

## FIGURES

1.1	Schematic Representation of an Optical Interferometer . . . . .	2
1.2	Schematic Representation of Atomic Bouncing Experiment . . . . .	7
1.3	Schematic Representation of Gravity Sensitive Interferometer . . . . .	8
1.4	Schematic Representation of Improved Gravimeter . . . . .	10
1.5	Schematic Representation of Gyroscope . . . . .	11
2.1	Vacuum System Schematic . . . . .	17
2.2	Relevant Energy Levels of $^{87}\text{Rb}$ . . . . .	18
2.3	Optical Block Diagram for Saturated Absorption Setup . . . . .	19
2.4	Optical Block Diagram for Laser Setups . . . . .	22
2.5	MOT Setup Schematic . . . . .	24
2.6	Optical Pumping Setup Schematic . . . . .	28
2.7	Transfer Setup Schematic . . . . .	30
2.8	Energy Level Diagram for Evaporative Cooling in DC trap . . . . .	32
2.9	Absorption Imaging Schematic . . . . .	35
2.10	Horizontal Imaging Schematic . . . . .	36
2.11	Condensate Formation . . . . .	37
3.1	AC Bias Field . . . . .	41
3.2	Coil Geometry . . . . .	45
3.3	Trap Frequencies versus Bias Field Strength . . . . .	49
3.4	CAD rendering of Coil Chip . . . . .	51
3.5	Cutaway View of Trap Support Structure . . . . .	54
3.6	CAD rendering of Magnetic Trap . . . . .	54
3.7	CAD rendering of Magnetic Trap Assembly . . . . .	55
3.8	Photograph of Assembled Magnetic Trap . . . . .	57
3.9	Vacuum Flange Feedthrough Connections . . . . .	58
3.10	$R_{X+}$ vs. $T$ . . . . .	59
3.11	Cycled Temperature vs. Time of Waveguide . . . . .	61
3.12	Phase Shifter Circuit Diagram . . . . .	62
3.13	Block Diagram of Waveguide Signal Generators . . . . .	63
3.14	Trap Amplifier Circuit . . . . .	64
3.15	Measured Trap Frequencies . . . . .	70

---

4.1	Energy-momentum Diagram for Asymmetric Split/Recombination Pulse . . .	72
4.2	Split Probabilities . . . . .	78
4.3	Split Pulse Numerical Calculation Results . . . . .	79
4.4	Optical Block Diagram for Bragg Beam Setup . . . . .	81
4.5	Angle Between Bragg Beams at Photo-detector . . . . .	82
4.6	Schematic Representation of Interference Pattern at Dual Photodiode . . . .	83
4.7	Electronics for Driving the Bragg Beam AOMs . . . . .	84
4.8	Atoms After Various Split Pulse Durations . . . . .	86
4.9	Momentum State Populations versus Splitting Time . . . . .	87
4.10	Schematic Representation of a Ramsey Interferometer . . . . .	88
4.11	Ramsey Interference Curves . . . . .	91
4.12	Ramsey Interferometer Visibility versus Interferometer Time . . . . .	95
4.13	Schematic of Ramsey-Bordé Interferometer . . . . .	98
4.14	Energy-momentum Diagram for Asymmetric Reflect Pulse . . . . .	99
4.15	Reflect Pulse Numerical Calculation Results . . . . .	100
4.16	Ramsey-Bordé Interference Curves . . . . .	104
5.1	Schematic Representation of Improved Sagnac Interferometer . . . . .	108
5.2	Schematic Representation of Improved Gravimeter . . . . .	110
5.3	Schematic Representation of Ladder Pulse Sequence . . . . .	111
C.1	Front Panel layout for Magnetic Trap Voltage Generation Box . . . . .	129
C.2	Rear Panel layout for Magnetic Trap Voltage Generation Box . . . . .	130
C.3	Quadrature Sources . . . . .	132
C.4	Control Voltage Buffers and Summing and Difference Amplifiers . . . . .	133
C.5	Multiplier Configuration . . . . .	134
C.6	Output Buffers and Switches . . . . .	135
C.7	Multiplier Noise Spectrum Measurement Setup . . . . .	136
C.8	Multiplier Noise Spectrum . . . . .	137

## TABLES

3.1	Trap Frequency Fit Parameters for Numerical Calculation . . . . .	49
3.2	Coil Chip Impedance Measurements . . . . .	52
3.3	Connections between Vacuum Flange and Waveguide Coils . . . . .	58
3.4	Fitting Parameters for $R_{X+}$ vs. $T$ . . . . .	59
3.5	Fitting Parameters for Temperature vs. Time of Waveguide . . . . .	61
3.6	Uncompensated Trap Signal Impedance Measurements . . . . .	65
3.7	Waveguide Phase Compensated Impedance Measurements . . . . .	65
3.8	Trap Loading Sequence . . . . .	69
3.9	Trap Frequency Fit Parameters . . . . .	70
4.1	MUX Output Configuration . . . . .	84
4.2	I-Q Modulator Outputs . . . . .	85
4.3	Ramsey Interference Curve Fitting Parameters . . . . .	92
4.4	I-Q Modulator Outputs . . . . .	102
4.5	Ramsey-Bordé Interference Curve Fitting Parameters . . . . .	104
C.1	Magnetic Trap Voltage Generation Box Potentiometer Adjustment Key . .	130
C.2	Card Edge Connections . . . . .	131



# 1 | INTRODUCTION

## 1.1 Interference

Interference is a well-known property of waves. Nearly everyone is introduced to this concept early on in one form or another. Waves are so ubiquitous that it would be almost impossible to avoid noticing interference as it applies to waves on a string, water waves, electromagnetic waves, and even sound waves. How waves interfere depends on their phase relation. If two waves are said to be in phase, they will interfere constructively and add together. If, on the other hand the two waves are out of phase, then they would destructively interfere and cancel each other out. In general though, the way that the waves interfere can be complicated and lead to interference patterns like the colored patterns of light reflecting off a puddle with a thin film on top of it. A device used to measure these patterns is known as an interferometer.

## 1.2 Interferometry

One possible application of interference is interferometry. The goal is to learn something about the waves or the environment that the waves traverse by observing the interference pattern produced. To glean an understanding of how this might be used we can consider a simple optical interferometer as shown in figure [1.1](#)

In this interferometer, a laser is used as the light (wave) source. The laser then hits

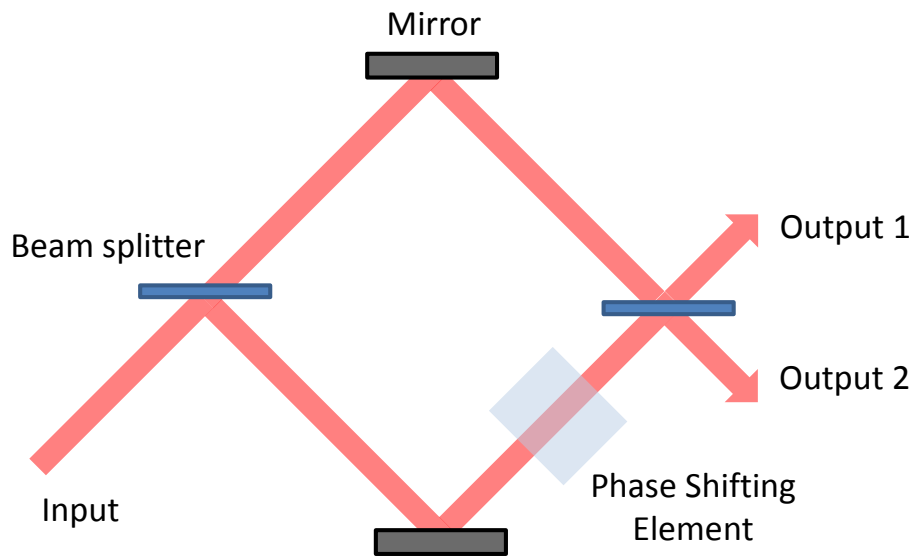


**Figure 1.1: Schematic Representation of an Optical Interferometer.**

a 50-50 beamsplitter, such that half of the input power is sent into both branches of the interferometer. Each path is reflected by a mirror such that the two beams hit a second 50-50 beamsplitter, which acts as a recombiner. There will be two outputs of the interferometer and the intensity of the outputs will depend on the relative phase difference between the two paths. Typically, the output intensity follows the form  $I/I_0 = (1/2)[1 + \cos(\phi + \phi_0)]$  where  $I$  is the intensity of one of the outputs,  $I_0$  is the maximum output intensity and  $\phi$  is the relative phase difference between the two paths and  $\phi_0$  is an offset phase. Therefore, by measuring the intensity of one (or both) of the outputs, the phase difference can be determined.

If an optical element is placed into one of the beam paths, such as a piece of glass, or a cell containing some unknown gas, then the phase difference measured will correspond to the phase shift due to that element. Thus, measuring the phase will tell us something about the element that has been placed into the path. In fact, because light travels at a different speed inside the element, the phase is proportional to the index of refraction,  $n$ ,

of the element, i.e.  $\phi = (2\pi/\lambda)(n - 1)L$ , where  $\lambda$  is the wavelength of the light and  $L$  is the length of the optical element. This method can therefore be used to measure the index of refraction of the element.

### 1.3 Matter Waves

In 1924, Louis de Broglie proposed that matter can behave as a wave and that the wavelength of a particle is inversely proportional to its momentum, i.e.  $\lambda = h/p$  [1]. A consequence of this proposal is that matter interferes in a similar way to light. In fact, matter wave interference was first observed directly by Davisson and Germer using an electron beam to study electron diffraction from a crystalline solid [2]. Work followed shortly thereafter demonstrating that atoms could also exhibit wave-like properties. In 1930, Estermann and Stern observed diffraction of helium atoms from a crystalline solid [3]

It wasn't however until the 1990's that atoms were used as a source for interferometers. This is largely because good mirrors and beamsplitters had not yet been developed. During the preceding years, atom optics were developed using nanofabricated mechanical transmission gratings [4] as well as optical standing waves to act as coherent beamsplitters [5]. These technologies were then applied to create early atom interferometers [6, 7, 8]. All of these interferometers share a common thread. They all used atoms from a thermal beam as their source. With the advent of laser cooling and trapping, atoms were able to be sourced with much narrower momentum spread. The first interfering Bose-Einstein Condensates were produced by Wolfgang Ketterle's group at MIT [9].

### 1.4 Applications

One question that springs to mind when discussing atom interferometers is: what is the benefit to using atoms instead of light? The simple answer is that atoms interact more strongly with their environment. Light is not directly affected by accelerations or by electromagnetic

fields (photons are mass-less and charge-less). On the contrary, atoms do interact strongly with these fields. Furthermore, by using atoms as the wave source for an interferometer, it is possible to gain some understanding of the atoms themselves.

If atoms are used instead of photons for the wave source of the interferometer, then the output intensity corresponds to the number of atoms detected. As such, the fraction of atoms in a given output path varies by  $I/I_{tot} = N/N_{tot} = (1/2)[1 + \cos(\phi)]$  where  $N_0$  is the number of atoms in the output path,  $N_{tot}$  is the total number of atoms in all output paths,  $\phi$  is again the relative phase difference between the two paths of the interferometer and  $\phi_0$  is an offset phase. For light, the phase difference can be thought of as an optical path length difference. For atoms however, the phase developed along each path is given by the quantum phase as shown in equation 1.1.

$$\phi = \frac{1}{\hbar}S = \frac{1}{\hbar} \oint_P \mathcal{L} dt \quad (1.1)$$

Here  $S$  is the classical action,  $\mathcal{L}$  is the classical Lagrangian, and  $P$  represents the classical path of the atom wave [10]. It should be clear that the phase difference is dependent on the energy differences between the two paths. This leads to many fruitful applications which will be discussed here briefly. For a more thorough examination of the applications and a nice primer on atom interferometry in general, I would refer the reader to the review by Cronin et. al. [11].

### Magnetic Gradiometry

If the atoms are prepared in a magnetically sensitive state such that the magnetic moment,  $\mu \neq 0$ , then if the two arms of the interferometer pass through different magnetic field strengths, a phase difference will develop due to the Zeeman effect.

### Gravimetry

If the interferometer is subject to gravity, and the two arms are oriented such that one is above the other, thereby creating a gravitational potential energy difference between the two arms, then the relative phase difference will be dependent upon the acceleration due to gravity. Atom interferometers have been implemented in atomic fountain configurations to measure gravity to great precision [12, 13, 14]

### Gravity Gradiometry

By making two interferometers, separated along the direction that gravity acts, a gradient measurement of the acceleration due to gravity can be performed. This has been demonstrated by measuring the gravity gradient of Earth [15] as well as for measuring the Newtonian gravitational constant,  $G$  [16]

### Accelerometry

By the same means that a gravity measurement would work, atoms in an accelerating interferometer will also develop a phase difference between the two paths that depends on the size of that acceleration.

### Rotation Sensing

Although not at all obvious, if the interferometer arms enclose an area, then the phase difference between the two paths will be given by the Sagnac phase shown in equation 1.2.

$$\phi = \frac{2m}{\hbar} \boldsymbol{\Omega} \cdot \mathbf{A} \quad (1.2)$$

where  $m$  is the mass of a single atom used in the interferometer,  $\boldsymbol{\Omega}$  is the rotation rate of the interferometer, and  $\mathbf{A}$  is a vector with a magnitude equal to the area enclosed by the

interferometer arms and normal to the area enclosed [10]. In fact, atom interferometers in a rotation sensing configuration have been used to make precision measurements [17].

### Geophysics

By applying the ability to measure the acceleration of gravity to the Earth, local studies of the Earth's gravitational field can be performed. Additionally, very precise measurements of the Earth's rotation rate and gravity can be performed and linked to geophysical phenomena such as tides [14].

### Inertial Navigation

By combining precision accelerometers and gyroscopes with a known initial position, the position of the interferometers can be calculated using simple kinematic models.

## 1.5 Previous Work

Previously in our lab, another condensate interferometer was developed [18, 19]. In this apparatus, we obtain condensates of approximately  $10^4$   $^{87}\text{Rb}$  atoms in a linear magnetic trap. By linear, I mean that the trap is harmonic with tight confinement in two directions (y and z) and very weak confinement along the x direction. It is worth noting that the z direction opposes gravity. Prior to making the condensate the atoms are prepared in a magnetically trappable state.

This trapping potential was selected because it allows for large separation of the atomic packets in the interferometer ( $\approx 1$  mm). Therefore, it is easier to apply a potential to one packet at a time, such as a laser pulse to apply an energy shift, or a barrier along one side of the interferometer to produce surface interactions. While this geometry is convenient for some measurements, it provides limitations for others.

To motivate the development of a new magnetic trap, I will discuss two experiments in particular.

### Gravimetry

Jeremy Hughes' dissertation focused on the implementation of a gravimeter [20, 21]. As a first experiment, he made an atomic trampoline in which the atoms were released from the linear magnetic trap operating with frequencies of 7.4, 0.8, and 4.3 Hz for x, y, and z respectively. After the atoms were allowed to fall under the acceleration due to gravity, a pulse from two counter-propagating laser beams was used to reflect (or bounce) the atoms via Bragg scattering. The first order process involves the absorption of a photon from one of the beams followed by the stimulated emission into the other, thereby resulting in a momentum transfer of  $2\hbar k$  to the atoms, where  $k$  is the wavenumber of the lasers used. By applying many of these reflect pulses in sequence, a measurement of gravity could be made by adjusting the repetition rate of the pulses and extracting from that the acceleration due to gravity. This bouncing experiment is shown schematically in figure 1.2.

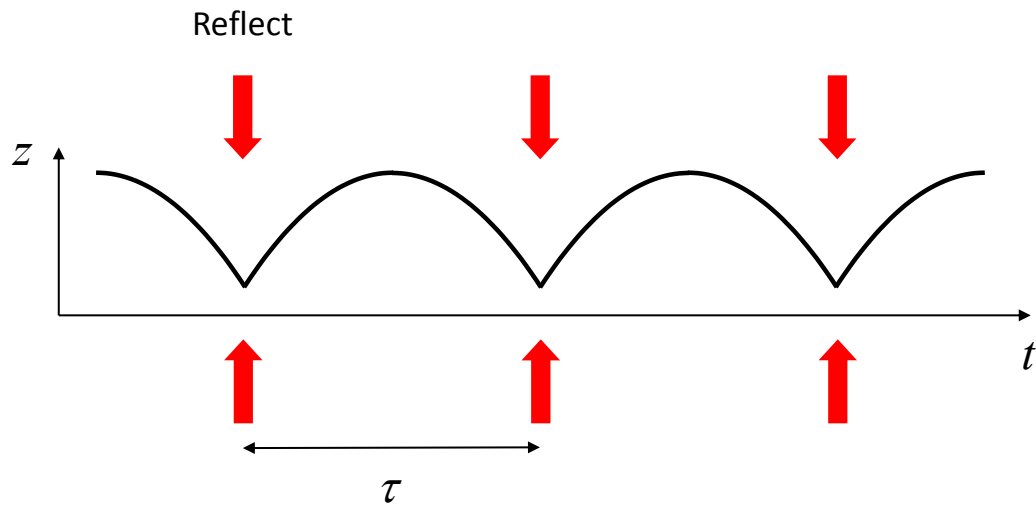


Figure 1.2: Schematic Representation of Atomic Bouncing Experiment

The atoms were able to be suspended for up to 100 ms which resulted in a measurement of the acceleration due to gravity of  $g = 9.814 \pm 0.008 \text{ m/s}^2$  after corrections, which is within error of the average value of  $g = 9.81 \text{ m/s}^2$ .

Modeling of the reflect operation was performed and it was determined that the atoms should have been able to remain suspended for nearly ten times longer. There are several possibilities that would explain the difference. First, since the atoms are strongly confined in one of the directions transverse to gravity they expand much more rapidly along that direction. This could cause issues where the atoms expand to become large compared to the beam waist used for the reflect pulses ( $\approx 1 \text{ mm}$ ). Furthermore, if the trapping potential were more symmetric, then the cloud would be more uniform to begin with. This provides some motivation to develop a cylindrically symmetric trap as well as to use a larger beam waist.

As an additional experiment a gravity sensitive interferometer was made by using reflect pulses to create the interferometer configuration shown in figure 1.3.

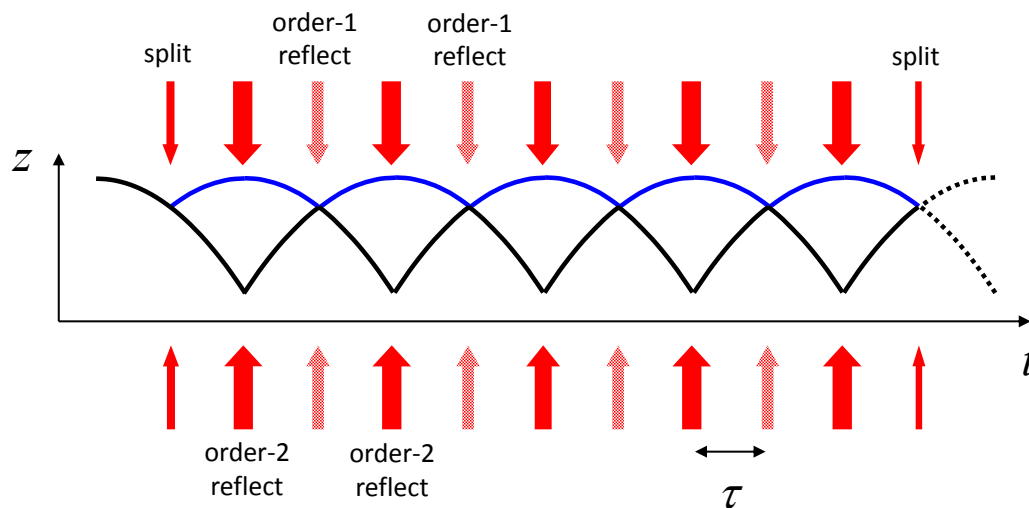


Figure 1.3: Schematic Representation of Gravity Sensitive Interferometer

In this configuration the atoms are separated vertically and undergo free fall between the laser pulses. To implement this configuration two types of reflect pulses were required. An order-1 reflect caused atoms moving with momentum  $\pm\hbar k$  to receive a kick of  $2\hbar k$  opposing their motion. An order-2 reflect gave atoms moving with  $-2\hbar$  an upward kick of  $4\hbar k$  while not impacting atoms at rest. The duration and intensity are different for the two reflect pulses which allows for selection between the two transitions. The phase difference developed during a single cycle (when the atoms come back together) is given by equation 1.3.

$$\phi = \frac{\hbar k}{m}(4k\tau + 2\gamma\tau^2) + \phi_{r1} + \phi_{r2} \quad (1.3)$$

where  $k$  is the wavenumber of the lasers used in the reflect pulses,  $2\tau$  is the duration of one cycle,  $\gamma \equiv mg/\hbar$ ,  $\phi_{r1}$  is the phase shift due to reflect pulse type 1 and  $\phi_{r2}$  is the phase shift due to reflect pulse type 2. The output of the interferometer was measured by looking at the fraction of atoms ( $N_+/N$ ) coming out moving with speed  $+\hbar k$  which is given theoretically by equation 1.4.

$$N_+/N = \sin^2[(n\phi + \phi_s)/2] \quad (1.4)$$

where  $\phi$  is the phase from a single cycle (1.3),  $n$  is the number of cycles, and  $\phi_s$  is the phase shift due to the recombination pulse at the end of the interferometer. The phase shift due to the reflect pulses was determined from a model of the pulse sequences. Because this uncertainty adds up for all of the cycles in the interferometer it leads to the largest source of error in the measurement of the acceleration due to gravity. the resulting measurement of the acceleration of gravity was  $g = 9.745 \pm 0.027 \text{ m/s}^2$ .

One solution to reduce the uncertainty caused by these reflect pulses would be to implement an interferometer that is more symmetric, such that both arms are effected more or less the same by the total pulse sequence. A possible implementation which would correct for this is shown in figure 1.4.

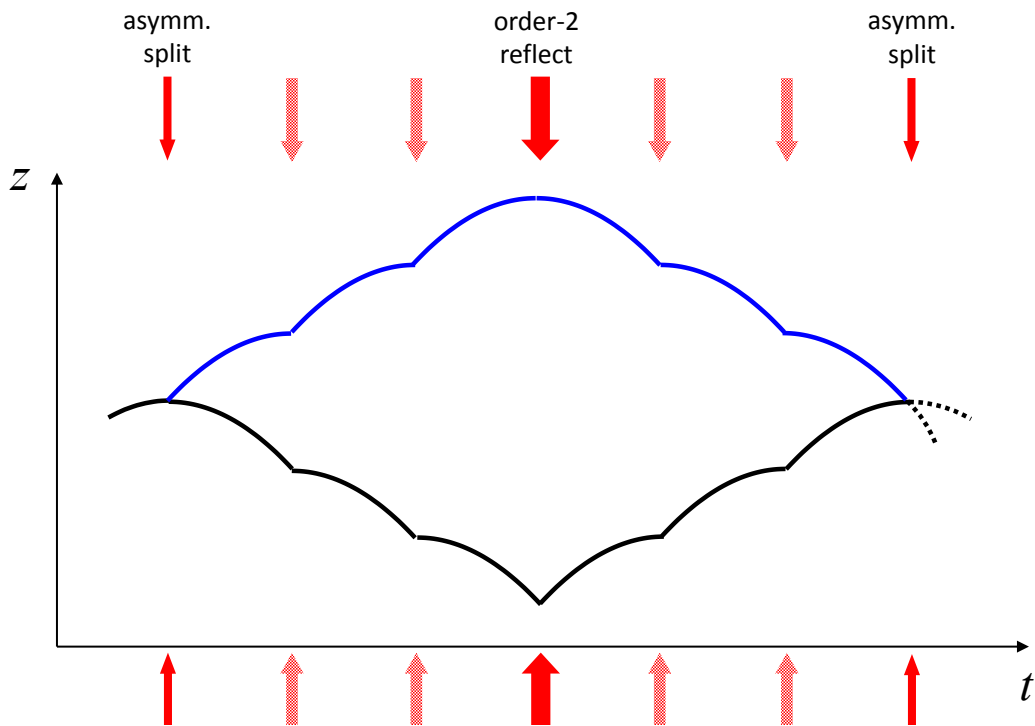


**Figure 1.4: Schematic Representation of Improved Gravimeter**

In this case, there is also the added benefit of providing larger packet separation for the same interferometer time. Furthermore, this implementation requires the ability to asymmetrically split the atoms and provides much of the motivation towards developing that capability, which is discussed in detail in Chapter 4.

## Gyroscope

The second most relevant experiment to this dissertation was a gyroscope implemented in the linear magnetic trap operating with frequencies of 6.0, 1.1, and 3.3 Hz for  $x$ ,  $y$ , and  $z$  respectively. This experiment, performed by Burke et. al. [22], required that the two paths in the interferometer enclosed an area. To do this in the linear trap, motion was excited in the transverse direction ( $x$ ) by electronically moving the trap center suddenly and returning it to its original location after an appropriate delay. This caused the atoms to oscillate in

the x direction. The atoms were then split using a pulse from an optical standing wave via Bragg scattering. This interferometer is represented schematically in figure 1.5.

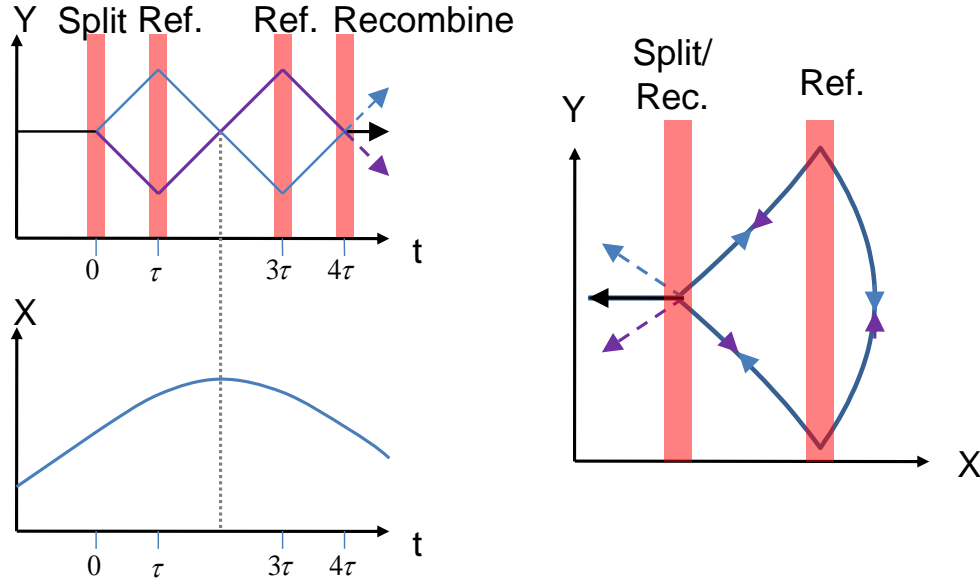


**Figure 1.5: Schematic Representation of Gyroscope.** Oscillations were induced in the x direction and then the Bragg operations took place along the y direction. The result was a small enclosed area.

This experiment was able to enclose an area of  $0.1 \text{ mm}^2$ ; however, due to coherence time limitations, the small area enclosed, and the extremely slow rotation rate of the platform being used (Earth), phase shifts from rotation were unable to be observed.

It should be clear from the Sagnac phase described in equation 1.2 that this implementation is not ideal for a highly sensitive gyroscope. The area is maximized for a given interferometer path length (and therefore interferometer time) when the area enclosed is circular. This is the motivation for creating a cylindrically symmetric trapping potential as it would allow for just such an experiment.

## 1.6 Scope

The scope of this dissertation will be to document the experimental apparatus for the second BEC based atom interferometer in our lab. This will be broken down into four chapters:

### **Chapter 2 - Bose-Einstein Condensate**

This chapter will document the apparatus and the steps we use in creating Bose-Einstein Condensates (BEC) of  $^{87}\text{Rb}$ , which will be used for interferometry experiments.

Section 2.1 - Experimental Setup: This section discusses the hardware used for producing our condensates including the vacuum system setup and the laser setups.

Section 2.2 - Condensate Production: This section focuses on the experimental steps used for cooling and trapping our  $^{87}\text{Rb}$  atoms, culminating in the production of a Bose-Einstein Condensate for use as the atomic source in our interferometer.

### **Chapter 3 - Magnetic Trap**

This chapter will document the design and construction of the magnetic trap used to confine the atoms during the atom interferometry experiments as well as provide support against gravity.

Section 3.1 - Design: This section focuses on the actual design of the magnetic trap. The fields used to create a cylindrically symmetric trap are discussed and the resulting potential which the atoms are confined is calculated.

Section 3.2 - Construction: This section focuses on the mechanical and electrical construction of the magnetic waveguide and the support structure to which it is mounted inside of the vacuum chamber. This section additionally details the thermal performance for the waveguide structure.

Section 3.3 - Electronics: This section details the implementation of the electronics used to provide the necessary currents to each of the coils of the waveguide.

Section 3.4 - Characterization: This section discusses how the trap was characterized by measuring the gradient and bias field strengths. Additionally, the results of measurements

of the trap frequencies are presented as a function of bias field strength.

### **Chapter 4 - Interferometry**

This chapter will detail the first interferometry experiments performed with the cylindrically symmetric magnetic trap. All of these experiments utilize the phase locking apparatus developed by Eun Oh [23].

Section 4.1 - Asymmetric Splitting/Recombination: This section discusses a brief overview of the theory behind asymmetric Bragg splitting and recombination. Additionally, a brief overview of the instrumentation used to create the Bragg beams for this operation are discussed. Finally, the results of the asymmetric splitting operation are presented and discussed.

Section 4.2 - Ramsey Interferometer: This section discusses the simplest interferometer that we were able to create. This uses only the asymmetric splitting and recombination pulses developed in the previous section. The basic theory is discussed and the resulting interference patterns are presented and analyzed.

Section 4.3 - Ramsey-Bordé Interferometer: This section discusses another interferometer that we used. This is similar to the Ramsey interferometer, but it adds one or more reflection pulses between the two pulses of the Ramsey interferometer. The theory for the reflection pulse is discussed followed with a brief discussion of how this pulse was implemented. Finally, the interference patterns which were observed are presented and analyzed.

### **Chapter 5 - Conclusions**

This chapter summarizes the results of all of our experimental results to date in the second BEC interferometer apparatus. Additionally, future experiments are discussed.



## 2 | BOSE-EINSTEIN CONDENSATION

Bose-Einstein statistics were first theorized for photons by Satyendra Bose in 1924 in collaboration with Albert Einstein to explain Planck's law. This theory was then extended upon by Einstein in 1925 to develop the theory of Bose statistics for massive particles. Bose-Einstein condensation is the result of the Bose-Einstein statistics for integer spin particles and shows up in many areas of physics, ranging from superfluidity to superconductivity [24, 25].

While Bose-Einstein condensation (BEC) was predicted for massive bosons in the 1920's, it took nearly three-quarters of a century for it to be realized experimentally. Historically, much of the effort was placed on hydrogen, but the first condensates were actually made with other hydrogen-like atoms (Rubidium [26], Sodium [27] and Lithium [28, 29]). The reason for this was due to the advances made during the 1980's and 90's for laser cooling and trapping of neutral atoms. This allowed for a room temperature gas of these alkali elements to be cooled down significantly; however, evaporative cooling was still required to remove enough energy from the atomic cloud for a condensate transition to occur.

The basic condition for Bose-Einstein condensation is that the interatomic spacing has to be smaller than the wavefunction of the individual atoms. A rough estimate can be obtained from the following expression

$$\lambda_T = \frac{h}{(2\pi mkT)^{1/2}} \quad (2.1)$$

It is well known that the onset of Bose-Einstein Condensation, which occurs when a significant fraction of the atoms occupy the ground state, happens when the phase space density

reaches a critical value of  $\rho_c = n\lambda^3 \geq 2.612$ , where  $n = N/V$  is the spatial density,  $N$  is the number of particles and  $V$  is the volume [24]. To increase the phase space density, the spatial density needs to be increased while the temperature of the ensemble is decreased. This chapter will discuss how we accomplish this task with our apparatus.

## 2.1 Experimental Setup

I begin the discussion of how we make BEC with the experimental apparatus that we used. We must perform our experiments in a vacuum chamber and we utilize lasers to manipulate the atoms. I will discuss both of these in turn.

### 2.1.1 Vacuum System

Our experiment revolves around our ability to work with neutral  $^{87}\text{Rb}$ . To perform these experiments we must isolate the gaseous rubidium atoms from background elements. We achieve this by performing our experiments in an ultra-high vacuum cell. This cell is split into two regions, a low pressure region where the atoms are first collected in the Magneto-Optical Trap (MOT), we refer to this section of the chamber as the MOT cell, and another region where BEC is produced and atom interferometry experiments are performed, which we call the science cell. These two regions are separated by a long, narrow tube which allows for a pressure differential to develop between the two regions. This setup is shown schematically in figure 2.1.

In the MOT cell, we include Rb dispensers from SAES. We can therefore supply rubidium vapor to the MOT cell by running current through the dispensers. This acts as the source of rubidium for the MOT and in turn the condensate. Additionally, the MOT cell has an ion gauge for pressure measurement and an ion pump to maintain the pressure in the cell.

In the science cell, we include the magnetic trap needed to produce a condensate along with an antenna to allow for RF evaporation of the atoms. The science cell also has it's

own ion gauge and ion pump as well as a set of titanium sublimation pump filaments.

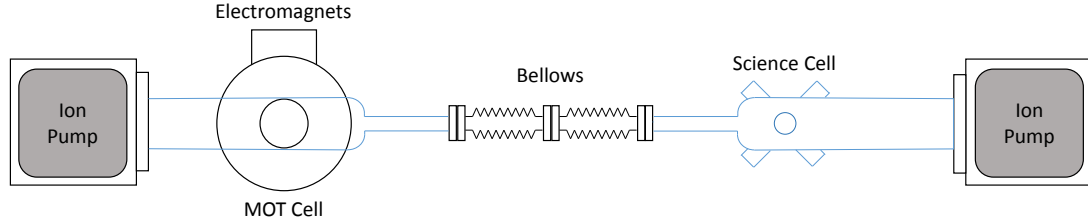


**Figure 2.1: Vacuum System Schematic.** The vacuum system consists of two sections separated by a long, narrow tube allowing for a differential pressure to develop between the two sections. Each section has its own ion pump and pressure gauge. The rubidium is sourced in the MOT cell.

Before installing the vacuum chamber into the optical setup, the entire system was baked in a home-built oven to 250 °C. This serves the purpose of reducing the ultimate pressure attainable in the chamber by essentially boiling contaminants (mostly water) off of the internal surfaces of the vacuum chamber while being pumped out by an external pumping station. Before allowing the chamber to cool it was sealed off to prevent diffusion of contaminants back into the chamber. Additionally, baking the chamber allows for the ultimate pressure to be reached in a shorter time. After the vacuum cell was installed onto the optical table, the typical operating pressures in the two regions are approximately  $10^{-9}$  torr in the MOT cell and  $5 \times 10^{-11}$  torr in the science cell.

### 2.1.2 Laser Setup

With the vacuum chamber in place we need a way to manipulate the atoms for our purposes. As with many atomic physics experiments, we utilize lasers for this task. The relevant energy levels of  $^{87}\text{Rb}$  are shown in figure 2.2.

To establish a Magneto-Optical Trap (MOT) it is necessary to have a cycling transition. In other words, a transition that when atoms absorb a photon the atoms will spontaneously decay back to the initial state they were in before the photon absorption. The cooling beam

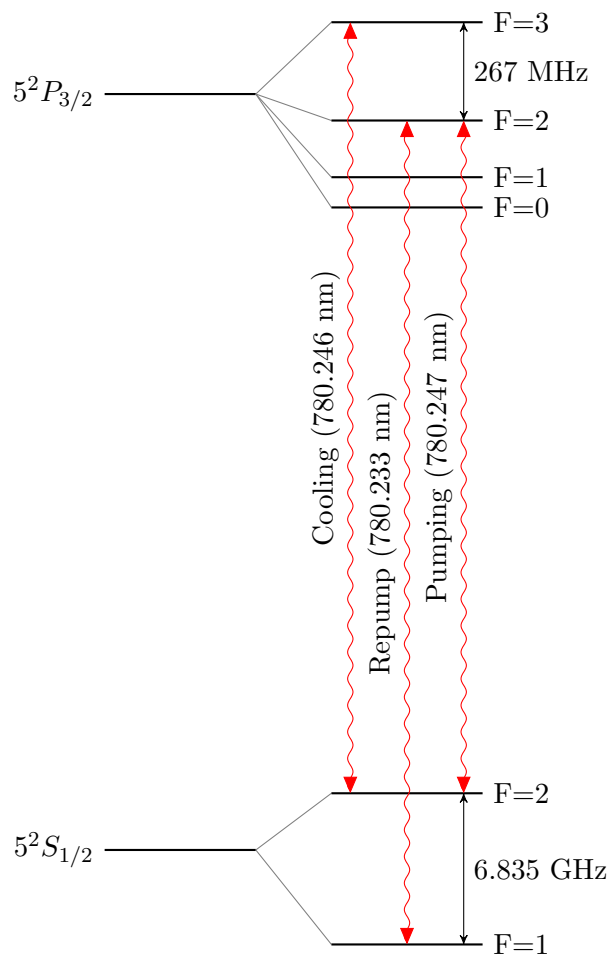


**Figure 2.2: Relevant Energy Levels of  $^{87}\text{Rb}$ .** The wavelengths of each transition are shown along with the relevant hyperfine splitting. Data from [30].

used in the MOT operates on one such cycling transition, i.e. between the  $5^2S_{1/2, F=2}$  and the  $5^2P_{3/2, F=3}$  energy levels. There does however exist a small probability the atoms will be excited by the cooling beam to the  $5^2P_{3/2, F=2}$  state, which can then decay down to the  $5^2S_{1/2, F=1}$  state. This state is dark to the cooling beam. Therefore, a second repumping laser is required to pump the atoms out of the dark state. This repumping laser operates between the  $5^2S_{1/2, F=1}$  and the  $5^2P_{3/2, F=2}$  energy levels. Additionally, a laser is required operating between the  $5^2S_{1/2, F=2}$  and the  $5^2P_{3/2, F=2}$  energy levels to be used in the optical pumping stage of condensate production, which will be discussed in more detail in section

2.2.4. Finally, one more laser is required to image, or probe, the atoms. Prior to the imaging step of the experiment, the atoms are prepared in the ground state  $5^2S_{1/2, F=2}$ . We utilize absorption imaging and therefore use a beam near-resonant with the same transition used as the cooling beam in the MOT.

To derive the laser beams necessary for condensate creation we use two main, independent laser heads. A Toptica DL Pro provides the beams for cooling, pumping, and probing the atoms and a distributed feedback diode (DFB) laser acts as the master repump laser. These lasers are both sent into saturated absorption spectrometers which allow their frequencies to be locked to the desired atomic transitions. The saturated absorption lock setups are shown schematically in figure 2.3.

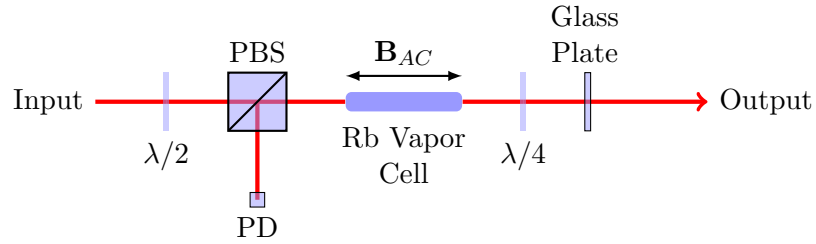


**Figure 2.3: Optical Block Diagram for Saturated Absorption Setup.** The output is sent to a spectrum analyzer and wavemeter for diagnostics. The AC bias field is only present on the DL Pro SA lock. The arrow indicates the magnetic field orientation.

The details of saturated absorption spectroscopy and frequency locking are presented by many sources [31, 32]; therefore, I will not go into the details here. The important thing to note is that a saturated absorption spectrometer yields an absorption signal with Doppler-free absorption peaks corresponding to the atomic transitions as well as cross-over peaks between them. The absorption signal is converted to an electronic signal via a photodiode.

To lock the laser frequency to one of the atomic transitions, we use a lock-in amplifier. This requires that we modulate the saturated absorption signal at a fixed frequency. This modulation allows us to use a phase detection method to produce an error signal which can then be fed back to one of the control inputs which govern the operating frequency

of the laser. For the Toptica laser, we apply an alternating magnetic field that shifts the transition frequencies via the Zeeman effect. This is done to avoid putting spectral noise onto the laser itself. For the DFB laser, we directly modulate the laser injection current. Both of these are modulated at 10 kHz. The resulting signal from each of the locking circuit photodiodes is sent into a phase-detection circuit and an error signal is produced and fed back to the respective laser control circuit. The piezo-electric transducer which adjusts the grating in the Toptica lasers external cavity is used to stabilize its frequency while the injection current is used for that purpose on the DFB laser.

The Toptica DL Pro is fiber coupled and outputs approximately 25 mW of total power. This beam is then split with a fiber-based beam splitter such that 5% is sent to the saturated absorption lock setup and the other 95% is sent to a Toptica BoosTA (Tapered Amplifier) for amplification. Before the 5% beam from the beam-splitter is sent to the saturated absorption setup, it first passes through an Acousto-Optic Modulator (AOM) set up in a double pass configuration. The beam passes through the first time and the first-order diffracted beam is then retro-reflected back through the AOM. There is also a lens in the beam path a focal length away from the AOM to allow the frequency of the AOM to be adjusted with minimal impact on the alignment of the outgoing beam to the saturated absorption lock. A prism is used to reflect the first pass beam to produce a small vertical offset from the incident beam so that the output of the AOM after the second pass through can be separated from the originally incident beam. Again, the first-order diffracted beam is used from the second pass. This results in a total, positive frequency shift of twice the AOM drive frequency. This beam is then sent to the saturated absorption lock setup. As a result of this setup, the DL Pro laser operates red detuned of the locking transition by twice the double-pass AOM drive frequency.

The output from the BoosTA is approximately 1 W of laser light also red detuned of the locking transition by twice the double-pass AOM drive frequency. This beam passes through a telescope with a 10  $\mu\text{m}$  pinhole at the focus, which acts as a spatial filter. The

beam then passes through a mechanical shutter which is used to extinguish all of the light from the laser. Finally, the beam passes through several single pass AOMs to derive the cooling, pumping, and probe beams used in the experiment. The cooling and probe AOM beams come from the positive first-order diffracted beams, while the pumping beam is the negative second-order diffracted beam.

The DFB laser however does not provide the required power to produce a healthy MOT since it only outputs around 15 mW of total power. This is the power directly output from the laser diode and there are substantial losses in the beam path between the laser diode and the MOT. Additionally, we need to expand the beam substantially in order to cover the entire MOT with repump light. This results in a repump intensity at the atoms of about  $0.25 \text{ mW/cm}^2$ . We therefore elected to use the DFB laser to injection lock a higher powered diode laser [33]. To accomplish this, the DFB master has a small portion of the light picked off and sent to the saturated absorption lock. The rest of the beam is then allowed to enter into the cavity of the slave diode laser through its front facet. If there is a lasing mode near this injected light then the slave will be pulled to lase at the same wavelength. This requires that the master laser is aligned well and with enough power coupled into the slave cavity. As a result, we obtain 60 mW of light out of the slave laser locked to the repumping transition. This gives us about  $1 \text{ mW/cm}^2$  repump intensity at the atoms.

To diagnose the effectiveness of injection locking both the master and slave laser are sent into a spectrum analyzer. When the injection locking is working properly, the peaks on the spectrum analyzer from the master and slave lasers fall on top of one another. This also provides a useful way to get the master laser coupled well into the slave laser's cavity. By monitoring the spectrum analyzer signal while adjusting the alignment of the master laser into the slave cavity, or the relative wavelength difference between the two lasers, then the injection locking can be peaked up such that the peak on the spectrum analyzer due to the slave laser is pulled more towards the master laser's peak. This process can be iterated until the peaks coincide. The entire laser setup is shown schematically in figure 2.4.

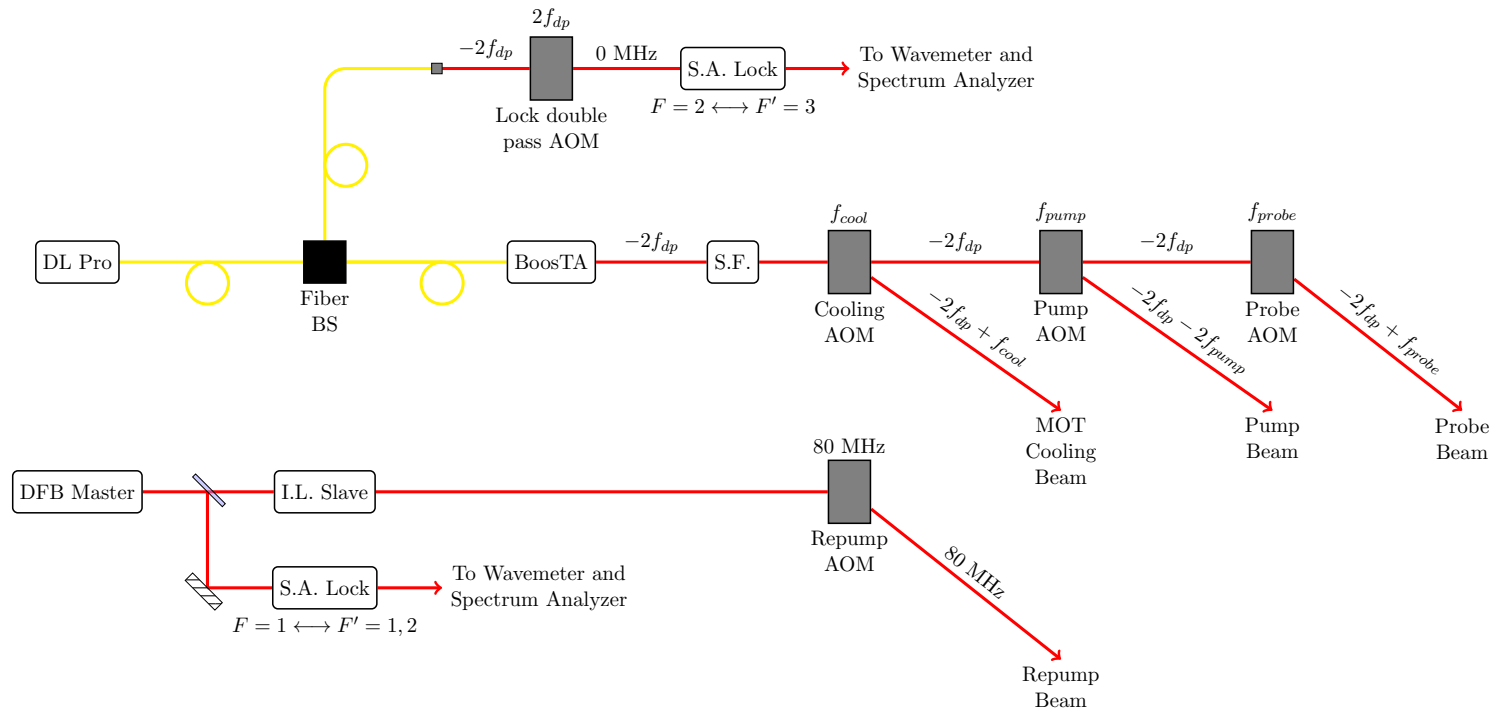


**Figure 2.4: Optical Block Diagram for Laser Setups.** All four laser beams needed for BEC production are derived from these two lasers.

## 2.2 Condensate Production

In our experiment, the road to creating a condensate starts with a Magneto-Optical Trap. In this trap, a large number (about  $10^9$ ) of very cold atoms (about  $150 \mu\text{K}$ ) is collected. The atoms are then prepared in a magnetically trappable internal state so that they can be transferred into a magnetic spherical quadrupole trap, using DC fields. This trap is then physically moved to the location of yet another magnetic trap, this one uses AC fields, and the atoms are cooled a bit and then transferred from the DC trap to the AC trap. After this stage the atoms are still too hot to form a condensate. To reduce the temperature below the critical temperature such that more atoms are in the ground state the atoms are evaporatively cooled. This process results in about  $10^4$  atoms in a condensate. Each step of the process will be elaborated upon in the next few pages.

### 2.2.1 Magneto-Optical Trap

As with many other cold atom experiments, we begin by collecting and cooling atoms in a Magneto-Optical Trap, or MOT. This trap relies on the spontaneous force exerted on the atoms due to scattering of many photons from a laser. The trap is comprised of three orthogonal pairs of laser beams which are detuned from the cooling transition and provide Doppler cooling. In addition to the lasers there are two electromagnets, wired in such a way as to produce a spherical quadrupole magnetic field. This configuration produces a magnetic field that increases in strength from the center of the trap and produces a spatially dependent Zeeman shift to the atomic energy levels. The combination of the Doppler cooling and Zeeman shifts produces three-dimensional cooling and spatial trapping of the atoms at the center of the electromagnets [34]. A schematic representation of the MOT is shown in figure 2.5.

In our MOT, we use six cooling laser beams each with an intensity of approximately  $4.5 \text{ mW/cm}^2$  and a diameter of near 5 cm. Additionally, along two of these beams, we combine

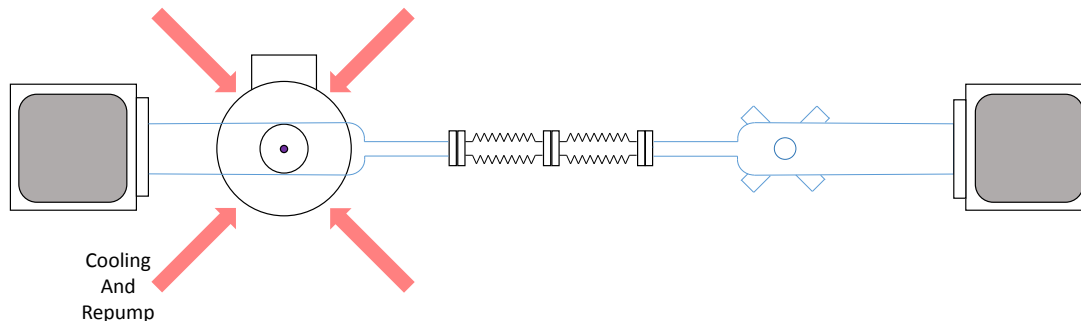


**Figure 2.5: MOT Setup Schematic.** Six laser beams converge on the atoms in the center of the magnetic quadrupole coils. The vertical beams are not shown in the schematic, but pass through the center of the magnet coils along the axis of symmetry. The polarizations are all circular with opposing beams having the same handedness (LHC or RHC). The beams in the horizontal plane and the vertical beams have opposite handedness.

light from the repumping laser with an intensity of approximately  $1 \text{ mW/cm}^2$ . The field gradient applied by the electromagnets is measured to be approximately  $10 \text{ Gauss/cm}$  along  $z$  (vertical direction), which corresponds to the axis of symmetry of the coils.

To measure the performance of the MOT we have two tools. To obtain an approximate number of atoms in the MOT we measure the total fluorescence from the scattered photons of the cooling lasers. This is done by imaging the MOT onto a photodiode. By carefully determining the solid angle collected by the imaging optics and calibrating the photodiode, the number of atoms can be backed out [31]. Additionally, we set up fluorescence imaging in which we imaged the MOT onto a CCD camera and simply took a picture of the MOT. This provided us with a detailed image showing the size and shape of the MOT and also provided us with temperature estimates via time of flight expansion imaging. Using these measurement techniques we find that our MOT collects nearly  $2 \times 10^9$  atoms at about  $150 \mu\text{K}$ .

### 2.2.2 Compressed Magneto-Optical Trap

After loading the atoms into the MOT, the cooling laser detuning is shifted further red from the cooling transition. To accomplish this we adjust the double-pass AOM frequency between the master laser (DL Pro) and the saturated absorption setup.

Detuning the cooling laser has the effect of allowing the photons to penetrate deeper into the atomic cloud. This improves cooling and results in a smaller atomic cloud. This allows for better matching of the MOT to the upcoming magnetic trap. To optimize this process in our experiments the configuration was varied and the configuration which produced the most and coldest atoms was determined empirically. We find that the largest number of the coldest atoms are obtained when we shift the detuning as far as possible from the cooling transition. We find that this is -60 MHz, which is the furthest that the double-pass AOM can be driven while maintaining enough laser power in the saturated absorption setup to remain locked to the cooling transition. Additionally, the repumping laser is attenuated by nearly 50% during the CMOT stage. This has the effect of decreasing the scattering rate of the cooling beam further. The detuning and repump power are linearly ramped from the MOT configuration to the CMOT configuration over the course of 30 ms. We found that ramping the quadrupole field strength off from the MOT level during this step improved the temperature after the molasses stage.

We performed the same fluorescence imaging as with the normal MOT to estimate that we have about  $10^9$  atoms at approximately  $50 \mu\text{K}$  at the end of the CMOT stage. Additionally, we obtain a size estimate of the cloud from the fluorescence images.

### 2.2.3 Optical Molasses

Following the compressed-MOT stage, a brief pulse of optical molasses light is applied to the atoms lasting about 5 ms. This has the effect of further reducing the temperature of the atoms. To perform this step, the magnetic field used in the MOT stage is turned off and the

the laser beams remain on. This creates standing waves along the three MOT beam pairs and they exert a velocity dependent force on the atoms via the spontaneous force. One would expect that the cooled atom temperature would be limited by the quantum heating due to the random spontaneous emission. When this heating balances the Doppler cooling provided by the beams, the resulting temperature is called the Doppler limit. In the optical molasses this is no longer the limit. The beams constituting the molasses are circularly polarized and a spatial dependence to the polarization arises from this. A full discussion of  $\sigma_+ \perp \sigma_-$  polarization gradient cooling is beyond the scope of this dissertation; however, details can be found in the work by Dalibard et al. [35]. The result is a damping effect on the atomic motion due to a radiation pressure imbalance.

Our molasses does not reach the recoil limit likely due to the optical depth of our atomic cloud. The benefit to applying this extra molasses light is that the atoms can be cooled to near the recoil limit; however, our molasses does not appear to work nearly this well. Stray field gradients have a large impact on the effectiveness of the molasses so we attempt to nullify these using a permanent magnet. Unfortunately, this gradient tends to drift over time. Additionally, the molasses provides slowing after the atoms are dropped from the magnetic trap before the pumping stage. The atoms must be released from the trap so that we can apply a bias field so that the pumping will be effective.

#### 2.2.4 Optical Pumping

After the molasses stage, the atoms are in many different Zeeman sub-states of the  $5^2S_{1/2}$ ,  $F=2$  ground state. These atoms can be loaded directly to the magnetic trap at the cost of losing the atoms which are in untrappable states. To collect all of the atoms in the magnetic trap they must therefore be prepared in a magnetically trappable state. Since we wish to create a condensate with these atoms, we would also like the atoms to remain in the ground state after this preparation.

In the ground state there are only three possible magnetically trappable sub-states:

$|F = 1, m = -1\rangle$ ,  $|F = 2, m = 1\rangle$ , and  $|F = 2, m = 2\rangle$ . This is because the atoms must be in a weak field seeking state, or a state in which the atoms seek a minimum in the magnetic field because it has been shown that it is not possible to create a local field maximum in a volume absent of currents and charges [36]. Therefore, the trapping field must create a local minimum. This will be addressed in the next section.

To prepare the atoms in the magnetically trappable state a bias magnetic field is applied and circularly polarized light of the proper polarization is allowed to impart angular momentum to the atoms. We elected to prepare the atoms in the  $|F = 2, m = 2\rangle$  because it results in tighter confinement while in the subsequent magnetic traps (both DC and AC traps). By applying laser light which is circularly polarized such that the angular momentum of the photons is parallel with the bias magnetic field, i.e.  $\sigma_+$  at the wavelength between the  $5^2S_{1/2}$ ,  $F=2$  ground state and the  $5^2P_{3/2}$   $F=2$  excited state, the atoms will be pumped to the  $|F = 2, m = 2\rangle$  ground state sub-level. This is easily understood through the selection rules since the pumping light must cause a change in the electronic m-level of  $+1$ . The atoms are then able to spontaneously emit a photon from the excited state causing a change in m-level by  $\pm 1$  or  $0$ . Therefore after several absorption emission cycles, nearly all of the atoms be pumped into the  $|F = 2, m = 2\rangle$  level of the ground state, which is dark to the pumping light. Therefore, once the atoms are in this state, they will remain there.

To implement the optical pumping stage, the cooling light is switched off with an AOM and mechanical shutter. The spherical quadrupole coils have already been switched off prior to the previous optical molasses stage. A bias coil is then switched on and the pump beam is sent along the axis of symmetry of this coil. The pump beam is circularly polarized in the  $\sigma_+$  handedness. This is shown schematically in figure 2.6.

### 2.2.5 Magnetic Trap

After pumping the atoms into the magnetically trappable state, they are then loaded into a DC magnetic trap. This trap works via the Zeeman shift in the energy levels of the atoms,

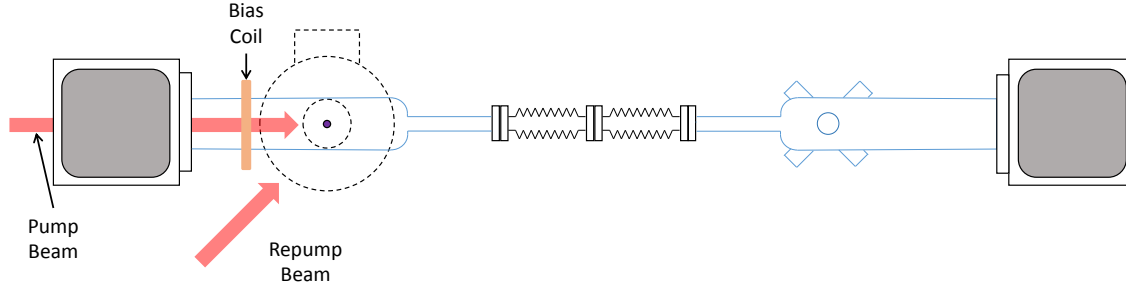


**Figure 2.6: Optical Pumping Setup Schematic.** A bias field is produced by the bias coil along the length of the chamber. The pump beam comes down the axis of symmetry of the coil.

i.e.  $U = -\boldsymbol{\mu} \cdot \mathbf{B}$ . Here  $\boldsymbol{\mu}$  is the magnetic moment of the atom and  $\mathbf{B}$  is the applied magnetic field. Since the atoms are loaded into a DC trap, the spins will align with the field at a given point and so the energy shift will only depend on the strength of the magnetic field  $U = g_F \mu_B m_F |\mathbf{B}|$ , where  $g_F$  is the Landé g-factor for the given state.

The atoms are in a state which is attracted to a field minimum. Therefore, a field needs to be produced which creates a minimum inside the vacuum chamber. This can be achieved by using the MOT coils to produce a spherical quadrupole field. This field has the spatial dependence shown in equation 2.2:

$$\mathbf{B} = B' \left[ \frac{1}{2} (x\hat{x} + y\hat{y}) - z\hat{z} \right] \quad (2.2)$$

This results in the spatially dependent potential in equation 2.3.

$$|\mathbf{B}| = \frac{B'}{2} \sqrt{x^2 + y^2 + 4z^2} \quad (2.3)$$

We switch the magnetic trap on immediately after the atoms finish the optical pumping stage and the field takes a few milliseconds to turn on. The optimum strength of the trap

was found empirically to produce the coldest trapped atoms. This resulted in a current of about 113 A and a corresponding quadrupole strength of just around 58 Gauss/cm.

### 2.2.6 Transfer to Science Cell

In order to make a condensate, we need to reduce the temperature of our atomic ensemble. To do this we use RF evaporation techniques, which will be discussed in more detail momentarily (see section 2.2.7), which requires a long trap lifetime in order to create runaway evaporation. In the MOT cell, the lifetime of the ground state is limited by collisions with the background gas to only a few seconds. This means that we must move our atoms to the lower pressure region in our vacuum chamber to reduce the losses. As discussed in the section on the vacuum system, the science cell has a pressure nearly 1000 times lower than the MOT cell. As a result, the lifetime is greatly increased to well over 60 s when the atoms are present in this section of the vacuum chamber.

Once the atoms have been successfully loaded into the magnetic trap, the trap strength is increased over the course of 200 ms to its maximum value. The maximum current we can supply to our quadrupole coils is about 750 A which corresponds to a gradient along the z-direction of about 388 Gauss/cm. This causes the atoms to be very tightly confined, but also causes the temperature to increase from the compression to around 1 mK. The electromagnet coils used to create the spherical quadrupole trap are mounted to a Parker Automation translation stage. This stage allows us to physically move the electromagnets, which in turn transports the atoms from the MOT cell to the science cell. The setup is shown schematically in figure 2.7.

As discussed previously, these two cells are separated by a long, thin tube, to allow for a differential pressure to develop between the two regions of the chamber. While loaded into the maximum strength magnetic trap the atomic cloud has a diameter of approximately 2.2 mm. This is important because the atomic cloud has to traverse this tube separating the two pressure regions of the vacuum system. The inner diameter of the tube is approximately

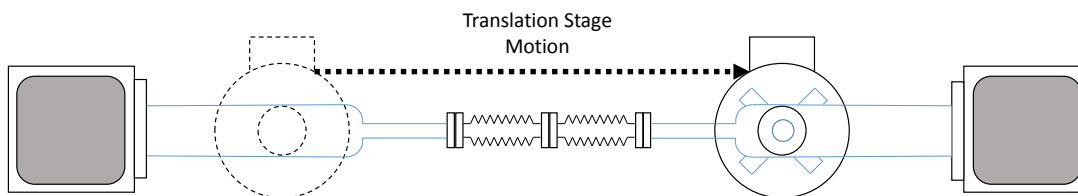


**Figure 2.7: Transfer Setup Schematic.** The electromagnets are mounted to a translation stage which runs parallel to the chamber. After loading the atoms into the magnetic trap, the coils are physically moved.

8 mm. To optimize the number of atoms transferred between the two regions of the vacuum system we physically move the translation stage to which the electromagnets are attached as well as the vertical position of the two coils to center the trap with the tube. To measure the efficiency of the transfer, we loaded the atoms into the magnetic trap and then released them, applied a pulse of the cooling laser and then measured the total fluorescence using a photodiode. This gave us our starting number. We then run the experiment a second time. This time the magnetic trap is loaded and the the electromagnets are moved from the MOT cell to the science cell and then returned to the MOT cell and the number of atoms is measured again. The alignment process can also be performed at intermediate travel distances if the track and tube were far from aligned. In fact, by doing just this after aligning the track we determined that nearly all of our losses during the transfer occur when the cloud first enters the small tube. We suspect that this is because some of the atoms collide with the opening of the tube.

We achieve an optimum transfer efficiency of approximately 40%. This results in a the transfer of approximately  $10^9$  atoms at a temperature of roughly 1 mK to the science cell.

### 2.2.7 RF Evaporation

With the sample of  $10^9$  atoms at around 1 mK, the phase space density is only about  $10^{-7}$ , which is far too low to produce a condensate. As such, we must increase the phase space density significantly. We do this by cooling the sample of atoms down through the use of RF evaporation. The basic principle of operation is to remove the hottest and therefore highest energy atoms from the trap. When the atomic sample is allowed to equilibrate via elastic collisions, the resultant temperature will be lower than that of the initial ensemble. Fortunately, removing a small fraction of the most energetic atoms reduces the temperature of the ensemble significantly and therefore the phase space density will increase. This is the exact same mechanism that cools a steaming cup of coffee. The hottest molecules in the coffee boil off thereby reducing the temperature of the coffee remaining in the cup. This process is known as evaporative cooling [37].

To implement this cooling, we utilize an RF transition between the internal Zeeman levels of the atoms. The potential energy for the different Zeeman states in the  $5^2S_{1/2}, F = 2$  state are shown versus position with the effects of gravity included in figure 2.8.

At temperatures much higher than the critical temperature, the atoms will obey Maxwell-Boltzmann statistics. The energy distribution is well known and characteristically has an exponential tail. By removing even a small number of very high energy atoms and allowing the ensemble to re-equilibrate, the total energy (temperature) can be reduced significantly without losing too many atoms. Clearly the atoms with the most energy will move furthest from the trap center based on the potential energy of the magnetic trap. They will also therefore have the largest splitting in energy between the Zeeman sub-levels. Therefore to reduce the temperature of the atoms, an antenna was placed inside the vacuum chamber. This antenna is discussed in more detail in section 3.2. By turning the RF radiation on with a relatively high frequency of about 90 MHz and ramping the frequency down slowly (to allow for the atoms to re-thermalize), the temperature can be reduced significantly.

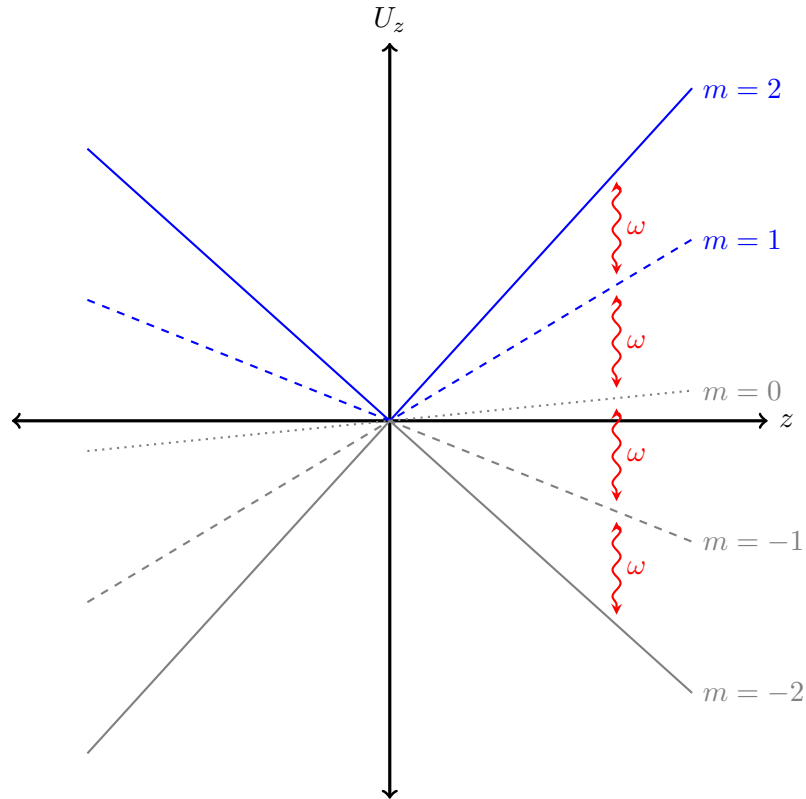


**Figure 2.8: Energy Level Diagram for Evaporative Cooling in DC trap.** The effects of gravity are included in the potential to emphasize that only the  $m=1$  and  $m=2$  states are trappable. To get an idea of scaling, the energy splitting between the  $m$ -levels is 0.7 MHz/Gauss.

### 2.2.8 Time-Orbiting Potential Trap

While the atoms can be cooled by evaporative cooling there is unfortunately a limit while the atoms are in the quadrupole magnetic trap. As the atoms cool down to lower and lower temperatures, they will have lower kinetic energy and therefore will spend more time near the center of the trap. If the atoms pass through the center of the trap, then the magnetic field is momentarily zero. During this time, it is possible for the atoms to lose their spin orientation and their spins can become reoriented when they move out of the center of the trap. This can result in them being in an anti-trapped state and being lost from the

ensemble. These non-adiabatic spin flips are referred to as Majorana losses [38].

There are several means to combat this problem. The trap could be made such that the minimum is a local minimum and non-zero [39, 40], the center of the trap can be plugged by a blue-detuned laser [27] or the field zero can be moved through space around faster than the atoms can respond but slower than the Larmor precession frequency [41]. This last solution is often referred to as a Time-Orbiting Potential trap, or TOP trap, and is the basis for the trap we have elected to use in our experiment.

To implement the TOP trap, we apply a rotating bias field and the same DC spherical quadrupole field which was used to transfer the atoms from the MOT cell to the science cell. In a traditional TOP trap, the bias field rotates around in a plane; however, we use a more complicated bias that rotates around on a sphere due to the simplification it provides to the electronics we need for our entire experiment. This is the same bias used for the trap in which interferometry experiments are performed (described in Chapter 3). The fields are described mathematically in equations 2.4 and 2.5

$$\mathbf{B}_{bias} = B_0 \begin{pmatrix} \sin(\Omega_1 t) \cos(\Omega_2 t) \\ \sin(\Omega_1 t) \sin(\Omega_2 t) \\ \cos(\Omega_1 t) \end{pmatrix} \quad (2.4)$$

$$\mathbf{B}_{quad} = B'_{DC} \begin{pmatrix} x/2 \\ y/2 \\ -z \end{pmatrix} \quad (2.5)$$

Here  $z$  is the direction opposing gravity and  $x$  and  $y$  are in the plane of the optics table. This is the same convention used for the waveguide in Chapter 3.

Just as with the DC spherical quadrupole magnetic trap, we expect that the potential energy of the atoms will be given by the Zeeman effect, i.e.  $U = -\boldsymbol{\mu} \cdot \mathbf{B}$ . Although since the field is rotating faster than the atoms can respond, while still slow enough that the spin of the atoms can follow the bias, the resulting potential will be the time averaged potential. In other words, since the spin is able to stay aligned with the bias, the potential that the

atoms will experience is given by equation 2.6.

$$U = g_F m_F \mu_B \langle |\mathbf{B}| \rangle \quad (2.6)$$

Note that the brackets indicate the time-average. This can be calculated just as for the waveguide potential from section 3.1 and I will therefore skip the details and simply state the result. The total potential energy felt by the atoms in the TOP trap is given by equation 2.7.

$$U_{tot} = \mu_B B_0 + mgz + \frac{1}{2} m \omega_x^2 x^2 + \frac{1}{2} m \omega_y^2 y^2 + \frac{1}{2} m \omega_z^2 z^2 \quad (2.7)$$

where the trap frequencies in the  $x$ ,  $y$ , and  $z$  directions are given in equation 2.8.

$$\begin{aligned} \omega_x = \omega_y &= \left[ \frac{2\mu_B}{m} \left( \frac{3}{32} \frac{B_{DC}^2}{B_0} \right) \right]^{1/2} \\ \omega_z &= \left[ \frac{2\mu_B}{m} \left( \frac{1}{4} \frac{B_{DC}^2}{B_0} \right) \right]^{1/2} \end{aligned} \quad (2.8)$$

The TOP trap offers one major advantage to the other trap types. The TOP trap provides reduced sensitivity to extraneous magnetic fields. This comes from the fact that the spins of the atoms remain aligned with the rotating bias field so long as the rotation of the bias is well below the Larmor frequency. Therefore, magnetic fields far from the trap driving frequency will not contribute to an energy shift in the atoms since half of the time the spins will be aligned and the other half they will be anti-aligned to those fields. Half of the time the resulting energy shift will be positive and the other half it will be negative and will therefore cancel. This can be quite important for an interferometer where the energy of the atoms becomes a phase difference and can become a source of noise.

After the first stage of evaporative cooling, we transfer the atoms from the DC magnetic trap to the TOP trap. To do this, the atoms are evaporatively cooled until they reach around  $100 \mu\text{K}$  (just below this temperature Majorana losses start become an issue). The rotating bias field is then switched on at full strength (23 Gauss). As mentioned before, atoms

which pass through the field zero can be kicked from the trap and we can use this to our advantage. The field zero is moving around the atoms on the surface of an ellipsoid and this ellipsoid defines the maximum size of the atomic cloud. By reducing the strength of the bias field, the ellipsoid shrinks, thereby acting as another way to expel the most energetic atoms and evaporatively cooling the cloud. We therefore ramp the bias field strength from its maximum of 23 Gauss down to around 7 Gauss and effectively reduce the bottom frequency of the trap as well as evaporatively cool the atoms.

### 2.2.9 Imaging

To evaluate the various stages in producing a condensate, we chose to use absorption imaging. The basic principle of absorption imaging is to shine light on the cloud of atoms and to observe the shadow created due to absorption on a CCD. This is represented schematically in figure 2.9.

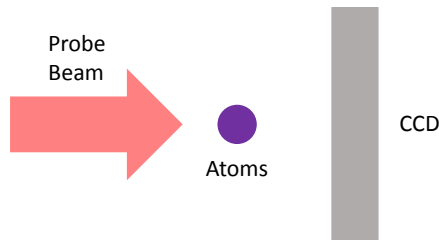


**Figure 2.9: Absorption Imaging Schematic.** A near-resonant laser beam is used to cast a shadow of the atoms onto a CCD.

To implement the absorption imaging for our experiment, we use a probe laser beam operating very close to resonance on the  $5^2S_{1/2}, F = 2$  to  $5^2P_{3/2}, F = 3$  transition. The laser passes through the atoms and into an imaging system. This imaging system comprises two sections. The first is a simple 1:1 telescope to move the imaging plane outside of the vacuum cell which is composed of two 75 mm lenses separated by 150 mm. The second is

used to image the atoms onto the CCD. An imaging setup for both the vertical (along  $z$  direction by convention used) and horizontal (along  $y$  direction) directions was used. For diagnosing the BEC production stages, only the horizontal imaging was used. A schematic representation of the horizontal imaging setup is shown in figure 2.10. The reason for this being that the atomic cloud is released from the trap prior to imaging to obtain temperature information via ballistic expansion. Therefore, the atoms remain in focus for the horizontal imaging setup, while the focus would need to be adjusted for the vertical.

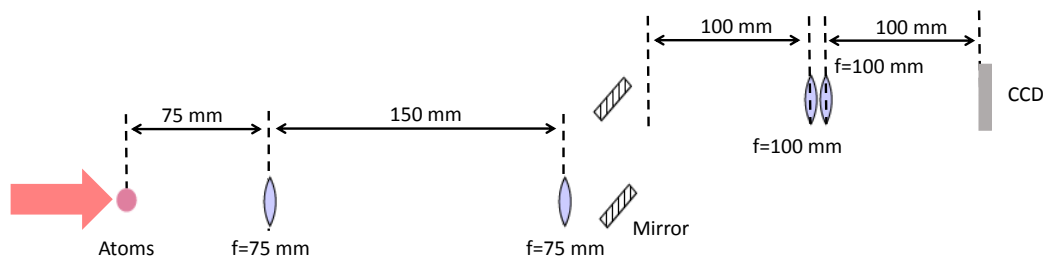


**Figure 2.10: Horizontal Imaging Schematic.** The mirrors allow for easy alignment of the probe beam onto the CCD.

### 2.2.10 Condensate

After the atoms are loaded into the TOP trap the phase-space density is still too low to produce a condensate ( $\rho \approx 10^{-2}$ ). We therefore apply a second stage of RF evaporation to further increase the phase-space density. This stage of evaporation was empirically optimized to produce the most atoms with the highest phase-space density. To determine that we do indeed have a condensate, we drop the sample of atoms for 20 ms and image the atoms with our side absorption imaging setup. At the transition to a condensate, a clear peak occurs in the cloud of thermal (400 nK) atoms. As more atoms are evaporated from the sample, the thermal cloud slowly vanishes while the condensate peak increases. The

first images of a BEC in our apparatus are shown in figure 2.11.

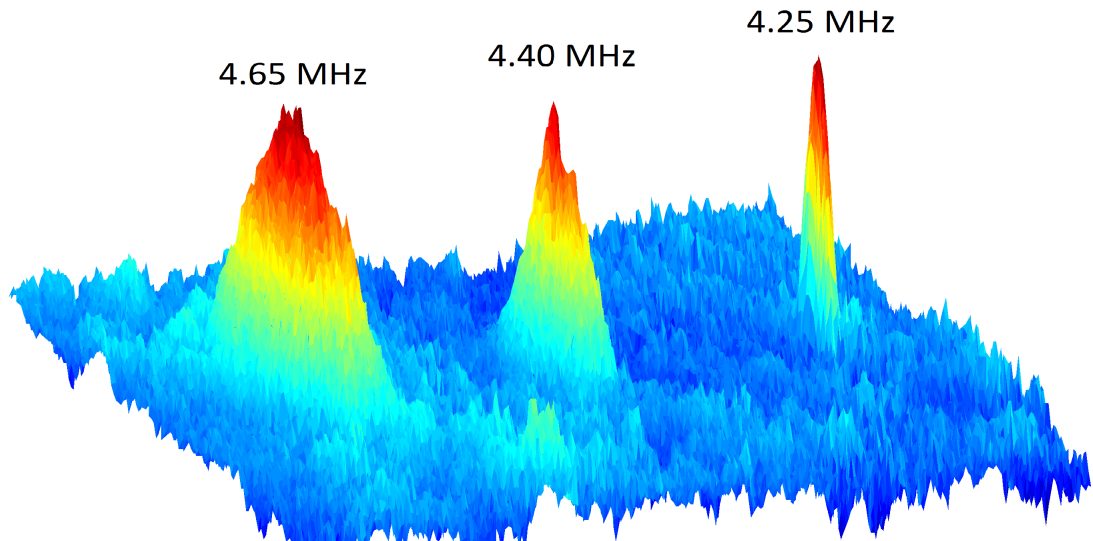


**Figure 2.11: Condensate Formation.** This shows a composite image of the atoms after expansion at various bottom frequencies of the trap. A clear peak begins to appear around 4.40 MHz and we have a high purity condensate at 4.25 MHz.

We achieve a condensate of approximately  $10^4$   $^{87}\text{Rb}$  atoms.



# 3 | MAGNETIC TRAP

To conduct an atom interferometry experiment with any sort of precision, one of the most important factors is to have a long interaction time for the interferometer. One way to do this is to perform the interference experiments on the atoms while they undergo free-fall. While at first glance, this seems straight-forward enough, it does have limitations. Namely, for interaction times even on the order of a second a rather tall tower structure is required of around a meter tall. This can effect can be reduced to some degree by using a fountain configuration where the atoms are kicked upwards as the interferometer experiment begins. Another approach to increasing the interaction time is to confine the atoms in some coherence maintaining trapping potential. Atom interferometers have been implemented in magnetic traps of varying configurations. They have been implemented in linear guides where one trap direction is considerably weaker than the other two [42, 18]. They have also been implemented in ring configurations [43]. Interferometers have also been implemented in traps that are a cross between the two like a stadium [44]. For our experiments we consider a variant to the trap used by Reeves et al. [18], which uses a Time-Orbiting Potential. However, we desire to have a cylindrically symmetric trapping potential so that it is optimized for rotation sensing. This will allow the interferometer to enclose a circular area, thereby maximizing the area enclosed and thus the sensitivity to rotations for a given interferometer time.

### 3.1 Design

To make an interferometer in a small enclosed volume with long interaction times ( $\approx 1$  s), we need to supply support against gravity. We have elected to use a magnetic trap utilizing a Time-Orbiting Potential also known colloquially as a TOP trap [41]. The basic premise of such a trap is to move the field zero location around the atoms more rapidly than the atoms can follow, yet keeping the rotation of the bias field below the Larmor precession frequency such that the spin state can be maintained. The resultant potential which the atoms will experience will be given by the time-average of the potential. From chapter 2, we know that the time-averaged potential energy shift that an atom undergoes in a magnetic field is given by:

$$U = \langle -\boldsymbol{\mu} \cdot \mathbf{B} \rangle = -\mu_z \langle |\mathbf{B}| \rangle = m_F g_F \mu_B \langle |\mathbf{B}| \rangle \quad (3.1)$$

where  $m_F$  is the quantum number for the component of the total electronic angular momentum along the field direction and  $g_F$  is the Landé g-factor. In our experiment, we optically pump all of the atoms into the  $|F = 2, m_F = 2\rangle$  state before loading them into the magnetic trap. Therefore,  $m_F g_F = 1$ . I will consider the potential for only this state from this point forward.

In previous work in this lab, a magnetic trap was developed under a similar configuration to provide a linear waveguide [18]. To obtain a cylindrical trapping potential, we have chosen a field configuration that includes an oscillating spherical quadrupole field along with a bias field which rotates in space at two frequencies. The bias field rotates in a vertical plane with a frequency  $\Omega_1$  and that plane rotates about the vertical  $z$ -axis with frequency  $\Omega_2$ . The resulting bias field vector traces out a path on the surface of a sphere as shown in figure 3.1. The bias and AC quadrupole fields are expressed mathematically in equations 3.2 and 3.3 respectively.

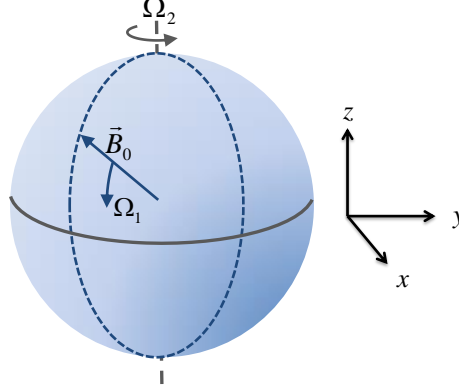


**Figure 3.1: AC Bias Field.** The bias field rotates in a vertical plane at angular frequency  $\Omega_1$ , and that vertical plane rotates about the  $z$ -axis at angular frequency  $\Omega_2$ .

$$\mathbf{B}_{bias} = B_0 \begin{pmatrix} \sin(\Omega_1 t) \cos(\Omega_2 t) \\ \sin(\Omega_1 t) \sin(\Omega_2 t) \\ \cos(\Omega_1 t) \end{pmatrix} \quad (3.2)$$

$$\mathbf{B}_{quad} = B'_1 \cos(\Omega_1 t) \begin{pmatrix} x/2 \\ y/2 \\ -z \end{pmatrix} \quad (3.3)$$

Here the same coordinate system is used as with the TOP trap in chapter 2. The  $z$ -direction opposes gravity and the  $x$  and  $y$  directions are in the plane of the table. To be precise,  $x$  points along the long direction of the vacuum chamber from the science cell to toward the MOT cell. The  $y$  is chosen by the right-hand rule. In the expressions above for the fields,  $B_0$  is the strength of the bias field and  $B'_1$  is the strength of the quadrupole field gradient along the  $z$  direction.

To determine the trapping potential, the magnitude of the field needs to be calculated.

$$\begin{aligned}
|\mathbf{B}| = |\mathbf{B}_{bias} + \mathbf{B}_{quad}| = & \left[ \left( B_0 \sin(\Omega_1 t) \cos(\Omega_2 t) + \frac{B'_1 x}{2} \cos(\Omega_1 t) \right)^2 \right. \\
& + \left( B_0 \sin(\Omega_1 t) \sin(\Omega_2 t) + \frac{B'_1 y}{2} \cos(\Omega_1 t) \right)^2 \\
& \left. + (B_0 \cos(\Omega_1 t) - B'_1 z \cos(\Omega_1 t))^2 \right]^{1/2}
\end{aligned} \tag{3.4}$$

After some minor simplification, this becomes

$$\begin{aligned}
|\mathbf{B}| = B_0 & \left[ 1 + \frac{B'_1}{B_0} \sin(\Omega_1 t) \cos(\Omega_1 t) (x \cos(\Omega_2 t) + y \sin(\Omega_2 t)) \right. \\
& \left. - 2 \frac{B'_1}{B_0} z \cos(\Omega_1 t) + \frac{B_1'^2}{B_0^2} \cos^2(\Omega_1 t) \left( \frac{x^2 + y^2}{4} + z^2 \right) \right]^{1/2}
\end{aligned} \tag{3.5}$$

Since the field oscillates much faster than the atoms can follow, we define the time average as the long time average

$$\langle f \rangle = \lim_{T \rightarrow \infty} \frac{1}{T} \int_0^T f(t) dt \tag{3.6}$$

To evaluate this integral, a Taylor expansion of the integrand can be made to approximate the result and simplify the calculation. In this case, the series expansion around the origin is given by

$$\sqrt{1 + \varepsilon} \approx 1 + \frac{1}{2}\varepsilon - \frac{1}{8}\varepsilon^2 + \dots \tag{3.7}$$

and requires that  $\varepsilon \ll 1$ . This results in the following time-averaged magnetic field (keeping only terms in  $x$ ,  $y$ , and  $z$  to second order).

$$\begin{aligned}
\langle |\mathbf{B}| \rangle \approx B_0 & \left[ 1 + \frac{B'_1}{2B_0} x \langle \sin(\Omega_1 t) \cos(\Omega_1 t) \cos(\Omega_2 t) \rangle \right. \\
& + \frac{B'_1}{2B_0} y \langle \sin(\Omega_1 t) \cos(\Omega_1 t) \sin(\Omega_2 t) \rangle \\
& - \frac{B'_1}{B_0} z \langle \cos^2(\Omega_1 t) \rangle \\
& + \frac{B_1'^2}{2B_0^2} \left( \frac{x^2 + y^2}{4} + z^2 \right) \langle \cos^2(\Omega_1 t) \rangle \\
& - \frac{B_1'^2}{8B_0^2} x^2 \langle \sin^2(\Omega_1 t) \cos^2(\Omega_1 t) \cos^2(\Omega_2 t) \rangle \\
& - \frac{B_1'^2}{8B_0^2} y^2 \langle \sin^2(\Omega_1 t) \cos^2(\Omega_1 t) \sin^2(\Omega_2 t) \rangle \\
& - \frac{B_1'^2}{2B_0^2} z^2 \langle \cos^4(\Omega_1 t) \rangle \\
& - \frac{B_1'^2}{4B_0^2} xy \langle \sin^2(\Omega_1 t) \cos^2(\Omega_1 t) \sin(\Omega_2 t) \cos(\Omega_2 t) \rangle \\
& - \frac{B_1'^2}{2B_0^2} xz \langle \sin(\Omega_1 t) \cos^2(\Omega_1 t) \cos(\Omega_2 t) \rangle \\
& \left. - \frac{B_1'^2}{2B_0^2} yz \langle \sin(\Omega_1 t) \cos^2(\Omega_1 t) \sin(\Omega_2 t) \rangle \right] \tag{3.8}
\end{aligned}$$

By imposing the restriction that  $\Omega_1$  and  $\Omega_2$  are incommensurate the relevant time-averaged functions can be evaluated.

$$\begin{aligned}
\langle \sin(\Omega_1 t) \cos(\Omega_1 t) \cos(\Omega_2 t) \rangle &= 0 \\
\langle \sin(\Omega_1 t) \cos(\Omega_1 t) \sin(\Omega_2 t) \rangle &= 0 \\
\langle \cos^2(\Omega_1 t) \rangle &= 1/2 \\
\langle \sin^2(\Omega_1 t) \cos^2(\Omega_1 t) \cos^2(\Omega_2 t) \rangle &= 1/16 \\
\langle \sin^2(\Omega_1 t) \cos^2(\Omega_1 t) \sin^2(\Omega_2 t) \rangle &= 1/16 \\
\langle \cos^4(\Omega_1 t) \rangle &= 3/8 \\
\langle \sin^2(\Omega_1 t) \cos^2(\Omega_1 t) \sin(\Omega_2 t) \cos(\Omega_2 t) \rangle &= 0 \\
\langle \sin(\Omega_1 t) \cos^2(\Omega_1 t) \cos(\Omega_2 t) \rangle &= 0 \\
\langle \sin(\Omega_1 t) \cos^2(\Omega_1 t) \sin(\Omega_2 t) \rangle &= 0
\end{aligned} \tag{3.9}$$

After plugging these time averages back into equation (3.8), the final form of the potential,

including the gravitational potential, is as follows

$$U_{tot} = \mu_B B_0 + mgz - \frac{1}{2}\mu_B B_1' z + \frac{1}{2}m\omega_x^2 x^2 + \frac{1}{2}m\omega_y^2 y^2 + \frac{1}{2}m\omega_z^2 z^2 \quad (3.10)$$

where the angular frequencies of the trap are

$$\begin{aligned} \omega_x = \omega_y &= \left[ \frac{2\mu_B}{m} \left( \frac{7}{128} \frac{B_1'^2}{B_0} \right) \right]^{1/2} \\ \omega_z &= \left[ \frac{2\mu_B}{m} \left( \frac{1}{16} \frac{B_1'^2}{B_0} \right) \right]^{1/2} \end{aligned} \quad (3.11)$$

It's clear that this relatively straightforward field configuration can provide the desired result. The trap is cylindrically symmetric in the horizontal plane, i.e.  $\omega_x = \omega_y$ , and by careful choice of the quadrupole strength ( $B_1' = 2mg/\mu_B$ ), the atoms will be supported against gravity.

The way we create the fields in equations (3.2) and (3.3) is by using six independent coils with a pair of coils along each axis, ( $\hat{x}$ ,  $\hat{y}$ , and  $\hat{z}$ ). This configuration is shown schematically in figure 3.2. We define a positive current as one that produces a field along the positive direction of the axis of symmetry for a given coil. Therefore, the following currents will produce the desired fields.

$$\begin{aligned} I_x &= I_0 \sin(\Omega_1 t) \cos(\Omega_2 t) \\ I_y &= I_0 \sin(\Omega_1 t) \sin(\Omega_2 t) \\ I_{z+} &= (I_0 - I_1) \cos(\Omega_1 t) \\ I_{z-} &= (I_0 + I_1) \cos(\Omega_1 t) \end{aligned} \quad (3.12)$$

Here  $I_0$  is responsible for creating the bias field, while  $I_1$  creates the quadrupole field. Note that the subscripts indicate the symmetry axis of the the coils. Both coils along a given direction are aligned such that a positive current produces a field in the positive direction along the axis of symmetry. Additionally, the plus and minus subscript given for the z direction indicates the direction along z that the given coil is displaced. The coils along the x and y directions have the same current supplied in each of the coils in that pair.

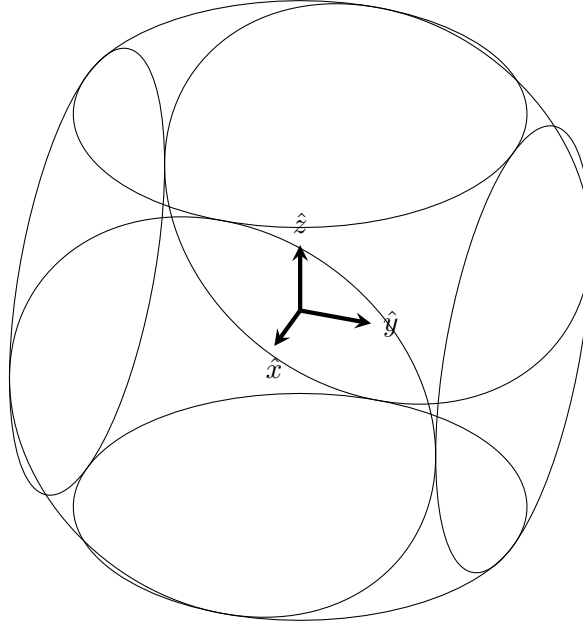


**Figure 3.2: Coil Geometry.** The fields can be implemented by using a pair of coils separated along each direction:  $x$ ,  $y$ , and  $z$ .

As a next step the design of the coils was considered. To cancel gravity it has already been mentioned that the quadrupole strength needs to be set to a certain value for a given atomic state. In the case of our atoms, the necessary quadrupole strength is  $B'_1 = 2mg/\mu_z = 30.7$  Gauss/cm. The field from a current loop with radius,  $R$ , at a position  $z$  along the coils symmetry axis is given by

$$B_z(z) = \frac{\mu_0 I}{2R} \frac{1}{(1 + z^2/R^2)^{3/2}} \quad (3.13)$$

Using this expression, the field at the position between a pair of coils with radius  $R$  and separation  $d$  along their symmetry axis, and with the same currents such that the field produced by the two coils are aligned along  $\hat{z}$

$$B_z = \frac{\mu_0 I}{R} \frac{1}{(1 + d^2/(4R^2))^{3/2}} \quad (3.14)$$

Additionally, for the same configuration, but with the current in the positively displaced

coil such that the fields produced by the two coils are opposed, the derivative at the center is given by

$$\frac{dB_z}{dz} = \frac{3\mu_0 Id}{2R^3} \frac{1}{(1 + d^2/(4R^2))^{5/2}} \quad (3.15)$$

There are several physical constraints for our system as well. There is very little clearance outside of the vacuum chamber due to the translating coils which are required to make a condensate. Additionally, the vacuum chamber prevents external coils from being very close together. To minimize the effect of the separation, a larger radius coil would need to be used. It is also clear from equations (3.14) and (3.15) that the further separated and the larger the coil radius the more current is needed to produce the same field strength. Furthermore, more current and larger coils will lead to higher heat being produced by the coils during operation. For these reasons, it was determined that the best course of action was to design the coils to be inside the vacuum chamber.

The final configuration for this design was to use six independent coils inside the vacuum chamber. This will be discussed in more depth in the next section (3.2).

While this result shows that the configuration of fields described in equations (3.2) and (3.3) will yield the desired cylindrically symmetric, trapping potential, it neglects a very important term. For a real set of coils, there could also be a curvature to the field such that it varies quadratically from the center along the axis of the coil pairs. One possible way to avoid this consequence is to use a coil pair in the Helmholtz configuration. In this fashion the curvature is zero and the additional term will be negligible. However, due to the constraints of the design this was not possible. If this curvature is included in the field calculation, then the bias produced by a pair of coils with symmetry axis along the z-direction can be written as in (3.16), where  $\gamma$  is the curvature of the field along the z-direction.

$$\mathbf{B}_{bias} = B_0 \begin{pmatrix} -\gamma zx/2 \\ -\gamma zy/2 \\ 1 + \gamma z^2/2 - \gamma(x^2 + y^2)/4 \end{pmatrix} \quad (3.16)$$

We can therefore obtain a more accurate model of the potential by including the effects of the curvature in the total bias field produced from three identical pairs of coils with their axes of symmetry aligned along x, y, and z and using the same time dependence as in equation 3.2. Since we are only interested in keeping terms to second order, the curvature in the spherical quadrupole field can be neglected as it enters into the potential as a third-order term. The same type of procedure which was used before can be used to determine the resulting time-averaged potential; however, the math is quite laborious in this case. As such, I will spare the unpleasant details and simply state the resulting potential in equation (3.17).

$$U_{tot} = \mu_z B_0 + mgz - \frac{1}{2}\mu_z B_1' z + \frac{1}{2}m\omega_x^2 x^2 + \frac{1}{2}m\omega_y^2 y^2 + \frac{1}{2}m\omega_z^2 z^2 \quad (3.17)$$

where the angular frequencies of the trap now include a correction from the curvature of the fields.

$$\begin{aligned} \omega_x = \omega_y &= \left[ \frac{2\mu_z}{m} \left( \frac{7}{128} \frac{B_1'^2}{B_0} - \frac{\gamma}{16} B_0 \right) \right]^{1/2} \\ \omega_z &= \left[ \frac{2\mu_z}{m} \left( \frac{1}{16} \frac{B_1'^2}{B_0} + \frac{\gamma}{8} B_0 \right) \right]^{1/2} \end{aligned} \quad (3.18)$$

One interesting result from this calculation is that the x and y frequencies go to zero, while the z frequency remains relatively strong. The curvature of the coils along each direction can be estimated from the simple model 3.14 for a pair of coils. Given the constraints of placing the coils inside the vacuum chamber, we are limited to a separation of  $d = 2.14$  cm and an average coil radius of  $R = 0.76$  cm. Using the model of coils made of infinitesimally small wires with these parameters gives an approximation of the bias field strength of  $B_0/I_0 = 4.48$  Gauss/A and the curvature of the bias field is given by  $\gamma = 4.0$  cm<sup>-2</sup>. Additionally, the quadrupole strength is  $B_1/I_1 = 8.3$  Gauss/cm/A. With these parameters, the x and y frequencies go to zero at a bias strength of  $B_0 = 14.3$  Gauss.

For an improved estimate, the field and resulting potential was calculated numerically taking the geometry of the coils into account. The coil geometry is discussed in detail in section 3.2. The field was calculated using the Biot-Savart Law for small wire segments. The coils were modeled as spirals with a small segment of wire connecting them at the center just as the actual coils were made. The currents used in the field calculation contained the same time dependence as in equation (3.2). The potential was then time averaged by setting the two frequencies to a ratio of 1:2 and integrating over one period of the more slowly oscillating frequency. In addition to the potential from the magnetic field gravity was also included.

The gradient of the potential was calculated and the quadrupole current was adjusted to balance gravity. Upon doing this, the potential was recalculated and the curvature was computed along all directions, yielding the Hessian matrix. The matrix was diagonalized and the remaining elements were the trap frequencies. It's worth noting that the off-diagonal terms were small and therefore, the principal axes of the trap are shifted only slightly from the coordinate axes. The results of the trapping frequencies versus bias field strength are plotted in figure 3.3.

From these fitting parameters the quadrupole strength and the curvature of the bias can be determined by comparing with the expected trap frequencies from equation (3.18). This yields the results  $B'_1 = 30.5 \pm 0.1$  Gauss/cm, which is close to the expected value needed to cancel gravity. The curvature coefficient for the bias field is  $\gamma = 3.96 \pm 0.02$  cm<sup>-2</sup>, which is quite close to the value obtained from the simple model using two coils.

## 3.2 Construction

To implement the fields discussed in section 3.1, six independent coils are used with a pair along each axis.

Since we're implementing the waveguide inside the vacuum chamber, we must choose

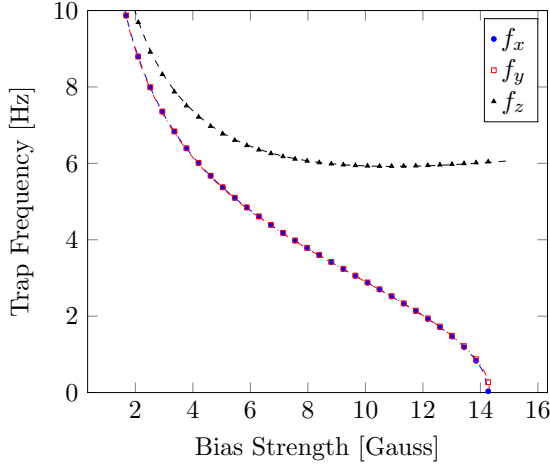


**Figure 3.3: Trap Frequencies versus Bias Field Strength.** The fitting function is used to compare with the analytic model. The quadrupole strength is set at  $B'_1 = 30.5$  Gauss which corresponds to a current of  $I_1 = 3.96$  A

Axis	$\alpha$ [Gauss $\cdot$ Hz <sup>2</sup> ]	$\beta$ [Hz <sup>2</sup> /Gauss]
X	$165.86 \pm 0.02$	$-0.814 \pm 7e - 5$
Y	$164.34 \pm 0.39$	$-0.801 \pm 0.002$
Z	$191.93 \pm 0.41$	$1.60 \pm 0.01$

**Table 3.1: Trap Frequency Fit Parameters for Numerical Calculation.** Fitting Function:

$$f(V_{bias}) = \sqrt{\frac{\alpha}{B_0} + \beta B_0}$$

materials which have low vapor pressures at room temperature in order to maintain the ultra-high vacuum necessary for BEC production. The materials must also effectively dissipate the heat produced by the coils during operation. Finally, the material must withstand the elevated temperatures of the vacuum system bake. Other groups have had success using copper clad Aluminum Nitride substrates, where the copper has been chemically bonded to the Aluminum Nitride substrate [45]. Aluminum Nitride is an attractive material because it offers a very low thermal expansion coefficient ( $\alpha_T = 6.09 \times 10^{-6} \text{ K}^{-1}$ ) and the thermal conductivity typical of a metal ( $\kappa_T = 30 \text{ W/m/K}$ ); however, it is an electrical insulator [46]. Curamik GMBH offers a product line of these substrates with varying copper thickness. We elected to use a 0.63 mm thick AlN substrate with a copper thickness of 0.125 mm bonded to each side.

### 3.2.1 Coil Chip Production

The coil patterns were produced by photolithography. Much effort was devoted into developing the coil production process to establish the specifications to which the coils could be manufactured as well as ensure that the chips were produced with sufficient quality. I will briefly outline the procedure here and defer to the more detailed description which can be found in Appendix [A](#).

The basic process for producing the coil chips was to first cut the card supplied by Curamik into chip sized pieces ( $\approx 1$  inch per side). Due to the hardness of AlN, abrasive machining was required. To slice the card into appropriately sized bits, a diamond saw was used. The coils were then cleaned of any contaminants and were prepared for the chemical etching process. The copper clad chips were then coated with a photo-resistive material (MG Chemicals Dry Film Negative Resist, #416DFR-5). A negative pattern of the coil was produced onto an opaque mask through which the photo-resist was then exposed to UV light. This was repeated on both sides of the chip with special caution used to ensure alignment of the patterns. The chips were then developed using a chemical solution (MG Chemicals Negative Resist Developer, #4170-500ML) to remove the unexposed portions of the photoresist. This left a coil pattern in the photo-resistive material. The coils were then etched in a solution of Muriatic acid (33% HCl) and Hydrogen Peroxide at a volume ratio of 1:1, thereby removing the unwanted copper. The thickness of the copper on these boards is thicker than standard printed circuit boards and produced difficulty in etching. To improve the etch quality, the acid solution was heated. This provided two benefits. First, the etching time was decreased, which reduced the chance of the mask eroding away from the substrate. Secondly, it decreased the amount of undercut on the coil traces.

It is worth noting that to develop the photo-mask which was used in the development process before etching a custom program was written to produce the coil pattern in the industrial standard RS-274X Gerber file format. The pattern needed to be at quite high

resolution because the photo-resistive material was capable of producing features of approximately 45 nm size. Initially, we attempted to print the mask on standard overhead transparencies; however, these proved to be of insufficient quality for our purposes. The UV lamp used to expose the photo-resist bled through these inexpensive masks and typically led to areas on the coil pattern that would not be etched properly. To rectify this problem, we sent our mask file to a circuit board fab house in order to create the mask on an acetate film. This led to much better results in the final etched coil pattern.

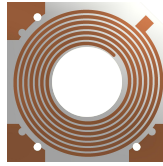


**Figure 3.4: CAD rendering of Coil Chip.** The spiral trace is the same on both sides. A more detailed drawing of the coil chip is available in Appendix B.

A CAD rendering of the coil patterns used for the magnetic trap is shown in Figure 3.4. The coils were double sided, with 7 turns on each side. The spiral pitch of the coil was 0.7 mm/turn and the copper traces were approximately .4 mm wide and 0.125 mm thick. To machine the holes into the coil, abrasive tooling was once again used. The central hole has a diameter of 1 cm, and the smaller mounting holes are made to allow clearance for a #00 threaded rod. To make the connection between the two sides of the board, it was necessary to solder a thin copper wire between the innermost point on the spiral on each side. Finally, to make electrical connections to the coil a small solder tab was placed on the notched corner. This was present on both sides of the chip.

Since the coils were going to be placed into the vacuum chamber, a solder compatible with the ultra-high vacuum was necessary. Additionally, it was required that the melting point be sufficiently high to allow us to bake our chamber to allow us the ability to reach these same pressures. An alloy of lead, tin, and silver was used (Multicore HMP 1.5%Ag,97.5%Pb,1%Sn) which has a solidus melting point of  $\approx 300^{\circ}\text{C}$  and a working tem-

perature of 255°C. Therefore, we were able to safely bake our vacuum chamber to 250°C. Additionally, the vapor pressure at room temperature for this alloy is below the working pressure for our vacuum chamber and as such out-gassing from the solder has not impacted the stability of the vacuum pressure.

To ensure the quality of the etching process several measurements were taken for the coils. The resistance and inductance of each coil was measured using an Agilent LCR meter. When a short was present between two loops on the spiral the inductance decreased measurably and was a good indication that the etch had not completely finished. Between these measurements and optical inspection, the coil production was made quite consistent. The resistance and inductance for each coil are shown in table 3.2.

Phase	$R$ [ $\Omega$ ]	$L$ [ $\mu\text{H}$ ]
$X_+$	0.285	3.34
$X_-$	0.228	3.33
$Y_+$	0.285	3.35
$Y_-$	0.268	3.33
$Z_+$	0.265	3.32
$Z_-$	0.223	3.33

**Table 3.2: Coil Chip Impedance Measurements** Measured impedance for each coil without any leads attached.

### 3.2.2 Waveguide Support Structure

To mount the waveguide inside the vacuum chamber it was necessary to design a mechanical structure to not only support the coils, but to also act as a heatsink to quickly remove the heat produced by the coils when running the trap. Additionally, it was necessary to select materials with low thermal expansion coefficients in order to reduce the effect of thermal expansion on the magnetic field strength. Finally, the material needed to be electrically insulating so that the coils would remain isolated from each other and also to prevent field distortion due to eddy currents. HBC grade hot-pressed Boron Nitride (BN) from Momentive was selected because it offers a very low thermal expansion coefficient, it acts as

an electrical insulator and it has quite good thermal conductivity for an insulator. Boron Nitride is anisotropic and Momentive specifies a range for the thermal expansion coefficient of  $\alpha_T = 0.4 - 0.8 \times 10^{-6} \text{ K}^{-1}$  and a range for the thermal conductivity of  $\kappa_T = 23 - 30 \text{ W/m/K}$  near room temperature. The properties of BN are in fact similar to those AlN, which makes it an outstanding candidate for the support structure. BN is also machinable with conventional tooling, albeit with difficulty due to its delicate nature.

The coils constituting the waveguide were mounted to a cube made of BN. The cube had a notch on two corners to allow the electrical connections to be made to the coils by wires. Additionally, the hole in one of the faces of the cube was made with a countersink, such that it could be held onto the support arm by a screw made out of Vespel (bulk Kapton), a plastic which provides very good electrical insulation and vacuum properties. A small, Kapton-coated wire (30 AWG) was wrapped around the body of this Vespel screw creating a single loop with a diameter of approximately 1 cm. This loop would act as the antenna for RF evaporative cooling as discussed in section 2.2.7. To allow the loose ends of the antenna wire to exit the cube, a slot was cut along the clearance hole for the Vespel screw body that the antenna was wrapped around and out to the nearest notched corner. A cutaway view of the trap support structure displaying the placement of the Vespel screw and nut are shown in figure 3.5.

Before mounting the coils to the cube structure, a thin wire coated in Kapton was soldered to each solder tab. The Vespel screw was inserted into the cube and through one of the central openings of the coils while using caution in order to avoid breaking the wire used to connect the two sides of that chip. The coils were then mounted to the cube using #00-80 screws, each homemade and cut precisely the right length to reach through the cube to the opposite coil and fastened with either a stainless steel #00-80 nut or by a custom Vespel nut. The Vespel nut was required only in the places where the screw could create an electrical connection to the opposite coil. Prior to assembling the the waveguide and support structure, the parts and tools used to assemble them were cleaned using water and

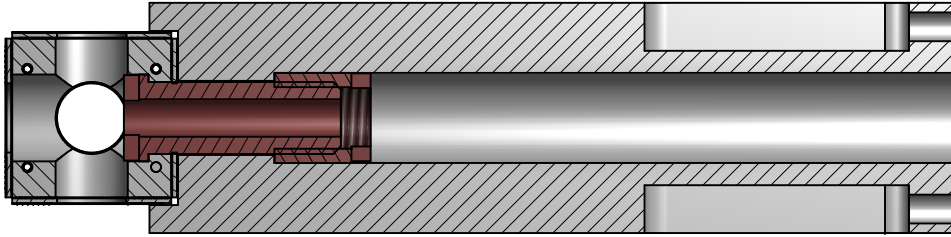


**Figure 3.5: Cutaway View of Trap Support Structure.** The Vespel screw and nut holding the cube to the rest of the support structure is represented as the darkly shaded part. The RF antenna loop is wrapped around the body of the screw between the head of the screw and the countersunk hole in the cube.

a mild detergent in an ultrasonic bath to remove any oily contaminants. These were then rinsed with acetone to remove any organic compounds. This included all of the wires used for the electrical connections. Once cleaned, the parts were only handled while wearing gloves.

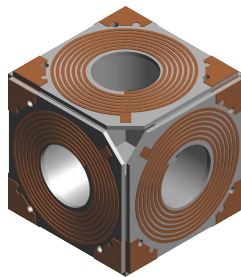


**Figure 3.6: CAD rendering of Magnetic Trap.** The screws holding the cube together are not shown.

A CAD rendering of the cube is shown in Figure 3.6. In addition to the cube assembly, a long support arm was needed to support the finished trap inside the vacuum chamber and to remove the heat produced by the trap. We elected to use a two piece arm, including a long portion made of aluminum and a short portion made out of BN. The short BN section was used to reduce the effects of eddy currents by moving any conductors further from the trap.

The cube was attached directly to the BN arm using the Vespel screw and a Vespel nut inserted from the back side of the BN arm. The BN arm was then attached to the Aluminum arm, which in turn was attached to a 4-1/2" Conflat vacuum flange via an aluminum adapter plate. The aluminum arm included vent holes to increase vacuum conductance. The mounting flange included thirteen electrical feedthroughs. Twelve feedthroughs were used to attach to the pair of wires from each of the six coils, and one SMA feedthrough was used to attach a vacuum compatible SMA cable to the RF antenna.

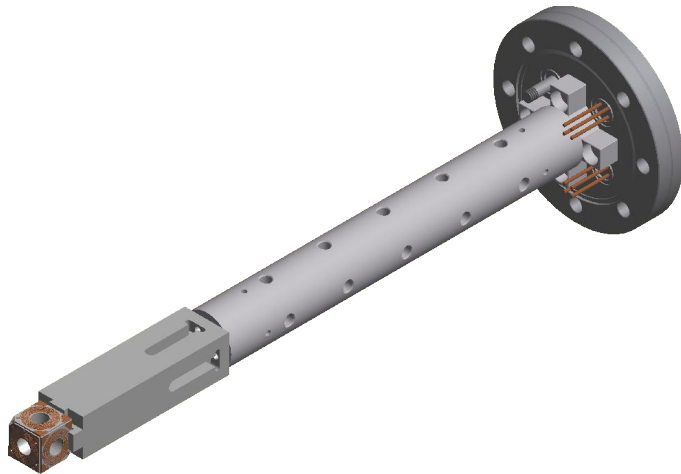


**Figure 3.7: CAD rendering of Magnetic Trap Assembly.** This rendering shows how the support structure assembly goes together. This entire assembly is inserted into the vacuum chamber.

The full mechanical assembly including the waveguide, support arm and vacuum flange are shown in 3.7. Detailed mechanical drawings of each of the parts used in this support assembly can be found in Appendix B.

### 3.2.3 Electrical Connections

Prior to completing the mechanical assembly, a small, Kapton-coated wire (30 AWG) was soldered to each of the coil's solder tabs and the other end was soldered to a slightly larger,

Kapton coated wire (22 AWG). This was done because the larger wire was stiff and the torques created on the solder pads could rip the pads from the AlN substrate. While we could have used the smaller diameter wire for the full length of the connection between the coils and the electrical feedthrough, this would have increased the resistance of the leads significantly. In using this two wire connection method, we ensured that most of the resistance was created by the coils themselves. The solder joints between the wires were covered with a short tube of alumina ( $\text{Al}_2\text{O}_3$ ) to prevent them from shorting. The wires from each coil were then twisted in pairs all the way to the vacuum flange feedthroughs in order to minimize pickup from the other wires as well as the self-inductance of the wires. Additionally, the wire used to create the RF antenna loop was soldered to the conductors in a Kapton insulated coaxial cable with an SMA connector on the opposite end. All of the wires were then restrained to the support arm by twisting bare copper wires around them and the arm. A photograph of the wired waveguide is shown in Figure 3.8.

Finally, the wires from each coil were connected to the electrical pin feedthroughs via barrel connectors. These used two screws on a barrel, one at each end, which could be tightened onto a wire from each end. The SMA connector was then fastened to the vacuum side of the SMA feedthrough. The feedthrough connections, as shown from the air side of the vacuum flange, are detailed by the combination of Figure 3.9 and Table 3.3. The first subscript used in Table 3.3 indicates the side of the cube that the coil is mounted. The second subscript indicates that if a current flows from the positive to negative pin, then a field will be created along the positive direction along the axis of symmetry of the coil.

### 3.2.4 Thermal Characterization

The thermal characteristics of the waveguide structure were examined. To gain an understanding of how much we should expect the apparatus to heat up during normal operation we needed to measure the temperature of the waveguide structure while inside the vacuum chamber. To perform this measurement, we first had to devise a means to measure this

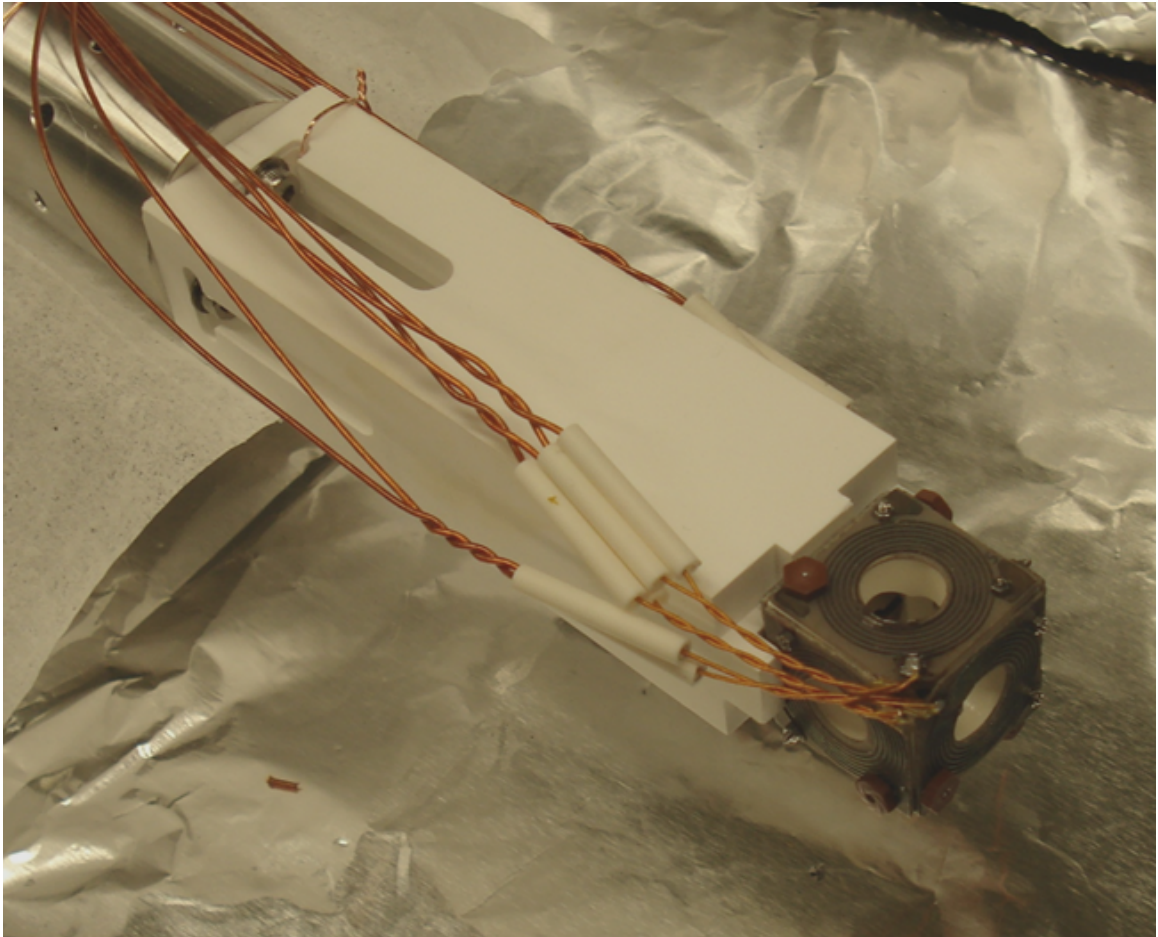


**Figure 3.8: Photograph of Assembled Magnetic Trap**

temperature. It is well known that the resistivity of copper changes with temperature. Therefore, we decided to measure the resistance of one of the coils versus temperature while outside of the vacuum chamber to calibrate this behavior.

The assumption was made that the most likely point of failure would be the coil farthest from the flange. This certainly seems reasonable since it should be nearly the highest temperature point. To perform the calibration, thermocouples were attached to several points of the waveguide and support structure. These included the coil furthest from the flange, inside the BN cube, the coil closest to the flange, the face of the BN Arm facing the waveguide, and the face of the Al Arm facing the BN Arm. To simulate the maximum power

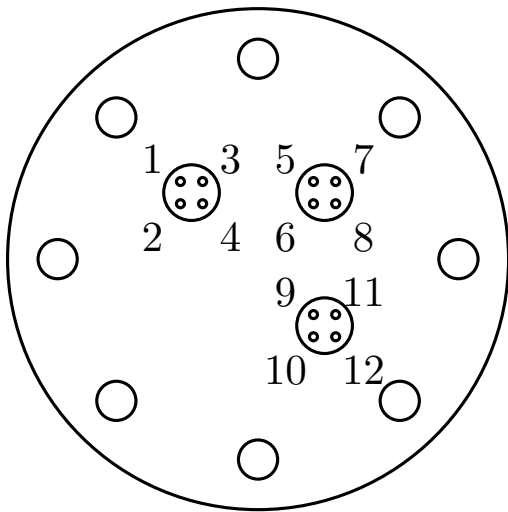


**Figure 3.9: Vacuum Flange Feedthrough Connections.** Note that this is viewed from the air side of the vacuum flange. There is also an SMA connector for the RF antenna which is not pictured here.

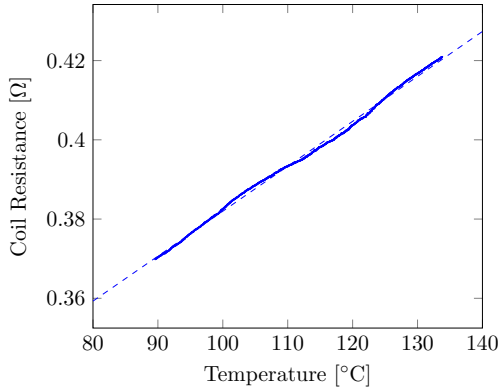
Flange Pin	Coil Connection
1	$X_{++}$
2	$X_{+-}$
3	$X_{-+}$
4	$X_{--}$
5	$Z_{++}$
6	$Z_{+-}$
7	$Z_{-+}$
8	$Z_{--}$
9	$Y_{++}$
10	$Y_{+-}$
11	$Y_{-+}$
12	$Y_{--}$

**Table 3.3: Connections between Vacuum Flange and Waveguide Coils.**(Note: X, Y, and Z refer the the symmetry axis of the coils. The first index indicates the relative position of the coil along that axis. the field produced by the coil is in the positive direction along the specified axis when current flows from + to -.)

which we expected the coils to dissipate during normal operation ( $P_{max} = 11$  W), all of the coils were connected in series on the air side of the flange and a DC current was applied such that the same total power was dissipated by the waveguide. The total resistance of the coils in series was  $R_s = 1.56 \Omega$  and so a current of  $I = 2.66$  A was required.

While performing this calibration it was discovered that the waveguide was not in good thermal contact with the support arm and needed the Vespel screw and nut to be tightened together. This was discovered from the large temperature difference between the coil closest to the flange and the face of the BN cube directly next to it. The Vespel screw and nut were tightened until the difference between the two points mentioned was negligible and did not improve with further tightening.

Upon improvement of the thermal contact between the waveguide and arm the resistance of the coil furthest from the flange ( $X_+$  in the notation of Table 3.3) was measured. This measurement was performed by monitoring the voltage across this coil and running the power supply in constant current mode ( $I = 2.66$  A). A thermocouple measured the temperature of the coil and both were recorded using an Agilent oscilloscope. The data were saved to disk and analyzed, producing the plot shown in Figure 3.10.



Fit Parameter	Value
$R_0$ [Ω]	$0.2686 \pm 0.0002$
$\alpha$ [%/° C]	$0.421 \pm 5e - 4$

**Table 3.4: Fitting Parameters for  $R_{X_+}$  vs.  $T$ .** Fitting function used:  $R(T) = R_0(1 + \alpha T)$ .

**Figure 3.10:  $R_{X_+}$  vs.  $T$ .** Measurement results for resistance versus temperature of the  $X_+$  coil.

We measured a temperature coefficient for the resistance of copper of  $\alpha = 0.421 \pm 0.001$

$\%/^{\circ}\text{C}$ , which is near the accepted value of  $\alpha = 0.394 \%/^{\circ}\text{C}$  [47]. This is a very near linear measurement and will work nicely for the intended purpose of measuring the temperature while in the vacuum chamber.

After settling on this method for temperature measurement, the waveguide and support structure were enclosed inside the vacuum chamber. The vacuum cell was then attached to an external vacuum pump-out station and the internal pressure was brought down to  $10^{-6}$  torr. The coils were again wired up in series and a DC current of  $I = 2.66$  A was run through them. Once more the power dissipated by the coils was approximately 11 W. The resistance of the  $X_+$  coil was monitored. The coil resistance topped out at  $R_{X_+max} = 0.43 \Omega$ , with corresponding temperature of  $T = 143^{\circ}$  C keeping in mind the melting point of the solder would correspond with a resistance measurement of  $R_{X_+} \approx 0.55 \Omega$ .

From these measurements and a simple thermal model, it was determined that the thermal resistance of the support structure was  $R_T = (143 + 273 \text{ K})/(11 \text{ W}) = 38 \text{ K/W}$ . This can be used to estimate the steady state temperature for a given power dissipation in the waveguide.

Additionally, we were interested in the dynamic response of the thermal system. To measure this, a square wave modulation was applied at approximately the frequency and duty cycle for normal experimental operation. The temperature was again measured using the variability of the resistance versus time, the results of which are plotted in Figure 3.11.

From the fitting parameters, it is clear that the time constant for heating and cooling are slightly different, but both are on the order of one minute. From these thermal data, we should have enough information to track the temperature of the trap. Furthermore, it is apparent that under the maximum expected power of 11 W that the trap should never be at serious risk of failure due to the solder melting.

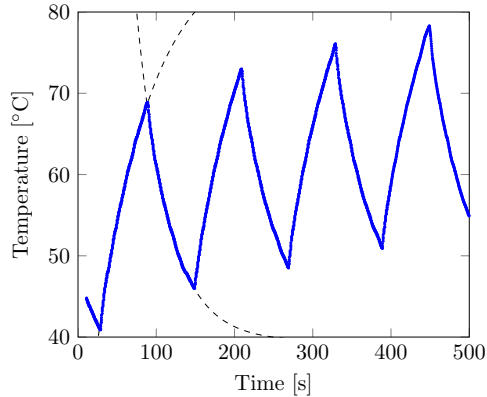


**Figure 3.11: Cycled Temperature vs. Time of Waveguide.** Shown here being run at a duty cycle of 50% at maximum power of 11 W

Fit Parameter	Heating	Cooling
$A$ [° C]	$88.0 \pm 0.6$	$39.5 \pm 0.2$
$B$ [° C]	$-45.8 \pm 0.5$	$27.9 \pm 0.1$
$t_0$ [s]	29	90
$\tau$ [s]	$69 \pm 1$	$40.3 \pm 0.4$

**Table 3.5: Fitting Parameters for Temperature vs. Time of Waveguide.** Fitting function used:  $T(t) = A + B \exp[-(t - t_0)/\tau]$ .

### 3.3 Electronics

Upon completing the mechanical and electrical assembly of the portion of the trap inside the vacuum chamber, we needed to develop a means of driving the coils to produce the potential discussed in section 3.1. We need to supply the currents from equation (3.12).

#### 3.3.1 Signal Generation

To create these signals requires the ability to have two quadrature sources, each yielding a sine and cosine signal at a given frequency. In other words, we need to create both sine and cosine signals at both  $\Omega_1$  and  $\Omega_2$ . Additionally, we require that these two frequencies need to be different from one another. To produce the initial cosine function at each frequency, we can simply use a function generator. We elected to utilize two Agilent function generators (Model # 33210A). One of the function generators was set to operate at  $f_1 = 10$  kHz and the other was set to operate at  $f_2 = 1$  kHz. To produce the sine signal from the cosine signal a variable phase shifter was used which would allow fine adjustment of the phase shift between the nominal sine and cosine functions without affecting the amplitude of the

signal. The circuit diagram for this adjustable phase shifter is displayed in Figure 3.12.

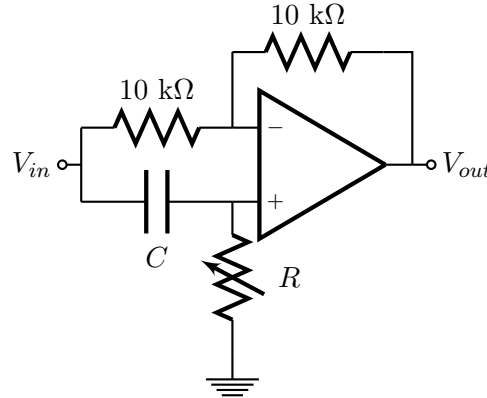


**Figure 3.12: Phase Shifter Circuit Diagram.** The values of  $R$  and  $C$  are set such that the nominal phase shift produced is  $90^\circ$ .

A quick analysis of the circuit will yield the result that  $V_{out}/V_{in} = Ge^{i\phi}$ . The gain is unity,  $G = 1$ ; however, the phase shift depends on the values of  $R$  and  $C$ .

$$\phi = \tan^{-1} \left( \frac{\omega}{\omega_0} \right) = \tan^{-1} \left( \frac{\omega}{RC} \right) \quad (3.19)$$

By selecting  $RC = 2\pi f$  for the two frequencies, a nominal  $90^\circ$  phase shift is produced. By making the resistor  $R$  a potentiometer of appropriate size, the phase shift can be tuned. With this we have the ability to produce the quadrature signals needed. To implement the phase shifters, we used AD711 low-noise, precision operational amplifiers.

It is also required that the signals be multiplied together to produce the complex currents. This could be achieved in many ways, but we used analog multiplier integrated circuits. Analog Devices AD534KDZ multipliers were selected for this task due to their high-precision and low noise floor. The basic operation of these chips is to take two signals,  $V_1$  and  $V_2$ , and output the product with some scaling factor. In this case,  $V_{out} = (0.1 V^{-1})V_1V_2$ . By multiplying the signals of the quadrature oscillators together in the proper fashion, the desired outputs can be achieved. Two voltages,  $V_0$  and  $V_1$  act as input controls for the bias and quadrupole strengths respectively. With the addition of buffer amplifiers

(AD711 wired as follows), we were able to construct the circuit shown in block diagram form in Figure 3.13. For a more detailed circuit diagram, refer to Appendix C.

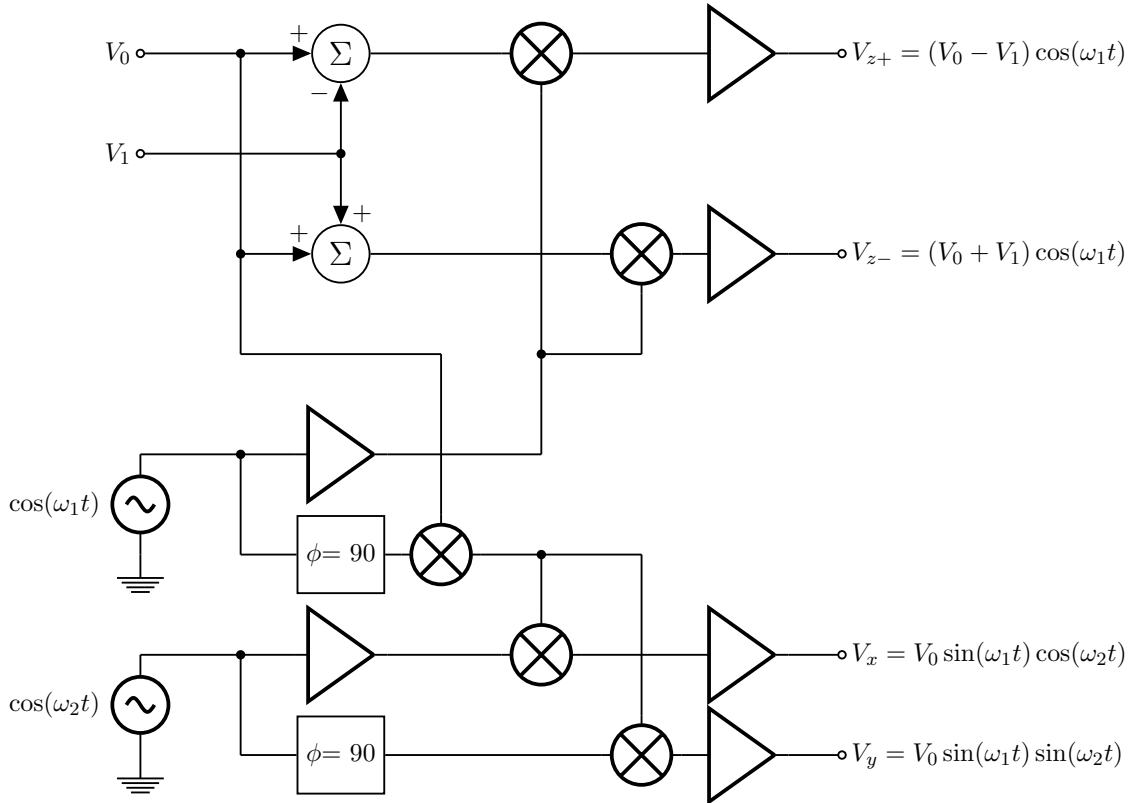


**Figure 3.13: Block Diagram of Waveguide Signal Generators.** The triangular elements are buffer amplifiers. The circles with  $\Sigma$  written in them are summing amplifiers, and the square boxes are variable phase shifters. The circles with X written in them are the multipliers. The inputs for the multiplier are to the left and either above or below. The output of the multiplier is always to the right.

The circuit takes the two control voltages and the inputs from the two function generators and produces an output for each waveguide signal. The end results are the voltage outputs shown in equation 3.20.

$$\begin{aligned}
 V_x &= V_0 \sin(\omega_1 t) \cos(\omega_2 t) \\
 V_y &= V_0 \sin(\omega_1 t) \sin(\omega_2 t) \\
 V_{z\pm} &= (V_0 \mp V_1) \cos(\omega_1 t)
 \end{aligned}
 \tag{3.20}$$

It should be noted that there are eight potentiometers in the circuit to allow for the

independent balancing of the voltages. Two to balance the  $Z_{\pm}$  bias and two to balance the  $Z_{\pm}$  quad. Another four to fine tune the balance between the four quadrature oscillator outputs. This is overparameterized and offers more than enough adjustments to balance all of the signals relative to one another. Additionally, there are two potentiometers to adjust the phase shifts for the quadrature oscillators. With this we only need the ability to drive currents proportional to these voltages in a controlled way. To do this, we constructed a voltage controlled current source.

### 3.3.2 Voltage Controlled Current Source

With the proper signals generated, we need only to convert these to currents in the coil. This is achieved by constructing a voltage controlled current source using a high-powered amplifier. The circuit used to accomplish this goal is shown in figure 3.14.

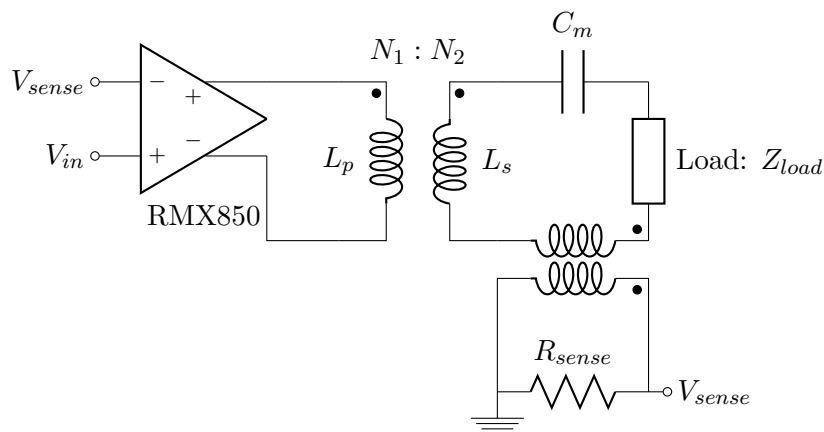


**Figure 3.14: Trap Amplifier Circuit.** This converts the voltage applied to a current in the load. The sense voltage is connected back to the negative input of the amplifier.

The QSC RMX850 is an audio amplifier capable of driving two channels in the audio frequency range (50 Hz - 20kHz). It is a fully differential amplifier with adjustable gain from 0 dB to 30 dB. The amplifiers are designed to drive a load of approximately 4-8  $\Omega$ . Therefore, it was necessary to implement some circuitry to match our coil impedance to the amplifier. The impedance was measured for all of the coils. In the configuration used

to create the AC bias and quad, the  $X$  and  $Y$  coils are driven in series and the two  $Z$  coils are driven independently. As such, the impedance measurements for the 4 distinct phases as measured using an Agilent  $LCR$  meter at 10 kHz are shown in table 3.6.

Signal	$R$ [ $\Omega$ ]	$L$ [ $\mu\text{H}$ ]
$X$	0.5593	7.137
$Y$	0.5509	7.344
$Z_+$	0.2974	3.583
$Z_-$	0.3023	3.620

**Table 3.6:** Uncompensated Trap Signal Impedance Measurements. Measured the the feedthrough connections after connecting the x and y coils in series.

To match the coil impedance to the design impedance of the amplifier, custom transformers were built. The turn ratios for the transformers were  $n_x = n_y = 21 : 6$  and  $n_z = 25 : 5$ . Additionally, a capacitor,  $C_m$ , was placed in series with the transformer as shown in figure 3.14. This was done to cancel the inductive reactance at the drive frequency so that the amplifier would effectively be driving a purely resistive load.

To select the values of the capacitors, the coils were connected to the secondary side of the transformers and the impedance was measured once again using the Agilent  $LCR$  meter at 10 kHz. The impedance measurements on the primary side of the transformer and the capacitance used to null the reactance,  $C = \frac{1}{\omega^2 L}$  for  $\omega = 2\pi(10 \text{ kHz})$ , are shown in table 3.7.

Signal	$R$ [ $\Omega$ ]	$L$ [ $\mu\text{H}$ ]	$C$ [ $\mu\text{F}$ ]	$Z$ [ $\Omega$ ]	$\phi$ [ $^\circ$ ]
$X$	6.365	17.68	14.3	6.461	-9.8
$Y$	6.446	16.4	15.4	6.528	9.0
$Z_+$	7.588	33.58	7.54	7.876	-15.5
$Z_-$	7.385	32.84	7.71	7.668	15.6

**Table 3.7:** Waveguide Phase Compensated Impedance Measurements.  $L$  and  $C$  values were measured on the load side of the transformer, whereas  $R$  was measured on the primary side. Here  $Z$  is the impedance measured at 10 kHz with the compensating capacitor included from the primary side of the transformer.  $\phi$  is the measured phase shift. Clearly, the compensation is imperfect.

Incidentally, the selection of components for this voltage controlled, current source set limitations on the frequencies which the function generators could be used. Since the load appears as an *RLC* resonator, the sum and difference frequencies ( $\Omega_1 \pm \Omega_2$ ) had to be within the FWHM of the resonance which was approximately 2 kHz. Otherwise, the signal would be severely distorted.

Finally, a current sense transformer with a turn ratio of  $n_{sense} = 1 : 200$  was used on the secondary (load) side of the transformer to measure the current through the load for each of the four signals. A wire-wound resistor was placed across the secondary side of this sense transformer with a value of  $200 \Omega$ , yielding a voltage  $V_{sense} = 1 \text{ V/A}$ . Therefore, due to the variability in the load impedance, we elected to run the circuit with negative feedback to stabilize the current. This was done by taking the load current sense voltage  $V_{sense}$  and returning it to the negative input of the RMX850 audio amplifier. This also has the added benefit of minimizing the impact of load impedance variations due to temperature fluctuations.

One important consideration was that the total loop gain of the circuit needed to go to unity at a frequency below where the phase shifts in the loop reached  $180^\circ$ . If the gain exceeds unity, the circuit will “ring” at the frequency where the phase shifts add to  $180^\circ$ . The maximum gain setting necessary to prevent this ringing was determined empirically to be 26 dB for all of the amplifiers. This value matches well with the theoretical value of 26 dB. This analysis largely follows that used by Baronowski et. al. [48].

### 3.4 Characterization

Finally, with all of the mechanical and electrical systems in place, we were able to characterize the trap. To do this we loaded atoms into the trap to determine its performance in situ. Several important details needed to be determined including the bias field scaling, the quad strength needed to cancel gravity, and whether the trap really was in fact cylindrically

symmetric.

To estimate the bias field strength, we look no further than the potential for the TOP trap, equation (2.7). From this equation, we see that the offset in the potential minimum is directly proportional to the bias field. Therefore, the bottom frequency of the trap, or the RF frequency during evaporation which causes the maximum population loss, is proportional to the bias strength. If we can make an accurate measurement of this frequency, then we can in turn gain information on the bias strength,  $2\hbar\omega_{bottom} = \mu_B B_0$ . To do this, an RF spectroscopy measurement was performed by turning on the RF at a constant level for some set duration. The RF frequency was then varied and the number of atoms present during absorption imaging was recorded. This produced a very noisy set of data due to the fluctuations in the initial number of atoms before the RF was applied; however, there was a clear dip at  $f_{bottom} = 14.83 \pm 0.06$  MHz. This gives an estimate of the bias field strength of  $B_0 = 21.20 \pm 0.09$  Gauss. The current used for the bias in this experiment was  $9.2 A_{pp}$ . This gives a bias field versus current of  $B_0/I_0 = 4.61 \pm 0.01$  Gauss/Amp. This is close to the value computed using the simple model of two coils of  $B_0/I_0 = 4.48$  Gauss/Amp. Additionally, we know that the maximum bias field that we can apply with our current setup is approximately 23 Gauss.

As a next step, the atoms were loaded into the new, cylindrical trap. To do this, the trap had to be adiabatically deformed from the TOP trap used in the evaporation stage into the new trap. Additionally, the centers of the two traps needed to be very close to coincident. If the trap is deformed either non-adiabatically or the two traps are not coincident, then the atom's motion can be excited. This will result in the atoms oscillating in the final trap. Therefore, in order to peak up these effects, the residual oscillations of the condensate were minimized. The atoms were imaged from both the top ( $z$ ) and side ( $y$ ) directions so that the oscillations of the atoms in the trap could be monitored in all three dimensions. To center the two traps on one another an oscillation curve was first taken for the condensate in the new trap. To do this, the atoms were loaded into the new trap and the time was

adjusted between the time the trap was loaded and before the image was taken. Therefore we were able to gain insight into the motion of the atoms in the trap. The data were fit to a cosine function in each direction and the center of oscillation could be determined from the fit. Upon determining the center of the new trap, the center of the TOP trap was measured in a similar way. This measurement was much more straightforward since the atoms weren't visibly oscillating. The translation stage to which the large, DC spherical quadrupole electromagnets are mounted was adjusted until the two traps were centered on top of one another. To align the traps vertically, the coils had to be adjusted up and down as well. The position of the coils was monitored with dial calipers along the track as well as a ruler for the vertical direction during this adjustment procedure. This gave us a quantifiable means of aligning the traps.

After centering the two traps on one another, we then proceeded to optimize the transfer between the two traps. To do this, we lowered the strength of the DC quadrupole field while increasing the strength of the AC quadrupole field. The optimum control sequence to switch between the two was determined empirically. The sequence consists of several linear ramps of the trapping configuration. An oscillation curve was taken after partially loading the new trap and the duration for each step was chosen to minimize the oscillations. The final sequence for switching between the TOP trap and the new trap is shown in table 3.8.

We then sought to adjust the quadrupole voltage to compensate for gravity. To induce motion in the direction of gravity, the AC quadrupole voltage was set to zero throughout the loading sequence and non-adiabatically switched on in the final trap configuration. This caused the atoms to start falling and when the support against gravity was switched on, the atoms would oscillate in the  $z$  direction. It can be seen from the model of the potential, equation (3.10), that the equilibrium condition is given by

$$\frac{\partial U}{\partial z} = \left( mg - \frac{\mu_B B'_1}{2} \right) + m\omega_z^2 z_0 = 0 \quad (3.21)$$

Duration [ms]	DC Quad [V]	AC Bias [V]	AC Quad [V]
0.001	10.0	3.0	0.0
200r	8.0	3.0	8.0
400r	1.0	3.0	8.0
1000r	0.8	3.0	8.0
2000r	0.4	3.0	8.0
3000r	0.1	3.0	8.0
6000r	0.0	3.0	8.0
6000r	0.0	$V_f$	8.0

**Table 3.8: Trap Loading Sequence.** This is the transfer sequence between the TOP trap and the new trap. The first line indicates the final configuration after evaporation. The small “r” denotes that the analog voltages are ramped linearly over the duration noted.  $V_f$  is the final bias voltage, which is adjusted depending upon the desired trap strength.

This gives the equilibrium position,  $z_0$  below.

$$z_0 = \frac{\mu_B B_1'}{2m\omega_z^2} \left( 1 - \frac{2mg}{\mu_B B_1'} \right) \quad (3.22)$$

So by determining the center of oscillations ( $z_0$ ) at varying bias strengths ( $B_0$ ) for fixed quad strength ( $B_1'$ ), the approximate quadrupole strength can be determined. If the quadrupole strength is properly set to balance gravity (so  $z_0 = 0$ ), then the center of oscillations should remain stationary as the bias is changed. This process was done iteratively until arriving at the final setting of  $V_{quad_{AC}} = 8.0$  V. This corresponds to a current of  $I_1 = 4.0$  A, which is almost exactly what was predicted by the numerical model of the trap ( $I_1 = 3.96$  A).

The final task was to determine the trapping frequencies as a function of bias strength. To do this, the oscillations were again monitored in both directions. The center of the TOP trap was purposely displaced from that of the new trap and the loading sequence was made non-adiabatic in order to induce oscillations. These oscillations were then observed by the same procedure as before. This was performed for various bias strengths.

These data were fit with sinusoidal functions and the fitting parameters included the trap frequencies. The trap frequencies were then plotted versus bias voltage and the results are shown in Figure 3.15.

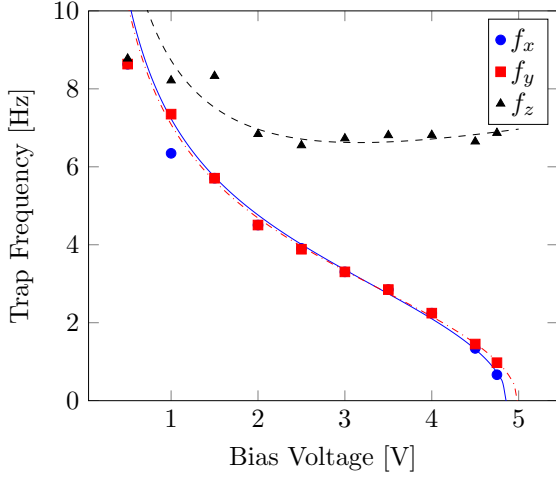


**Figure 3.15: Measured Trap Frequencies.** Trap frequencies measured at varying bias field strengths.

Axis	A [ $\text{V}\cdot\text{Hz}^2$ ]	B [ $\text{Hz}^2/\text{V}$ ]
X	$43.5 \pm 2.5$	$-1.7 \pm 0.2$
Y	$46.0 \pm 2.9$	$-1.8 \pm 0.2$
Z	$48.3 \pm 6.4$	$9.0 \pm 1.3$

**Table 3.9: Trap Frequency Fit Parameters.**Fitting Function:

$$f(V_{bias}) = \sqrt{\frac{A}{V_{bias}} + BV_{bias}}$$

The fitting parameters used in the frequency scaling model can be related back to the quadrupole strength and the curvature of the bias from equation (3.18). From these relations, it is determined that  $B'_1 = 33.7 \pm 0.4$  Gauss/cm and  $\gamma = 2.8 \pm 1.0$  cm<sup>-2</sup>. To recap the previous results from the numerical simulation of the new trap,  $B'_1 = 30.5 \pm 0.1$  Gauss/cm and  $\gamma = 3.96 \pm 0.02$ .

### 3.5 Conclusions

In summary, a new and novel magnetic trap has been developed which offers a harmonic trapping potential with cylindrical symmetry and support against gravity. The atomic lifetime in this trap is well beyond a minute. Furthermore, the trapping strength can be adjusted by tuning the bias field strength, which will allow for scalability when it comes time to implement the improved Sagnac interferometer.

# 4 | INTERFEROMETRY

Now that we have a BEC and are able to load it into our magnetic trap, we are ready to begin coherently manipulating the atoms in order to perform some interferometric measurements. In addition to the application of the gravimeter, this also opens the possibility of creating interferometers in which the output phase depends upon the atomic recoil frequency. In the next sections, the theory of this asymmetric process will be developed in further detail and discussion of two interferometers which have been implemented using this pulse technique will be explored.

## 4.1 Asymmetric Splitting/Recombination

To implement the asymmetric splitting necessary for the gravimeter proposed in section 1.5, we consider the method proposed in [49, 50]. This method involves using two counter-propagating beams at slightly different frequencies to implement a moving optical Bragg grating. In this sense, the standing wave created by the two beams actually moves with a group velocity in the direction that we wish to kick the atoms. This can also be understood from the energy-momentum diagram shown in figure 4.1. The atoms absorb a photon from the beam coming from the left and then emit a photon into the beam coming from the right via stimulated emission. This process conserves both energy and momentum and results in the atoms gaining  $2\hbar k$  momentum from the photon absorption-emission process.

In addition to the application of the gravimeter, this also opens the possibility of creating

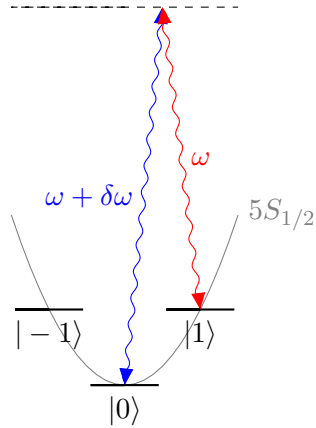


**Figure 4.1: Energy-momentum Diagram for Asymmetric Split/Recombination Pulse.** Two counter-propagating lasers with frequencies  $\omega$  and  $\omega + \delta\omega$  are used to create a standing wave. The atoms are kicked in the direction of the higher energy beam.

interferometers in which the output phase depends upon the atomic recoil frequency. In the next, subsections, I will develop the theory of this asymmetric process in further detail and discuss two interferometers which have been implemented using this pulse technique.

#### 4.1.1 Theory

To develop the theoretical grounds for the asymmetric splitting, we can begin with the one-dimensional Schrödinger equation:

$$i\hbar \frac{\partial \Psi}{\partial t} = H\Psi = \left( -\frac{\hbar}{2m} \frac{\partial^2}{\partial z^2} + V(z) \right) \Psi \quad (4.1)$$

Here  $H$  is the Hamiltonian,  $V(z)$  is the potential energy along the  $z$  direction, and  $\Psi$  is the atomic wavefunction. If we apply a two color standing wave such that the beam from the left of the atoms has a frequency  $\omega + \delta\omega$  and the beam hitting the atoms from the right side has angular frequency  $\omega$ , then the atoms will experience a potential due to the AC Stark shift. The potential energy is as follows:

$$V(z) = \hbar\Gamma \frac{I(z)}{I_{sat}} \frac{\Gamma}{4\Delta} = -\frac{1}{2}\alpha\langle E^2 \rangle \quad (4.2)$$

Here,  $\Delta$  is the laser detuning from the resonant atomic transition,  $\Gamma$  is the natural linewidth of the atomic transition,  $I_{sat}$  is the saturation intensity,  $I(z)$  is the combined light intensity from the two laser beams as a function of position  $z$ ,  $\alpha$  is the polarizability, and  $E$  is the electric field.

We know that the intensity is proportional to the square of the magnitude of the electric field vector. So we should first determine this quantity for the standing wave described above. For the sake of simplicity, let's assume that the beams are actually plane waves, which is a fair assumption if the Gaussian beams are well-collimated and large compared to the atoms in size. In this case, the total electric field at the location of the atoms can be written as:

$$\mathbf{E}_{tot} = \mathbf{E}_1 e^{i(kz - \omega t - \delta\omega t)} + \mathbf{E}_2 e^{i(-kz - \omega t - \alpha)} \quad (4.3)$$

Here  $\mathbf{E}_1$  is the electric field from the beam traveling from left to right,  $\mathbf{E}_2$  the electric field due to the beam traveling from right to left,  $\omega + \delta\omega$  is the frequency of the right moving beam,  $\omega$  is the frequency of the left traveling beam, and  $\alpha$  is the relative phase difference between the two beams and no longer represents the polarizability. It is worth noting that  $|\mathbf{k}_1| \approx |\mathbf{k}_2| = k$ . To determine the potential due to the AC Stark shift, we need to know the intensity as a function of position. This is given in equation (4.4):

$$I \propto |\mathbf{E}_{tot}|^2 = |\mathbf{E}_1|^2 + |\mathbf{E}_2|^2 + 2\mathbf{E}_1 \cdot \mathbf{E}_2 \cos(2kz - \delta\omega t + \alpha) \quad (4.4)$$

Thus, we can simply write the potential as shown in equation (4.5).

$$V(z) = \hbar\beta_0 + \hbar\beta \cos(2kz - \delta\omega t + \alpha) \quad (4.5)$$

The constant offset will shift all of the energy levels by the same amount, and will therefore not contribute to the overall evolution of the atomic wavefunction. Therefore, we can drop the constant term and only keep the term that changes with  $z$ . The resulting, simplified potential is therefore

$$V(z) = \hbar\beta \cos(2kz - \delta\omega t + \alpha) \quad (4.6)$$

where  $\beta$  is related to the two beam intensities,  $I_1$  and  $I_2$ , using equation (4.7).

$$\beta = \frac{\Gamma^2 \sqrt{I_1 I_2}}{2\Delta I_{sat}} \quad (4.7)$$

With these simplifications, Schrödinger's equation becomes:

$$i\hbar \frac{\partial \Psi}{\partial t} = \left[ -\frac{\hbar^2}{2m} \frac{\partial^2}{\partial z^2} + \hbar\beta \cos(2kz - \delta\omega t + \alpha) \right] \Psi \quad (4.8)$$

To determine the wavefunction, we can utilize the Bloch Expansion, i.e. equation (4.9).

$$\Psi = \sum_{n=-\infty}^{\infty} c_n(t) e^{i(2nk+\kappa)z} = \sum_{n=-\infty}^{\infty} c_n |n\rangle \quad (4.9)$$

Here  $\hbar\kappa$  is an offset in the momentum of the waves and  $|n\rangle$  represents a particle with momentum of  $2n\hbar k$ . Physically, this corresponds to the initial momentum of the atoms. The  $2\hbar k$  comes from the fact that this is a two photon transition. In the Bloch expansion, Schrödinger's equation yields a set of infinite, coupled differential equations relating the coefficients,  $c_n$ .

$$i\hbar \dot{c}_n |n\rangle = \left[ \frac{\hbar^2}{2m} (2nk + \kappa)^2 + \hbar\beta \left( e^{i(2kz - \delta\omega t + \alpha)} + e^{-i(2kz - \delta\omega t + \alpha)} \right) \right] c_n |n\rangle \quad (4.10)$$

$$i\hbar \dot{c}_n |n\rangle = \frac{\hbar^2}{2m} (2nk + \kappa)^2 c_n |n\rangle + \hbar\beta \left( e^{i(\alpha - \delta\omega t)} c_n |n+1\rangle + e^{-i(\alpha - \delta\omega t)} c_n |n-1\rangle \right) \quad (4.11)$$

If we multiply this equation by  $\langle m|$ , then we can determine the  $m^{\text{th}}$  equation:

$$i\hbar \dot{c}_n \delta_{m,n} = \frac{\hbar^2}{2m} (2nk + \kappa)^2 c_n \delta_{m,n} + \hbar\beta \left( e^{i(\alpha - \delta\omega t)} c_n \delta_{m,n+1} + e^{-i(\alpha - \delta\omega t)} c_n \delta_{m,n-1} \right) \quad (4.12)$$

Therefore the infinite series of coupled ODE's is given by the representative equation:

$$i\hbar\dot{c}_n = \frac{\hbar^2 k}{2m}(2n + \kappa/k)^2 c_n + \hbar\beta \left( e^{i(\alpha - \delta\omega t)} c_{n-1} + e^{-i(\alpha - \delta\omega t)} c_{n+1} \right) \quad (4.13)$$

This system of infinite, coupled ODE's can be readily solved by truncating the system at a reasonable momentum state and using a mathematical suite such as MATLAB to solve them numerically for a given set of initial conditions, i.e.  $c_n(0)$ . However, to gain insight into the splitting/recombination, one can simplify the calculation by transforming these equations into the interaction picture by absorbing the time varying bit into the state vectors. Let,  $c_n(t) = d_n(t)e^{-iE_n t/\hbar}$ , where  $d_n(t)$  is a slowly varying function of time. Substituting this into equation (4.13) yields

$$i\hbar\dot{d}_n = \frac{\hbar\beta}{2} \left\{ d_{n-1} e^{i[\alpha + (E_n - E_{n-1} - \delta\omega)t]} + d_{n+1} e^{-i[\alpha + (E_{n+1} - E_n - \delta\omega)t]} \right\} \quad (4.14)$$

If  $\delta\omega \approx E_{n+1} - E_n$  and  $\beta \ll E_{n+1} - E_n$ , then we can drop all of the rapidly oscillating terms because they will average out and only keep the slowly varying terms (this is the rotating-wave approximation). This leaves only two coupled states,  $|n\rangle$  and  $|n+1\rangle$ . Therefore, we can approximate the system as a two-level system and the Hamiltonian becomes

$$H = \frac{\hbar}{2} \begin{bmatrix} 2\omega_R \left( 2(n+1) + \frac{\kappa}{k} \right)^2 & \beta e^{i[\alpha - \delta\omega t]} \\ \beta e^{-i[\alpha - \delta\omega t]} & 2\omega_R \left( 2n + \frac{\kappa}{k} \right)^2 \end{bmatrix} \quad (4.15)$$

Here  $\omega_R \equiv \frac{\hbar k^2}{2m}$  is the recoil frequency from absorbing a single photon. If we change our state definitions, such that one of the states has its phase evolving with the standing wave phase as shown in equation (4.16),

$$|\Psi\rangle = \begin{bmatrix} c_{n+1} \\ c_n \end{bmatrix} = \begin{bmatrix} d_{n+1} e^{i\delta\omega t} \\ d_n \end{bmatrix} \quad (4.16)$$

then this reduces to a normal two-level system, with detuning  $\Delta \equiv 4\hbar\omega_R(2n+1 + \kappa/k) - \delta\omega$

and interaction strength  $\Omega = \beta e^{i\alpha}$ . The results of such a system have been detailed by many sources[34]. I will summarize the relevant results here.

The two-level system with states  $|g\rangle$  and  $|e\rangle$  and is governed by the Hamiltonian shown in equation (4.17).

$$H = \frac{\hbar}{2} \begin{bmatrix} 2\Delta & \Omega \\ \Omega^* & 0 \end{bmatrix} \quad (4.17)$$

The eigen-energies of the Hamiltonian are given by

$$E_{\pm} = \frac{\hbar}{2} (\Delta \pm \Omega_R) \quad (4.18)$$

where  $\Omega_R \equiv \sqrt{|\Omega|^2 + \Delta^2}$ . The eigenvectors can be found in the basis of  $|g\rangle$  and  $|e\rangle$  written in the form

$$|\pm\rangle = \begin{bmatrix} c_e \\ c_g \end{bmatrix} = \frac{1}{\sqrt{2\Omega_R(\Omega_R \pm \Delta)}} \begin{bmatrix} \Omega_R \pm \Delta \\ \pm\Omega^* \end{bmatrix} \quad (4.19)$$

To understand how the states evolve in time, the propagator,  $U(t) \equiv e^{-iHt/\hbar}$ , can be used. In the basis of  $|+\rangle$  and  $|-\rangle$ , this can be written quite simply as

$$U(t) = \begin{bmatrix} e^{-iE_+t/\hbar} & 0 \\ 0 & e^{-iE_-t/\hbar} \end{bmatrix} \quad (4.20)$$

While this is trivial to calculate, we really care about the propagator in the basis of  $|g\rangle$  and  $|e\rangle$  and therefore need to transform back to this basis. This can be done with a few algebraic steps, which I will skip here, to obtain the very useful result

$$U(t) = e^{-i\Delta t/2} \begin{bmatrix} \cos\left(\frac{\Omega_R t}{2}\right) - i\frac{\Delta}{\Omega_R} \sin\left(\frac{\Omega_R t}{2}\right) & -i\frac{\Omega}{\Omega_R} \sin\left(\frac{\Omega_R t}{2}\right) \\ -i\frac{\Omega^*}{\Omega_R} \sin\left(\frac{\Omega_R t}{2}\right) & \cos\left(\frac{\Omega_R t}{2}\right) + i\frac{\Delta}{\Omega_R} \sin\left(\frac{\Omega_R t}{2}\right) \end{bmatrix} \quad (4.21)$$

which we can use to calculate the time evolution of the of the state vector by  $|\psi(t)\rangle = U(t)|\psi(0)\rangle$ .

It is worth noting that a change in the initial velocity of the atoms acts in the same way as a detuning of the system since  $\Delta = 4\hbar\omega_R(2n+1+\kappa/k) - \delta\omega$ . If the initial velocity is large, or the detuning is far from the resonant condition, then the rotating wave approximation made previously to reduce the system to two levels will typically break down.

For our experiments, we will start with the atoms at rest or in state  $|0\rangle$ . If we set the detuning between the two Bragg beams such that  $\delta\omega = E_1 - E_0$ , then we can couple to the state moving with  $+2\hbar k$  momentum in the direction of the higher frequency beam.

Thus, if we start with atoms in  $|0\rangle$  and apply a  $\pi/2$ -pulse, i.e.  $\beta t_s = \pi/2$ , then we should be able to create a 50-50 beam-splitter which leaves half of the atoms at rest and kicks half of the atoms into the  $|1\rangle$  state, i.e.  $|0\rangle \rightarrow |0\rangle + |1\rangle$ . It follows from equation 4.21 that if the directions of the two beams are reversed or the relative detunings altered such that  $\delta\omega = E_0 - E_1$ , then the transition can be driven in the opposite direction.

While this simplified picture is useful in our understanding of the underlying physics it is incomplete. We have neglected couplings to the other momentum states as well as the effects of the detuning between the lasers and the initial velocity of the atoms. To include these effects, we go back to the infinite series of coupled, differential equations from equation (4.13) and rewrite them in the following form:

$$\dot{c}_n = \frac{\hbar}{2m}(2nk + \kappa)^2 c_n + \beta \left( e^{i(\alpha - \delta\omega t)} c_{n-1} + e^{-i(\alpha - \delta\omega t)} c_{n+1} \right) \quad (4.22)$$

By truncating the basis at some reasonable level this system of equations can be numerically integrated using MATLAB. To determine how many momentum states are necessary, we plot the fraction of atoms in each state versus the relevant parameters,  $\beta$  and  $t$ , the time that the light is pulsed on. We examine the ideal case where the detuning is set to the energy splitting between the  $|0\rangle$  and  $|\pm 1\rangle$  states, and plot the probability for the atoms to be in the various momentum states versus  $\beta$  and  $t$ , the pulse time, as shown in Figure 4.2. In the case that the intensity remains low, we see that our approximate 2-level solution is quite good and the population very nearly Rabi oscillates between the  $|0\rangle$  and  $|1\rangle$  state.

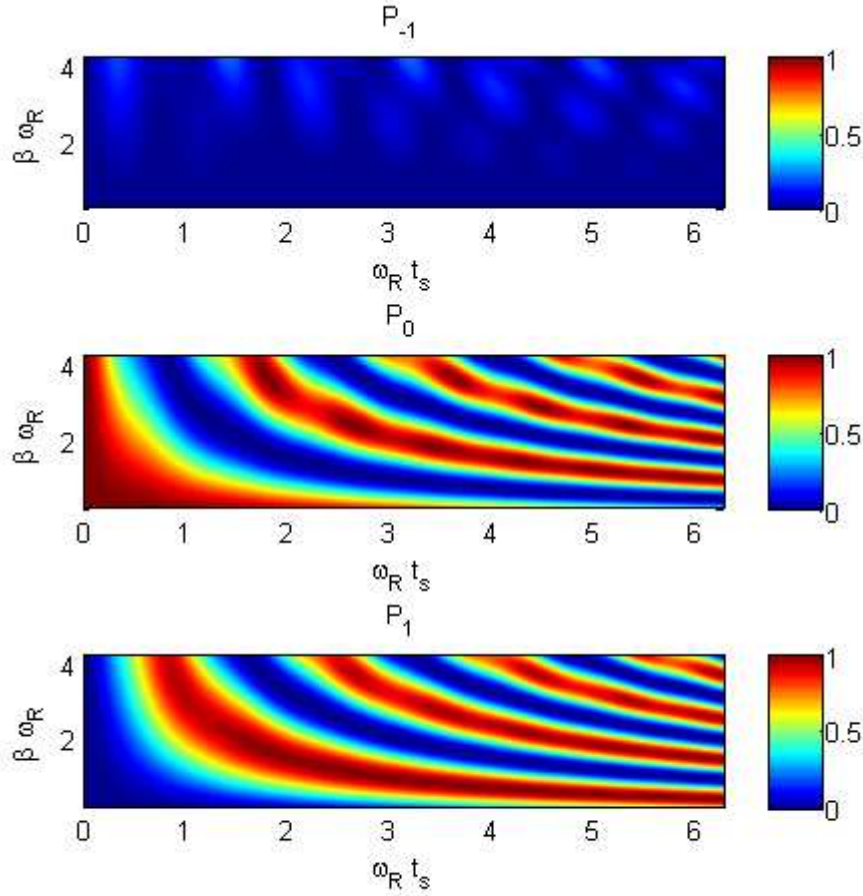
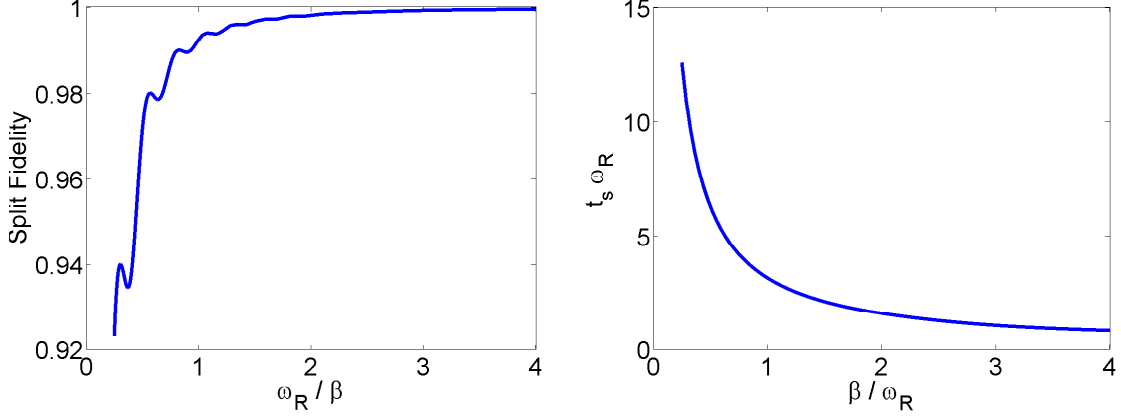


**Figure 4.2: Split Probabilities.** These plots show the population of the state  $| -1 \rangle$ ,  $| 0 \rangle$ , and  $| 1 \rangle$  versus pulse intensity and duration.

However, as the intensity increases, that approximation begins to break down since more atoms are transferred to the other momentum states and as such they can no longer be neglected.

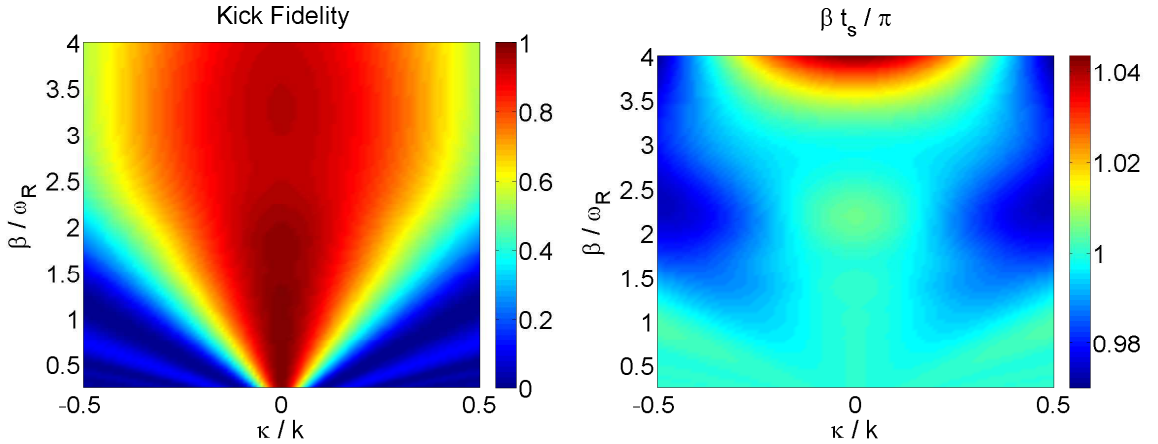
It is worth noting that as  $\beta$  is increased, the fractional population in the incorrect momentum state  $| -1 \rangle$  is no longer negligible. To this point the initial velocity (or detuning for that matter), has been neglected. If we define the fidelity,  $F$ , of our kick operation as the fraction of the atoms that make it into the desired state, i.e.  $F = |\langle \psi | 1 \rangle|^2$ . We then elect to optimize the pulse duration for a given  $\beta$  by increasing the time from zero to the

first maximum. These results are shown in Figures 4.3a and 4.3b respectively.



(a) Intensity Dependence of Optimal Pulse Fidelity.

(b) Intensity Dependence of Optimal Pulse Duration.



(c) Intensity and Initial Velocity Dependence of Fidelity.

(d) Velocity and Intensity Dependence of  $\beta t_s$ .

**Figure 4.3: Split Pulse Numerical Calculation Results**

Additionally, the dependence of the fidelity and the pulse duration were examined as a function of pulse intensity parameter,  $\beta$ , and initial velocity parameter,  $\kappa$ , with fixed  $\delta\omega = 4\omega_R$ . To do this, the pulse duration was optimized for each value of  $\beta$  and  $\kappa$  such that the fidelity of the splitting operation was maximized. The results of this optimization are shown in Figures 4.3c and 4.3d respectively.

From these plots, there are two trends that will play a vital role in the experiments

that were performed. First, as I've already mentioned, the fidelity decreases as  $\beta$  increases due to losses into the weakly coupled states, which the simple two-level model neglects. Furthermore, at lower intensities, the width of the fidelity peak in velocity becomes quite narrow and expands nearly linearly with pulse duration. Both of these phenomena can be explained by a simple argument of the frequency width of the pulse. For a very short pulse, the frequency width is quite large and the pulse will therefore couple states with large energy differences, or in this case the different momentum states. On the contrary, long pulses are quite narrow in frequency-space and will therefore only couple states that are nearly degenerate.

### 4.1.2 Implementation

In order to implement the asymmetric splitting of the atoms, it was necessary to develop a new Bragg beam setup. This was largely the focus of Eun Oh's dissertation [23] and so I will not focus too heavily on the details. However, I will discuss the basic setup and operation of the new Bragg setup. As shown in section 4.1.1, when two beams with a frequency difference equal to the splitting between the non-moving and moving state are used to create the optical potential for the atomic wavefunction, a transition can be driven directly between  $|0\rangle$  and either of the states  $|\pm 1\rangle$ , depending upon the direction of the two beams. To create the two beams, detuned by  $\delta\omega$ , we use the optical setup shown in figure 4.4. In this setup we derive the two beams constituting the Bragg potential from the same laser; In this case, a New Focus TLM-7000 External Cavity Diode Laser operating near the cooling transition (780.245 nm) is used. The beam is then split using a polarizing beam-splitting cube and sent through two separate Acousto-Optical Modulators (AOM). We then drive AOM1 and AOM2 at angular frequencies  $\omega_1$  and  $\omega_2$ , respectively. I will discuss how these frequencies are derived momentarily. The output beams from each AOM are then coupled into polarization maintaining fibers. One of the fibers has an inline Electro-Optical Modulator (EOM), which is used to adjust the relative phase difference between the two

beams. The beams are then output coupled from the fibers near the science cell and hit the atoms from opposite directions, resulting in the potential discussed in equation (4.6).

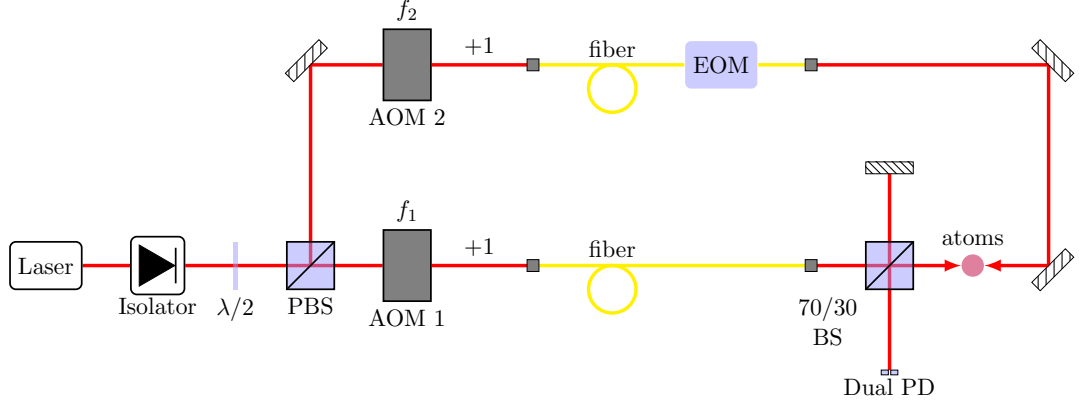


**Figure 4.4: Optical Block Diagram for Bragg Beam Setup.** The optical interferometer is used to stabilize the phase of the pulse at the beginning of each pulse. The EOM is used as an adjustable phase shifter.

Additionally, there is an optical Michelson interferometer to read out the phase difference between the two beams. This is used to actively stabilize the phase at the beginning of each pulse using the EOM phase shifter shown in one of the optical paths. This technique has been used previously for Stimulated Raman transitions [12]. A heterodyne lock was sufficient in this case because they were driving transitions between the internal states of the atoms, which are separated by energies on the order of gigahertz. However, in our case, we are operating in the Bragg regime and the splitting between the momentum states is only on the order of kilohertz. As seen from our calculations, we need to operate at pulse durations on the order of 100 microseconds, and so a heterodyne lock would not be sufficient to lock the phase of the pulse because the measurement time would take too long.

To overcome this limitation, Eun Oh has developed a different technique for reading out the phase difference. In this case, the two beams are intentionally misaligned such that there is an angle between them at the location of the photodiode. This has the effect of converting the temporal phase variation into spatial intensity variation. To illustrate this,

consider two plane waves incident on a surface with angle,  $\theta$ , between them as shown in figure 4.5. The interference pattern at the location of the photodiodes can be computed as

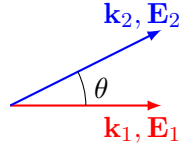


**Figure 4.5: Angle Between Bragg Beams at Photo-detector.**

follows

$$I \propto |\mathbf{E}_{\text{tot}}|^2 = \left[ \mathbf{E}_1^* e^{-i(\mathbf{k}_1 \cdot \mathbf{r} - \omega_1 t + \alpha)} + \mathbf{E}_2^* e^{-i(\mathbf{k}_2 \cdot \mathbf{r} - \omega_2 t)} \right] \cdot \left[ \mathbf{E}_1 e^{i(\mathbf{k}_1 \cdot \mathbf{r} - \omega_1 t + \alpha)} + \mathbf{E}_2 e^{i(\mathbf{k}_2 \cdot \mathbf{r} - \omega_2 t)} \right] \quad (4.23)$$

$$I \propto |\mathbf{E}_1|^2 + |\mathbf{E}_2|^2 + \mathbf{E}_1^* \cdot \mathbf{E}_2 e^{i[(\mathbf{k}_2 - \mathbf{k}_1) \cdot \mathbf{r} - (\omega_2 - \omega_1)t + \alpha]} + \mathbf{E}_1 \cdot \mathbf{E}_2^* e^{-i[(\mathbf{k}_2 - \mathbf{k}_1) \cdot \mathbf{r} - (\omega_2 - \omega_1)t + \alpha]} \quad (4.24)$$

If  $\mathbf{E}_1$  and  $\mathbf{E}_2$  are taken to be linearly polarized along  $\hat{\mathbf{z}}$  then we can simplify this to

$$I = I_0 + I_1 \cos [(\mathbf{k}_2 - \mathbf{k}_1) \cdot \mathbf{r} - (\omega_2 - \omega_1)t] \quad (4.25)$$

In this case, we take  $\mathbf{k}_1 = |\mathbf{k}_1| \hat{\mathbf{x}}$  and  $\mathbf{k}_2 = |\mathbf{k}_2| \cos(\theta) \hat{\mathbf{x}} + |\mathbf{k}_2| \sin(\theta) \hat{\mathbf{y}}$  and the photodiode to be positioned at  $x = 0$ . Therefore, the resultant interference pattern is expressed as

$$I = I_0 + I_1 \cos [|\mathbf{k}_2| \sin(\theta) y - (\omega_2 - \omega_1)t + \alpha] \quad (4.26)$$

By adjusting the angle between the beams at the photodiode such that the period of the spatial intensity pattern covers the entire photodiode, then the phase,  $\alpha$ , can be extracted by measuring the difference signal between two closely spaced photodiodes.

The frequencies used for driving the AOM's are derived from a single RF source operating at angular frequency  $\omega_{RF}$ ; however, one of the signals is modulated using an I-Q modulator to produce an RF signal at  $f'$ . Both signals are fed into a variable attenuators followed by amplifiers. The net result is approximately 1 Watt of RF power at  $\omega_{RF}$  and  $f'$

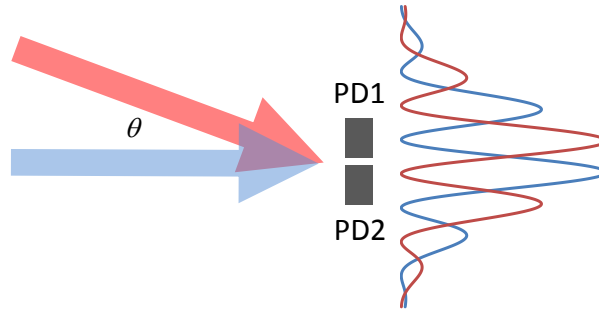


**Figure 4.6: Schematic Representation of Interference Pattern at Dual Photodiode.** As the phase shifts between the two beams, the pattern moves between the photodiodes. The difference in photodiode currents is measured and is proportional to the phase shift. The difference between the red and blue patterns is about  $180^\circ$  phase shift.

to drive the two AOM's. This is shown schematically in figure 4.7.

The basic function of the I-Q modulator is to take the low frequency inputs,  $I$  and  $Q$ , as well as the RF signal from the local oscillator,  $LO$ , and produce the output shown in equation (4.27)

$$V_{out} = I \cos(\omega_{LO}t) + Q \sin(\omega_{LO}t) \quad (4.27)$$

The multiplexer (MUX) in the circuit is used to switch the inputs  $V1$ ,  $V2$ ,  $V3$ , and  $V4$  between the outputs  $Out1$  and  $Out2$  depending upon the configuration of the digital addressing bits  $C1$  and  $C2$ . Additionally,  $V1$  and  $V2$  are driven by the same function generator with a sinusoidal voltage. The only difference is that the input to  $V2$  first passes through a phase shifter which adds a  $+90^\circ$  phase shift. The various output configurations of the multiplexer are shown in table 4.1. To implement the relative frequency shift needed to perform the asymmetric splitting operation, the sinusoidal voltage applied to  $V1$  and  $V2$  are driven at angular frequency  $\delta\omega$ , chosen to be equal to the energy splitting between  $|0\rangle$  and  $|\pm 1\rangle$ , or approximately 15 kHz. In this way, the output from the I-Q modulator for

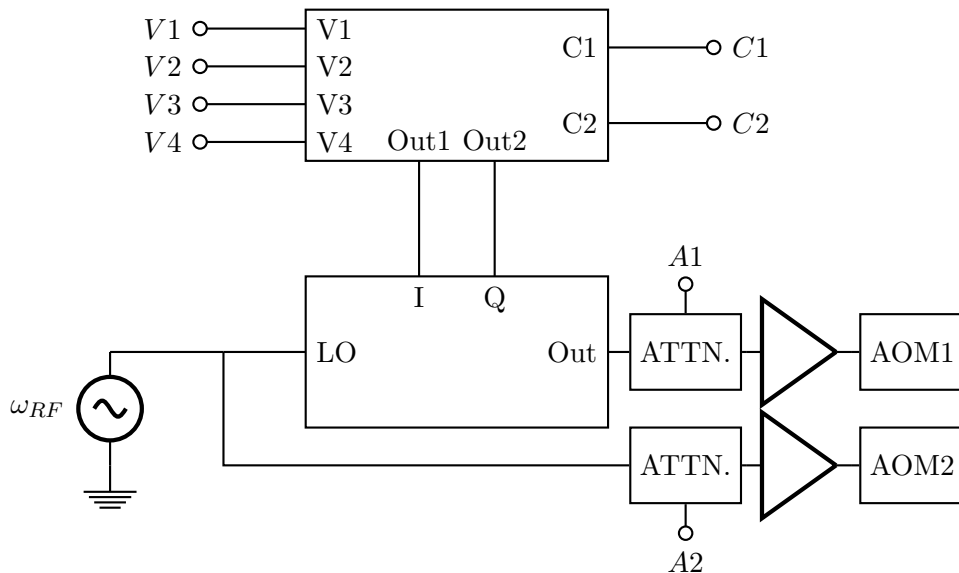


**Figure 4.7: Electronics for Driving the Bragg Beam AOMs.**

$C1$	$C2$	$Out1$	$Out2$
0	0	$V_0 \cos(\delta\omega t)$	$V_0 \sin(\delta\omega t)$
0	1	$V_0 \sin(\delta\omega t)$	$V_0 \cos(\delta\omega t)$
1	0	$V3$	$V4$
1	1	$V4$	$V3$

**Table 4.1: MUX Output Configuration.**  $C1$  and  $C2$  are the control bits of the MUX

the various control bit configurations is given in table 4.2. The resulting outputs will allow the frequency of AOM 2 to be either red or blue shifted from that of AOM 1 by  $\delta\omega$ . The phase stability of the lock was measured to be approximately 100 mrad. With this, all of the pieces are in place to perform the asymmetric splitting operation.

### 4.1.3 Results

To test the asymmetric splitting, the optics were set up as shown in figure 4.4. The polarizing beam splitter, fiber coupler, adjustable mirror and dual photodiode, were assembled together in a cage mount system and the entire system was mounted to a three-dimensional translation stage. To align the beam on the condensate, the beam was blocked before en-

$C1$	$C2$	$V_{out}$
0	0	$V_0 \cos[(\omega_{RF} - \delta\omega)t]$
0	1	$V_0 \cos[(\omega_{RF} + \delta\omega)t]$
1	0	$V3 \cos(\omega_{RF}t) + V4 \sin(\omega_{RF}t)$
1	1	$V4 \cos(\omega_{RF}t) + V3 \sin(\omega_{RF}t)$

**Table 4.2: I-Q Modulator Outputs.**  $C1$  and  $C2$  are the control bits of the MUX

tering the EOM fiber. Therefore only the beam from the other fiber was present in the science cell. The laser was shifted close to resonance ( $\lambda = 780.240$  nm), such that atoms would scatter the photons and therefore the number of atoms seen by absorption imaging would be decreased. The number of atoms remaining after a long ( $\approx 0.5$  seconds) pulse of the single Bragg beam was measured as a function of the translation stage position. The resulting atom loss gave a good measure for the center of the cloud of atoms. Additionally, this gave a measure of the peak scattering rate, from which an estimate of intensity and thus  $\beta$  for this single beam can be obtained.

Upon getting the beam lined up on the atomic cloud, the other beam was then unblocked and two mirrors are used to walk the beams on top of one another. This was most readily achieved by monitoring the power coupling of the second beam into the fiber for the first beam. Upon doing this we attempted to split the atoms.

The condensate was loaded into a fairly weak trap  $\omega_x = \omega_y = 2\pi \times 2$  Hz and  $\omega_z = 2\pi \times 7$  Hz and the splitting pulse was applied. After applying the pulse, the atoms were allowed to evolve in the trap for approximately 50 ms before being dropped for 5 ms and imaged via absorption imaging. By doing this, the different momentum states had time to separate and could be readily distinguished. We adjusted the pulse duration and measured the number of atoms in states  $|0\rangle$ ,  $|1\rangle$ , and  $|-1\rangle$ . When the frequency of AOM 2 was shifted blue of AOM 1 by  $\delta\omega \approx +15$  kHz, the atoms were kicked in the direction of the beam coming from AOM 2. On the contrary, when the frequency of AOM 2 was shifted red of AOM 1 by  $\delta\omega = -15$  kHz, the atoms were kicked in the direction of the beam coming

from AOM 1. This is exactly what one would expect from the theory.

Additionally, the fractional populations were mapped out for varying pulse durations. The images typically seen were like those in Figure 4.8. Data was taken with many samples

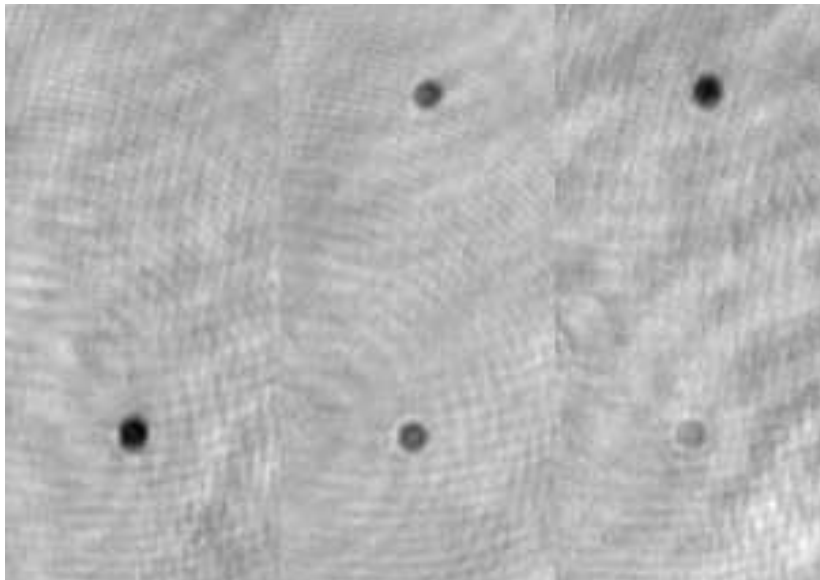


**Figure 4.8: Atoms After Various Split Pulse Durations.** This figure shows three cases, [Left] no pulse, [Middle] a  $\pi/2$ -pulse and [Right] a  $\pi$ -pulse. The top cloud in the picture is the packet moving with  $+2\hbar k$  and the bottom cloud is stationary.

at varying times and the results were plotted. The fractional number of atoms in each packet are plotted versus the split pulse duration in Figure 4.9. The population very clearly Rabi oscillates between the states  $|0\rangle$  and  $|1\rangle$ . The fact that the oscillations do not have an amplitude of 100% is likely due to the atoms having an initial velocity. This comes directly from the fact that the initial velocity acts as a detuning,  $\Delta \equiv 4\hbar\omega_R(2n + 1 + \kappa/k) - \delta\omega$ . In any case, it is clear that the atoms can be coherently transferred between the states.

## 4.2 Ramsey Interferometer

As a first attempt at making an interferometer, we consider a Ramsey type interferometer [51]. Ramsey introduced the separated oscillatory fields interferometer to study the internal

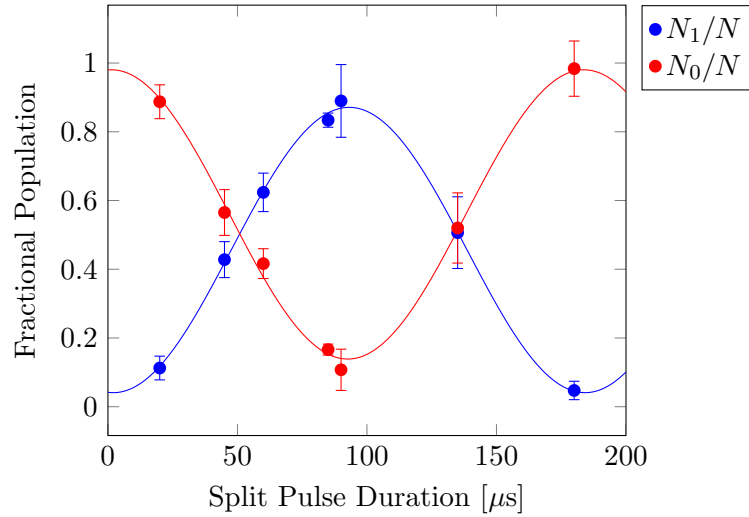


**Figure 4.9: Momentum State Populations versus Splitting Time.** The atoms oscillate between the moving and stationary states.

states transition; however, we keep our atoms in the same internal state. A typical Ramsey interferometer is characterized by taking the atoms in one state, applying a  $\pi/2$ -pulse to transfer the atoms into a superposition state, then allowing the atoms to freely-evolve in a non-interaction region followed by the application of a second  $\pi/2$ -pulse to read-out the developed phase. This phase shift comes from the difference in energies between the two states in the system. A schematic representation of this is shown in figure 4.10.

It is worth noting that for our experiment the difference in energies between the two states comes from the difference in their kinetic energy. The diagram in figure 4.10 is exaggerated to show that if enough time is placed between the two  $\pi/2$ -pulses, then the atomic wave-packets will separate. I will return to this thought a bit later as it is quite relevant to our results. For now, I will develop the theory assuming that the separation of the wavepackets is small compared to their extent.

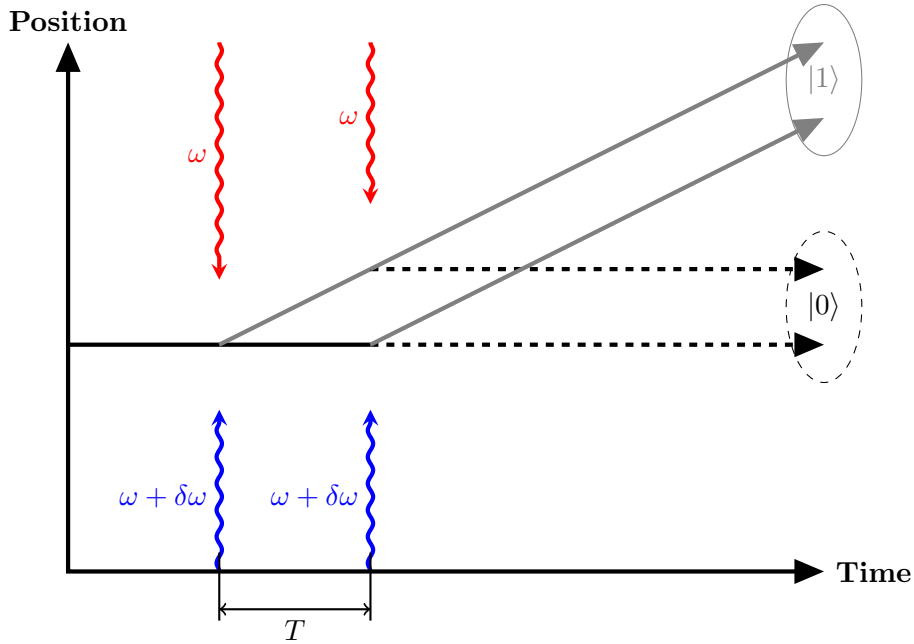


**Figure 4.10: Schematic Representation of a Ramsey Interferometer.** The basic implementation is two  $\pi/2$  splitting pulses separated by some time  $T$ .

### 4.2.1 Theory

We begin by assuming that the atoms start with nearly zero initial velocity  $|\Psi_0\rangle = |0\rangle$  and by neglecting the effects of the confining potential, which should be valid near the center of the trap. The atoms are then split into an even superposition using a  $\pi/2$ -pulse of the splitting light, i.e.  $\beta t_s = \pi/2$ . We can calculate the resulting wavefunction after the split using equation 4.21.

$$|\Psi_0\rangle \rightarrow \frac{1}{\sqrt{2}} \left[ |0\rangle - ie^{i\phi_{s1}} |1\rangle \right] \quad (4.28)$$

where  $\phi_{s1}$  is the phase written onto the atomic wavefunction by the laser. The atoms are then allowed to free evolve for time  $T$ . We can use the same propagator with  $|\Omega| = 0$ . So after free evolution, the wavefunction is given by

$$|\Psi_{fe}\rangle = \frac{1}{\sqrt{2}} \left[ |0\rangle - ie^{i(\phi_{s1}-\Delta T)}|1\rangle \right] \quad (4.29)$$

When the recombination  $\pi/2$ -pulse is applied, the transitions shown below will be driven.

$$\begin{aligned} |0\rangle &\rightarrow \frac{1}{\sqrt{2}} \left[ |0\rangle - ie^{i\phi_{s2}}|1\rangle \right] \\ |1\rangle &\rightarrow \frac{1}{\sqrt{2}} \left[ -ie^{-i\phi_{s2}}|0\rangle + |1\rangle \right] \end{aligned} \quad (4.30)$$

This leads to the final wavefunction:

$$|\Psi_f\rangle = \frac{1}{2} \left[ \left(1 - e^{-i\phi}\right) |0\rangle - ie^{i(\phi_{s1}-\Delta T)} \left(1 + e^{-i\phi}\right) |1\rangle \right] \quad (4.31)$$

where  $\phi \equiv \Delta T + \phi_{s2} - \phi_{s1}$  for simplification. From this we can compute the probability that the atoms will either be in the moving or non-moving states. This corresponds to the measurable quantity of the fractional populations in each state.

$$\frac{N_0}{N} = P_0 = |\langle \Psi_f | 0 \rangle|^2 = \frac{1}{4} \left(1 - e^{-i\phi}\right) \left(1 - e^{i\phi}\right) = \sin^2\left(\frac{\phi}{2}\right) \quad (4.32)$$

$$\frac{N_1}{N} = P_1 = |\langle \Psi_f | 1 \rangle|^2 = \frac{1}{4} \left(1 + e^{-i\phi}\right) \left(1 + e^{i\phi}\right) = \cos^2\left(\frac{\phi}{2}\right) \quad (4.33)$$

First, let's consider the case that the laser is allowed to evolve freely between the two  $\pi/2$ -pulses. In this case the atomic phase and the laser phase should still remain in sync throughout the interferometer, which leads to  $\phi_{s2} = \phi_{s1} = 0$ . In the case that the detuning,  $\Delta$ , is zero, all of the atoms will be transferred to the moving state. If however there is a small detuning, then the interferometer phase does depend on time. So measuring the fraction of atoms that returns to rest will oscillate at the beat frequency between the lasers and the atomic level splitting. This calculation is a little oversimplified in this case. There is also an offset phase that gets added in due to the detuning if a full calculation is performed.

The other case we consider is when the laser phase is not allowed to evolve freely

between the two  $\pi/2$ -pulses. If instead the laser phase is reset to its initial value, i.e.  $\phi_{s2} = -\delta\omega(T + t_s)$ , where  $t_s$  is the duration of the split pulse. In this case, the phase becomes time dependent. Specifically, if the fraction of atoms returning to rest is measured versus the free evolution time, then the output should oscillate at the energy splitting between the moving and non-moving states.

$$\frac{N_0}{N} = \frac{1}{2} \left[ 1 - \cos \left( \frac{(E_1 - E_0)}{\hbar} T - \delta\omega t_s \right) \right] \quad (4.34)$$

We know that the energy splitting is proportional to the recoil frequency,  $E_1 - E_0 = 4\hbar\omega_R(1 + \kappa/k)$ . Therefore, the fraction of atoms returning to rest will oscillate at four times the recoil frequency. This corresponds to a period of approximately  $67\mu\text{s}$ . It is also worth noting that this measurement is sensitive to the initial velocity of the atoms and effort must be made to reduce that effect as much as possible. Specifically, any velocity noise will create phase noise in the interferometer output.

### 4.2.2 Results

In order to actually measure an interference curve, the Bragg beams were set up along the Y-axis of the guide, where optical access is readily available. The atoms were loaded into the waveguide in a fairly weak potential, i.e.  $\omega_x = \omega_y = 2\pi(2 \text{ Hz})$  and  $\omega_z = 2\pi(7 \text{ Hz})$ .

To minimize the effects of the initial velocity, the oscillatory motion of the atoms was measured. From these measurements the time could be adjusted between the trap loading sequence and the interferometry pulse sequence. The time was set such that the interferometer began while the atoms were at the turning point in their oscillation, i.e.  $\kappa \propto v \approx 0$ .

The total interferometer time,  $T$ , was adjusted by small amounts and the fraction of atoms returning to rest was measured in order to measure the oscillation period. This was performed at several nominal times and some of the results can be seen in figure 4.11.

We fit the data to a cosine function and the fitting parameters are shown in table 4.3.

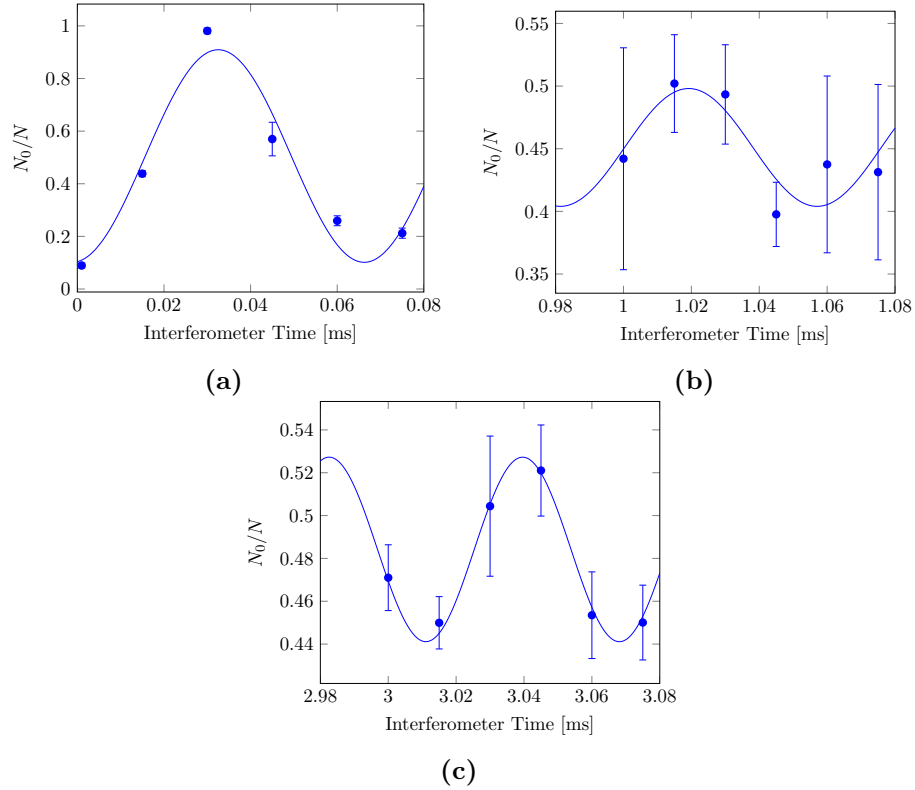


**Figure 4.11: Ramsey Interference Curves.** The fractional population of the atoms returning to rest at the end of the interferometer sequence versus the total interferometer time for three nominal times (a) 0ms, (b) 1 ms and (c) 3 ms. Each point shows the average of three runs at a given interferometer time, with the error bars representing the standard deviation of those measurements. Each set of data took approximately 45 minutes to record.

The fitting function used is defined as:

$$\frac{N_0}{N} = y_0 + A \cos \left[ \left( \frac{2\pi}{T} \right) (t - t_0) \right] \quad (4.35)$$

Parameter	0 [ms]	0.25 [ms]	1 [ms]
$y_0$	$0.505 \pm 0.05$	$0.69 \pm 0.02$	$0.45 \pm 0.01$
$A$	$0.40 \pm 0.07$	$0.19 \pm 0.03$	$0.047 \pm 0.036$
$t_0[\mu\text{s}]$	$0.033 \pm 0.002$	$0.04 \pm 0.01$	$-0.04 \pm 0.18$
$T[\mu\text{s}]$	$0.067 \pm 0.006$	$0.063 \pm 0.003$	$0.076 \pm 0.012$

Parameter	2 [ms]	3 [ms]
$y_0$	$0.45 \pm 0.02$	$0.484 \pm 0.002$
$A$	$0.04 \pm 0.03$	$0.04 \pm 0.03$
$t_0[\mu\text{s}]$	0.055	$0.65 \pm 0.05$
$T[\mu\text{s}]$	$0.0662 \pm 0.00003$	$0.057 \pm 0.001$

**Table 4.3: Ramsey Interference Curve Fitting Parameters.** This table shows the fitting parameters for the 5 nominal, total Ramsey interferometers that we implemented. The fitting function is shown in equation 4.35

From these fitting parameters, we can immediately see that the period of oscillation is very near the expected value of  $66 \mu\text{s}$ . In fact, the average value for the period is  $65.7 \pm 3.1 \mu\text{s}$ . This yields a measurement with 3% error and only 1.4% away from the expected value. While this gives a nice demonstration of interference, this result can be improved upon by employing the power of the interferometer as discussed in 4.4. From the fitting parameter data, we can also calculate the visibility of the interferometer and examine the limitations of the interferometer. The visibility is usually defined as in equation 4.36 [52].

$$V = \frac{\max - \min}{\max + \min} \quad (4.36)$$

In terms of our fitting parameters from equation 4.35 this is  $V = A/y_0$ .

At some point, the data becomes quite noisy and the fitting will no longer work. However, there is still some underlying visibility. We usually refer to this as contrast. We can

obtain a measure of the contrast by considering the expected value and the variance of  $N_0/N$  for an interferometer with uniform phase noise,  $f(\phi)$ , ranging from 0 to  $2\pi$  as shown in equation 4.37.

$$f(\phi) = \begin{cases} \frac{1}{2\pi} & 0 \leq \phi \leq 2\pi \\ 0 & \text{otherwise} \end{cases} \quad (4.37)$$

The interferometer output is expected to be  $N_0/N = (1/2)(1 + V \cos(\phi))$ , where  $V$  is the underlying visibility. Therefore the expectation value of  $N_0/N$  and of  $(N_0/N)^2$  will be given by equations 4.38 and 4.39, respectively.

$$E\left(\frac{N_0}{N}\right) = \int_0^{2\pi} \frac{1 + V \cos(\phi)}{2} d\phi = \frac{1}{2} \quad (4.38)$$

$$E\left(\left(\frac{N_0}{N}\right)^2\right) = \int_0^{2\pi} \frac{[1 + V \cos(\phi)]^2}{4} d\phi = \frac{1}{8\pi}(2\pi + V^2\pi) \quad (4.39)$$

Therefore the variance in  $N_0/N$  is directly related to the contrast as shown in equation 4.40.

$$\Delta \equiv V \left(\frac{N_0}{N}\right) = \sqrt{E\left(\left(\frac{N_0}{N}\right)^2\right) - E\left(\frac{N_0}{N}\right)^2} = \frac{V}{\sqrt{8}} \quad (4.40)$$

To understand the expected behavior for the directly measured visibility we must consider the initial velocity noise. As mentioned previously, the phase for our Ramsey interferometer depends on the initial velocity since  $\phi = 4\omega_R T (1 + \kappa/k)$ , where  $T$  is again the total time of the interferometer. If we assume that the initial velocity has a Gaussian distribution,  $f(\kappa)$ , centered around  $\kappa = 0$  as shown in equation 4.41.

$$f(\kappa) = \frac{1}{\sqrt{2\pi}\delta\kappa} e^{-\kappa^2/(2\delta\kappa^2)} \quad (4.41)$$

The expectation value of  $N_0/N$  can be calculated in this case to be:

$$E \left( \frac{N_0}{N} \right) = \int_{-\infty}^{\infty} \frac{1}{2} \left( 1 + V \cos \left[ 4\omega_R T \left( 1 + \frac{\kappa}{k} \right) \right] \right) f(\kappa) d\kappa = \frac{1}{2} + \frac{V_0}{2} \cos(4\omega_R T) e^{-32\omega_R^2 \delta\kappa^2 T^2 / k^2} \quad (4.42)$$

From this expression, we see that the measured visibility will vary as a function of time as shown below.

$$V(T) = V_0 e^{-8\omega_R^2 \delta\kappa^2 T^2 / k^2} \quad (4.43)$$

here  $V_0$  is the measured visibility at  $T = 0$ .

We would also like to understand what limits the underlying visibility. In this case we must take into consideration the finite extent of the atomic wavefunctions,  $\Psi_1$  and  $\Psi_2$ . Upon recombination, we expect that the interference will depend upon how well overlapped the two packets are. Mathematically, this is represented as the overlap integral shown in equation 4.44.

$$V = \int \Psi_1 \Psi_2 d^3 \mathbf{r} \quad (4.44)$$

To find the atomic wavefunction of a Bose-Einstein Condensate, one must turn to the non-linear Schrödinger equation known as the Gross-Pitaevskii Equation (GPE). I will spare the details here [53]; however, the solution becomes quite simple in the case that the kinetic energy is negligible, the Thomas-Fermi limit. In this case, the wavefunction is given by:

$$\Psi_{TF} = \sqrt{\frac{\mu - V(\mathbf{r})}{g}} \quad (4.45)$$

where  $g = 4\pi\hbar^2 a/m$  is the self-interaction,  $a = 5.77$  nm is the scattering length and  $\mu$  is the chemical potential. In our experiment the potential is harmonic and so the wavefunction can be written in terms of the Thomas-Fermi lengths in each direction,  $L_x$ ,  $L_y$ , and  $L_z$ .

$$\Psi_{TF} = \sqrt{n_0 \left[ 1 - \left( \frac{x}{L_x} \right)^2 - \left( \frac{y}{L_y} \right)^2 - \left( \frac{z}{L_z} \right)^2 \right]} \quad (4.46)$$

When the Bragg splitting pulse is applied at  $T = 0$ , one of the wavepackets begins moving along the direction of the Bragg beam (we're splitting along  $y$ ) with  $v = 2v_R \approx 12$  mm/s. This time dependence was included into one of the wavefunctions and the overlap integral was computed numerically. This numeric result was then used to fit the contrast data. Since the lengths are related via the trapping frequencies, there were only two free parameters in the fit. One of lengths and an overall multiplier. We obtain the results plotted in figure 4.12.

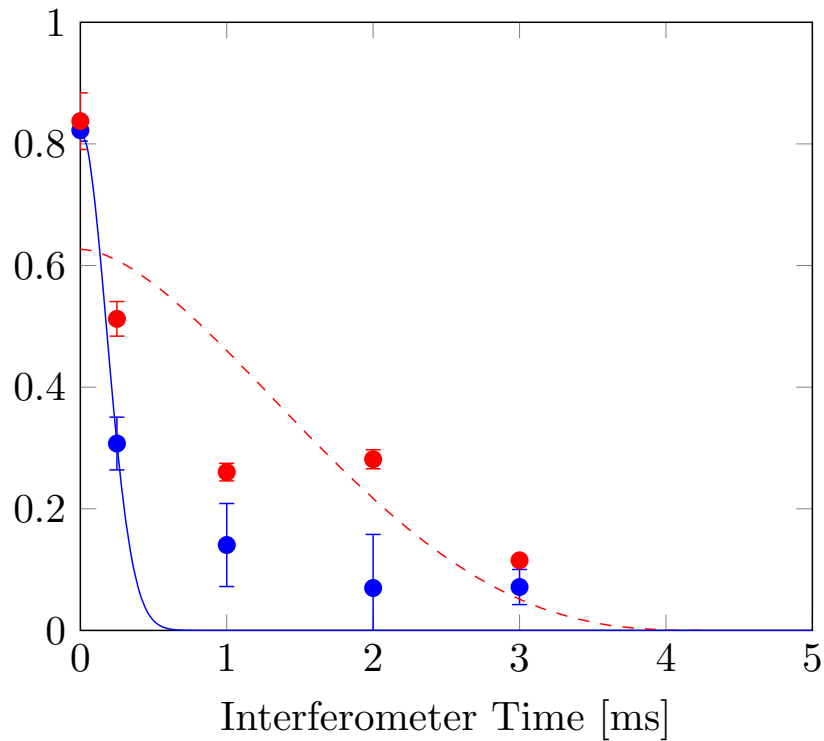


**Figure 4.12: Ramsey Interferometer Visibility versus Interferometer Time.** The visibility (blue) and the contrast (blue) are presented along with their respective fitting functions.

The visibility clearly drops off quite quickly, taking only about 300 microseconds to

drop off; however, the contrast remains good for several milliseconds. The results from the fit using the Thomas-Fermi wavefunctions show that it takes approximately 4 ms for the wavepackets to completely separate and that the extent of the wavepacket is approximately  $32 \mu\text{m}$ . This later number is consistent with the size that we get from fitting the absorption images of the cloud.

Additionally, we can obtain a measure of the initial velocity noise from the fit of the actual visibility using equation 4.43. This gives velocity noise of  $\delta\kappa/k = \delta v/v_R \approx 0.02$ . So the initial velocity fluctuates by about  $240 \mu\text{m/s}$ . This is consistent with the measurements that we obtain by measuring the oscillations of the atoms in the trap.

### 4.3 Ramsey-Bordé Interferometer

As a second type of interferometer, we implemented a Ramsey-Bordé configuration. This is essentially a variant of the Ramsey interferometer, but with the addition of one or more  $\pi$ -pulses between the two  $\pi/2$ -pulses as shown in figure 4.13. The effect of these additional pulses is to increase the total coherence time by creating a quantum revival effect. This can be thought of most simply as allowing the atomic wavepackets to return to the same position at the end of the interferometer, ensuring good overlap of the wavepackets. Additionally, because of the symmetry of the interferometer, the initial velocity of the atoms no longer impacts the phase. In our interferometer, the  $\pi$ -pulses are reflect pulses. That is to say, they drive  $|1\rangle \leftrightarrow |-1\rangle$ . The basic schematic of such an interferometer is shown in figure 4.13. While the quantum revival effect can be achieved with only one reflect pulse, there are other limitations to the interferometer performance. Since the interferometry is performed with the atoms in a harmonic trapping potential, phase gradients can develop between the two packets. This can cause issues with the readout. As such we chose to use a two sided interferometer which should minimize these phase gradients [54]. As a second type of interferometer, we implemented a Ramsey-Bordé configuration. This is essentially a variant

of the Ramsey interferometer, but with the addition of one or more  $\pi$ -pulses between the two  $\pi/2$ -pulses as shown in figure 4.13. The effect of these additional pulses is to increase the total coherence time by creating a quantum revival effect. This can be thought of most simply as allowing the atomic wavepackets to return to the same position at the end of the interferometer, ensuring good overlap of the wavepackets. Additionally, because of the symmetry of the interferometer, the initial velocity of the atoms no longer impacts the phase. In our interferometer, the  $\pi$ -pulses are reflect pulses. That is to say, they drive  $|1\rangle \leftrightarrow |-1\rangle$ . The basic schematic of such an interferometer is shown in figure 4.13. While the quantum revival effect can be achieved with only one reflect pulse, there are other limitations to the interferometer performance. Since the interferometry is performed with the atoms in a harmonic trapping potential, phase gradients can develop between the two packets. This can cause issues with the readout. As such we chose to use a two sided interferometer which should minimize these phase gradients [54].

### 4.3.1 Theory

In order to implement this interferometer configuration, we need the ability to reflect the atoms, i.e. drive the transition  $|+1\rangle \leftrightarrow |-1\rangle$ . This was looked at previously in our group by Hughes et. al. [49]. It was found that in order to achieve a high fidelity reflect operation a single pulse (with both beams operated at  $\omega$ ) can be used. This should yield an efficiency of approximately 90%. This requires an intensity which gives  $\beta \approx 4.5\omega_R$ . This is substantially higher than the optimal value for the asymmetric splitting/recombination pulse of  $\beta \approx \omega_R$  and therefore necessitates the ability to have a large dynamic range on the phase locking circuit. Unfortunately, the circuit only acceptably maintains the phase for a very narrow dynamic range, thereby acting as a technical limitation. There are several means by which this obstacle can be circumvented. One possible solution would have been to adjust the gain of the feedback loop between the two pulses. Another solution was to use a different type of reflect pulse which reduces the sensitivity to intensity. We have shown the ability

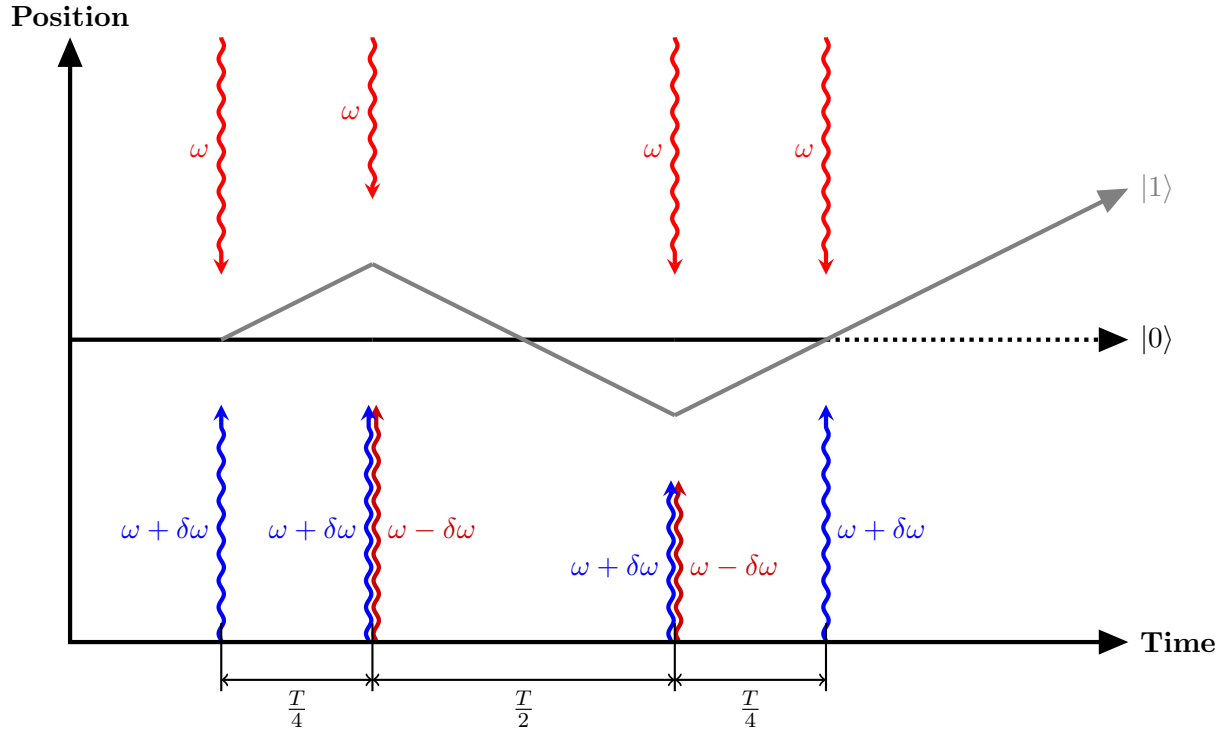


**Figure 4.13: Schematic of Ramsey-Bordé Interferometer.**

to shift one of the Bragg beams either red or blue of the other by  $\delta\omega$ . We now consider the case that we do both at the same time, which leads to the energy-momentum diagram shown in figure 4.14.

In this case, the electric field which impinges upon the atoms would be given by

$$\mathbf{E}_{tot} = \frac{\mathbf{E}_1}{2} \left[ e^{i(kz - \omega t - \delta\omega t)} + e^{i(kz - \omega t + \delta\omega t)} \right] e^{i\alpha} + \mathbf{E}_2 e^{i(-kz + \omega t)} \quad (4.47)$$

The intensity is therefore given by

$$I \propto |\mathbf{E}_{tot}|^2 = |\mathbf{E}_1|^2 \cos^2(\delta\omega t) + |\mathbf{E}_2|^2 + \mathbf{E}_1^* \cdot \mathbf{E}_2 e^{-i(2kz + \alpha)} \cos(\delta\omega t) + \mathbf{E}_2^* \cdot \mathbf{E}_1 e^{i(2kz + \alpha)} \cos(\delta\omega t) \quad (4.48)$$

If  $\mathbf{E}_1$  and  $\mathbf{E}_2$  are the same polarization, then  $\mathbf{E}_2^* \cdot \mathbf{E}_1 = \mathbf{E}_1^* \cdot \mathbf{E}_2 = |\mathbf{E}_1||\mathbf{E}_2|$  and the potential

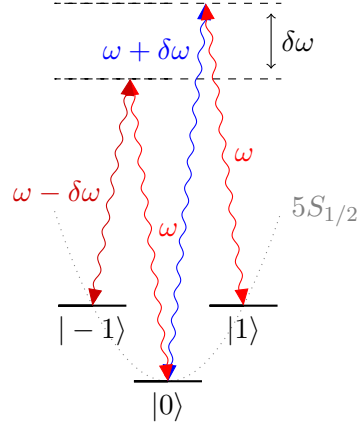


**Figure 4.14: Energy-momentum Diagram for Reflect Pulse.**

due to the AC Stark shift can be written as

$$V_{AC} = \hbar\beta_1 \cos^2(\delta\omega t) + \hbar\beta_2 \cos(2kz + \alpha) \cos(\delta\omega t) \quad (4.49)$$

or after a bit of algebra in the form that is most useful for the Bragg operations

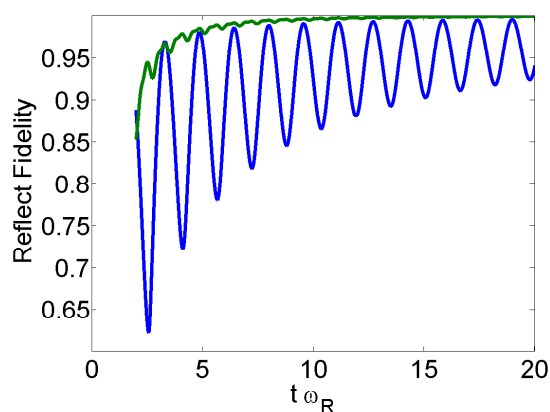
$$V_{AC} = \hbar\beta_1 \cos^2(\delta\omega t) + \frac{\hbar\beta_2}{2} [\cos(2kz + \alpha + \delta\omega t) + \cos(2kz + \alpha - \delta\omega t)] \quad (4.50)$$

The first term can be dropped as it has no effect since it applies all of the states and results in an overall phase. We can now plug this into Schrödinger's equation and use the Bloch expansion as before. I will skip the details here and simply state the end result. Again, there is an infinite set of coupled differential equations relating the coefficients  $c_n(t)$  just as for the splitting derivation with the characteristic equation (4.51).

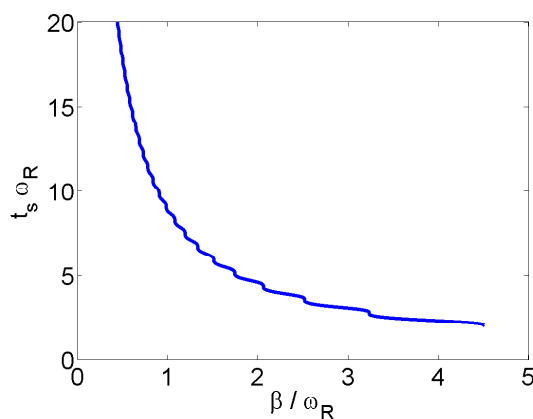
$$i\hbar\dot{c}_n = \hbar\omega_R(2n + \kappa/k)^2 c_n + \frac{\hbar\beta}{2} \cos(\delta\omega t) [e^{i\alpha} c_{n-1} + e^{-i\alpha} c_{n+1}] \quad (4.51)$$

In this case, MATLAB was used to reach a numerical solution to this system of equations. Just as with the asymmetric splitting, the system of equations was truncated at a reasonable level. The population in the various states was plotted versus  $\beta$  and the pulse duration and

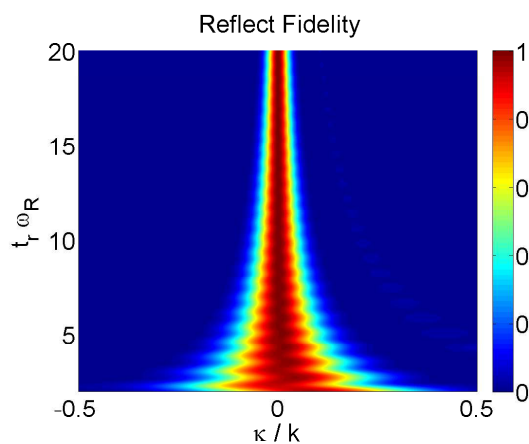
was used to determine the number of states required to maintain accuracy. The value of  $\beta$  was optimized for each pulse duration and then the fidelity was plotted versus the initial velocity to show the initial velocity dependence, i.e. versus  $\kappa$ . From these plots, it is clear that the reflect is much more sensitive to initial velocity than the splitting operations. The results of these calculations are shown in figure 4.15.



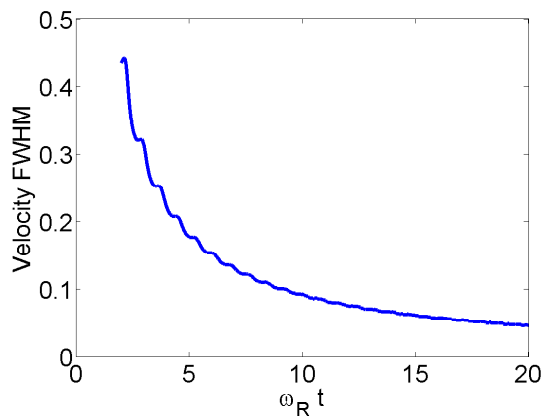
(a) **Pulse Duration Dependence of Optimal Reflect Fidelity.** Shows comparison between the single color (blue) and multicolor reflect fidelity (green).



(b) **Intensity Dependence of Optimal Pulse Duration.**



(c) **Intensity and Initial Velocity Dependence of Fidelity.**



(d) **FWHM Velocity width of Fidelity versus pulse duration.** FWHM is normalized to the recoil velocity,  $v_R$ .

**Figure 4.15: Reflect Pulse Numerical Calculation Results**

Additionally, the phase developed during the interferometer will be different for the Ramsey-Bordé configuration. To simplify the calculation we can state that the output of the interferometer depends only on the phase difference between the two paths of the interferometer. In other words, we can write

$$\frac{N_1}{N} = \frac{1}{2}[1 - \cos(\phi_p + \phi_1 - \phi_0)] \quad (4.52)$$

where  $\phi_1$  is the phase developed by the atoms which are nominally moving,  $\phi_0$  is the phase developed by the atoms which are nominally at rest and  $\phi_p$  is a phase shift from the pulses. In this case, we can use the path integral formulation to define the phases developed and simplify our calculation. The phases are thus a function of the action,  $S$ , as shown in equation (4.53) [10].

$$\phi = \frac{1}{\hbar}S = \frac{1}{\hbar} \int_P \mathcal{L} dt \quad (4.53)$$

If the experiment is performed in a very weakly confining trap and at times short compared to the oscillation period, then the potential energy term may be neglected and the integral becomes quite simple. The resulting phases will be given by

$$\begin{aligned} \phi_1 &= \frac{1}{\hbar} \int_{P_1} E dt = (E_1 + E_{-1}) \frac{T}{2} = \hbar\omega_R \left[ \left(2 + \frac{\kappa}{k}\right)^2 + \left(-2 + \frac{\kappa}{k}\right)^2 \right] \frac{T}{2} = \omega_R T \left(4 + \frac{\kappa^2}{k^2}\right) \\ \phi_0 &= \frac{1}{\hbar} \int_{P_0} E dt = E_0 T = \frac{\kappa^2}{k^2} T \end{aligned} \quad (4.54)$$

Perhaps not so surprisingly, the end result is nearly the same as the case of the Ramsey interferometer, but with one major and important difference. In this case, the interferometer phase does not depend on the initial velocity of the atoms, only the number of atoms remaining depends on this quantity. Therefore, even if the initial velocity fluctuates, it

should not produce phase noise. Additionally, we once again have a means of measuring the recoil frequency. The fraction of atoms returning to rest after the recombination pulse will be given by equation (4.55).

$$\frac{N_0}{N} = \frac{1}{2}[1 - \cos(\phi_p + 4\omega_R T)] \quad (4.55)$$

### 4.3.2 Implementation

To implement this new reflect, modifications to the AOM drive circuitry were required. Fortunately these modifications were quite simple due to the multiplexer. By connecting the inputs of the multiplexer  $V3$  to ground and  $V4$  to the same sinusoidal voltage used for  $V1$  in figure 4.7, we were able to produce both the asymmetric splitting and reflect pulses by simply changing the address bit configuration during the experiment. It is worth noting that with these modifications, the various output configurations are as shown in table 4.4.

$C1$	$C2$	$V_{out}$
0	0	$V_0 \cos[(\omega_{RF} - \delta\omega)t]$
0	1	$V_0 \cos[(\omega_{RF} + \delta\omega)t]$
1	0	$(V_0/2)\{\cos[(\omega_{RF} + \delta\omega)t] + \cos[(\omega_{RF} - \delta\omega)t]\}$
1	1	$(V_0/2)\{\sin[(\omega_{RF} + \delta\omega)t] + \sin[(\omega_{RF} - \delta\omega)t]\}$

**Table 4.4: I-Q Modulator Outputs.** Outputs to modulated AOM shown in figure 4.7.  $C1$  and  $C2$  are the control bit inputs of the MUX.

One of the major difficulties in getting this experiment to work at all came from the velocity sensitivity of the reflect operation. As can be seen clearly in the plot of the fidelity of the reflect operation versus intensity parameter,  $\beta$ , and initial velocity parameter,  $\kappa$ , the lower the light intensity the more velocity sensitive the reflect becomes since the pulse needs to be longer. There is a clear tradeoff between keeping the number of atoms remaining in the interferometer high and how sensitive the pulse sequence is to the atomic velocities.

Under our operating conditions,  $\beta \approx \omega_R$ , and the velocity width was  $\delta v \approx 0.01v_R$ . This means that the initial velocity of the cloud of atoms must be below this level to maintain any appreciable number of atoms at the end of the interferometer pulse sequence.

The atomic oscillations were reduced in the same fashion as in the Ramsey interferometer experiment. An oscillation curve was measured and an appropriate delay was inserted to allow the atoms to reach their turning point before the interferometer pulse sequence began.

### 4.3.3 Results

In the Ramsey-Bordé interferometer configuration, we were able to extend the coherence time out to over 4 ms. Additionally, data was taken for longer interferometer times, but the visibility was quite low. The drop in visibility is likely due to initial velocity fluctuations from loading the atoms into the trap. We predict a peak fidelity around 80% for the velocity noise we observed. It is also worth noting that the velocity noise will cause number noise from shot to shot and therefore the data exhibits more noise than the Ramsey data at short total interferometer times.

For this configuration, the visibility will drop off due to the reflect pulses velocity dependence. Since the atoms are being trapped inside a harmonic potential, as the atoms move away from the trap center they will lose kinetic energy. After approximately 10 ms of time, the atoms will be slowed enough by the potential to cause the reflect pulse to stop working. This comes from the fact that the reflect pulse is so narrow in velocity acceptance as shown in figure [4.15a](#).

## 4.4 Recoil Frequency Measurements

While the recoil frequency measurements produced by the two interferometers show that we have in fact observed interference, these results are not very exciting. However, we have not really tapped into the power of the interferometer at this point. By extending the

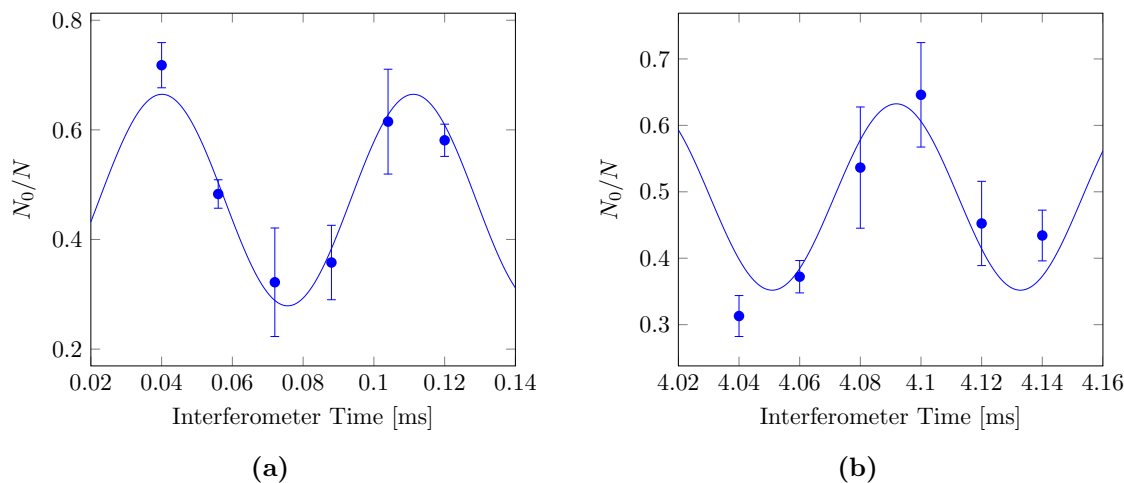


**Figure 4.16: Ramsey-Bordé Interference Curves.** 4.16a shows the results from the 0-0-0 ms interferometer and 4.16b shows the results of the 1-2-1 ms interferometer.

Parameter	0-0-0 [ms]	1-2-1 [ms]
$y_0$	$0.47 \pm 0.02$	$0.49 \pm 0.03$
$A$	$0.19 \pm 0.03$	$0.14 \pm 0.04$
$t_0$	$0.040 \pm 0.004$	$-0.001 \pm 0.004$
$T$	$0.071 \pm 0.006$	$0.082 \pm 0.012$

**Table 4.5: Ramsey-Bordé Interference Curve Fitting Parameters.** The fitting function is described in equation 4.35.

interferometer time, we are able to observe many fringes of the interference pattern. By using all of the data together from the Ramsey experiment we should be able to produce a much better measurement of the recoil frequency. In fact, by taking the data for the 0, 1, and 3 ms runs of the Ramsey experiment together and allowing only the value of  $y_0$  and  $A$  to vary, we measure a period of oscillation in the interference pattern of  $T = 66.6 \pm 0.7 \mu\text{s}$ . This is within error of the expected value of  $66.3 \mu\text{s}$ . One would expect that the longer time data would provide the best value for this measurement; however, due to the uncertainty in determining the fringe number that we are on from the data. The best individual data from the Ramsey experiment is the 1 ms run. This yields a result of  $T = 65.7 \pm 0.8 \mu\text{s}$  which is also within error of the expected value.

Again, one would expect the Ramsey-Bordé data to provide even better precision due to

the increased total interferometer time. In fact, by using both sets of Ramsey-Bordé data together and fitting to a sinusoidal function we obtain a measurement of  $T = 66.3 \pm 0.11$   $\mu\text{s}$ .

While this measurement proves our ability to make a useful interferometer, it is far from being competitive with other techniques at this point in time. Other groups are able to achieve measurement precisions on the order of  $\sigma_T/T = 10^{-9}$  [55, 56, 57]. It is worth pointing out that the measurement of the recoil frequency, when combined with other measurements, allows for the determination of the fine-structure constant and therefore improved measurements can provide a test for theory. We expect that the total interferometer time can be increased out to those of our other apparatus of around 100 ms. Even so, this would not be competitive with the other aforementioned experiments. Furthermore, since we are implementing this interferometer in a confining potential, as the interferometer time is increased a large systematic error in the phase arises from that confinement. Therefore, a free-space interferometer is much better suited for recoil measurements.

## 4.5 Conclusions

We have shown our ability to manipulate the atoms asymmetrically and obtained some reasonable accuracy in our proof of principle measurements of the recoil frequency considering. Additionally, we have developed a new type of reflect pulse which reduces the sensitivity to the intensity of the laser beams used in the Bragg grating.



# 5 | CONCLUSIONS

The main goal of this dissertation was to design and implement a magnetic trap for Bose-Einstein condensed atoms in a second apparatus for our lab to perform atom interferometry experiments in. This new apparatus has been designed specifically to overcome the shortcomings of the gravimetry and gyroscope experiments previously performed in the lab. With this new trap and the demonstration of the asymmetric splitting and recombination operations, more advanced versions of these previous experiments can now be performed.

## 5.0.1 Future Directions

### Improved Sagnac Interferometer

With the development of a new apparatus with a cylindrically symmetric trapping potential, it is now possible to implement an area enclosed interferometer which is optimized for rotation sensing. The principle of this future experiment was first proposed by Horikoshi et al. [58]. The basic principle of operation would be to start with the atoms at rest in the center of the cylindrically symmetric trapping potential. We will then use Bragg operations to split the atoms along the x direction, thereby obtaining two packets of atoms moving in opposing directions along x. The atoms will be slowed by the harmonic potential and eventually reach their turning point and momentarily come to rest. At this point, we will then split both packets of atoms along the y-direction using an identical Bragg pulse. This will result in four total packets of atoms. Each of the packets will then execute a circular trajectory around the harmonic potential due to the cylindrical symmetry. Upon

completing one revolution, the atoms will return to their starting point at which the  $y$ -pulse was applied. At this point we will apply a second, identical pulse along the  $y$ -direction. This will recombine the packets and create two interferometers. This proposed interferometer is shown schematically in figure 5.1. The number of atoms that return to rest in each will depend on the Sagnac phase as well as other phases that are common to both. The beauty of this implementation is that the Sagnac phase is differential while other sources of phase (such as vibrations) are not. This will allow for the two interferometers to be used in tandem to reduce errors. This dual interferometer technique has been used previously to great avail for a similar rotationally sensitive atom interferometer [59].

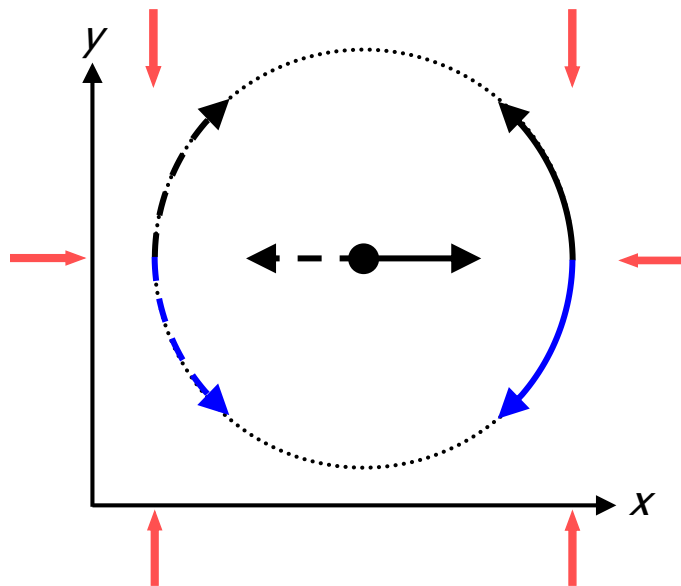


**Figure 5.1: Schematic Representation of Improved Sagnac Interferometer.**

Atoms starting at rest in the center of a cylindrically symmetric trap are split along the  $x$ -direction and then allowed to reach their classical turning point. By applying a second identical split along the  $y$ -direction the atoms will enclose an area thereby creating a Sagnac interferometer.

With the measurements of the trapping potential from Chapter 3, it is clear that the trap is deformable from nearly 10 Hz down to 1 Hz. Using our standard splitting operation

---

to drive atoms from rest to moving with  $\pm 2\hbar k$ , we should be able to achieve a range of circular trajectories with radii from  $150 \mu\text{m}$  -  $2 \text{ mm}$ , with corresponding transit times of  $79 \text{ ms}$  and  $1.6 \text{ s}$ . If we are able to measure the phase due to rotations to a precision of  $0.01 \text{ rad}$ , which is the shot noise limit for a condensate of  $10000$  atoms, this corresponds to range of rotation sensitivity relative to Earth's rotation rate of  $\delta\Omega/\Omega_{Earth} = 0.25$  to  $\delta\Omega/\Omega_{Earth} = 10^{-3}$ .

### Atomic Foucault Pendulum

While an interferometric measurement is in the future, there is another measurement which can be performed right away. If the atoms are again prepared at rest in the center of the trap and then kicked along one of the axes with cylindrical symmetry, then as the experimental platform rotates, the atoms will appear to rotate. This is sort of the atomic analog to the Foucault pendulum. With imaging resolution of  $\approx 2 \mu\text{m}$  and a modest kick producing cloud separation of  $0.5 \text{ mm}$ , then it is expected that the Earth's rotation rate can be measured with a total observation time of one minute even at the latitude of the lab.

### Gravity Revisited

In addition to the rotation sensing experiments, the gravity experiments can be revisited. First the bouncing experiment can be revisited using the cylindrically symmetric trap. This should allow for longer total times and therefore higher precision to the measurement of gravity.

Furthermore, with the implementation of the asymmetric splitting/recombination operations ( $|0\rangle \leftrightarrow |\pm 2\rangle$ ), the ladder type interferometer shown in figure 5.2 will be possible.

The basic principle of operation will be to start with the atoms at rest in the center of the trapping potential. A Bragg pulse will then be applied to kick the atoms upward along  $z$ . The trapping potential will be turned off and the atoms will undergo free-fall. When the atoms reach the peak of their flight and come to rest momentarily they will be split into two

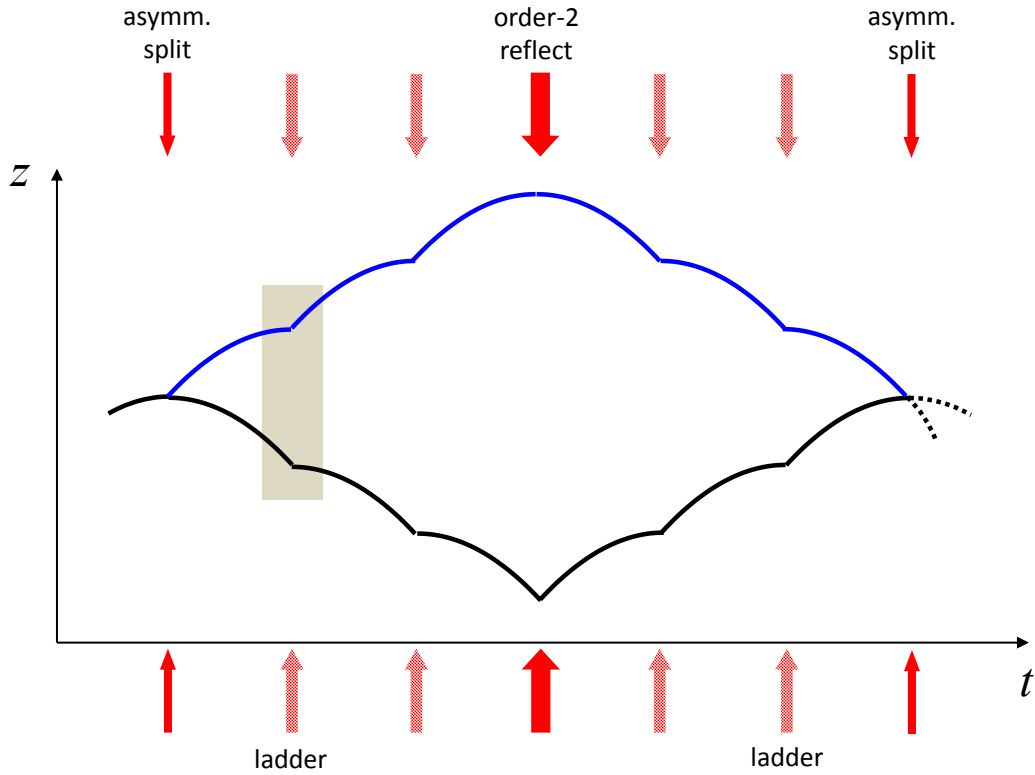


**Figure 5.2: Schematic Representation of Improved Gravimeter.** This implementation allows for large arm separation, but requires a special pulse sequence to achieve the transitions shown in the gray box, which we refer to as ladder pulses.

packets using the asymmetric splitting operation,  $(|0\rangle \rightarrow \frac{1}{\sqrt{2}}(|0\rangle + |2\hbar k\rangle))$ . The atoms will then undergo free-fall again until the upward moving packet again reaches its maximum and momentarily returns to rest. The time between the initial split and the upper packet returning to rest is  $\tau = 2\hbar k/(mg)$ , where  $k$  is the wavenumber of the Bragg beams and  $g$  is the acceleration due to gravity. At this point, to extend the separation of the interferometer, the atoms are kicked again. The lower packet needs to be driven from  $|-2\hbar k\rangle$  to  $|0\rangle$  and the upper packet needs to be driven from  $|0\rangle$  to  $|2\hbar k\rangle$ . This cannot be achieved with a single pulse, so we will need to first reflect the lower state,  $|-2\hbar k\rangle \rightarrow |2\hbar k\rangle$ , and then apply a  $\pi$ -pulse between  $|0\rangle \leftrightarrow |\pm 2\rangle$ . This two pulse sequence is shown schematically in

figure 5.3. This process can be repeated until the desired separation is reached. After  $N$  such laddering steps the total separation of the packets is given by  $\Delta z_{max} = \frac{4\hbar^2 k^2 N}{m^2 g}$ . At this point, a reflect pulse is applied, which leaves the upper packet at rest but reflects the lower packet. After another time  $\tau$ , the lower packet returns to rest. Now we need to apply the laddering pulse sequence again; however, now it drives the upper packet from  $|-2\hbar k\rangle \rightarrow |0\rangle$  and the lower packet from  $|0\rangle \rightarrow |2\hbar k\rangle$ . This process is repeated until the packets come back together and a final asymmetric recombination pulse is applied. The resulting interferometer requires a total time of  $T_{tot} = 2N\tau$ .

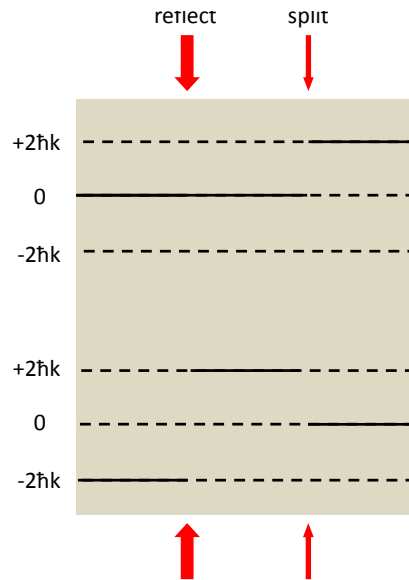


**Figure 5.3: Schematic Representation of Ladder Pulse Sequence.** The desired transitions are achieved by applying a reflect pulse followed immediately by an asymmetric splitting pulse. The momentum states are shown as solid lines.

The total phase difference developed between the two paths can be calculated and the phase shift from all of the Bragg pulses will cancel out (assuming the phase of the Bragg beams is steady) with the exception of the middle reflect pulse. The resulting phase difference is given by equation 5.1.

$$\phi = -\frac{p^3 N^2}{m^2 g \hbar} + \phi_r \quad (5.1)$$

Here  $p = 2\hbar k$  is the momentum imparted by a single Bragg pulse and  $\phi_r$  is the phase shift due to the center reflect pulse. It's worth noting that operations have been achieved which impart momentum kicks of up to  $24\hbar k$ , which would significantly improve the sensitivity although the fidelity of these large momentum transfer beamsplitters is still low [13]. Others have successfully demonstrated adiabatic rapid passage pulses which impart up to  $10\hbar k$  momentum kicks while maintaining a fidelity of around 97% [60]. To give an upper limit on the sensitivity achievable with the implementation described above using  $p = 2\hbar k$  kicks, we know that the best accuracy that we can hope to measure the phase with is the shot noise limit of 0.01 radians. For a modest number of pulses of  $N = 100$  the sensitivity would be  $\delta g/g \approx 10^{-8}$  with a separation of  $\Delta z_{max} \approx 1.4$  mm and a total interferometer time of  $T_{tot} \approx 240$  ms. For  $N = 1000$  the sensitivity would be  $\delta g/g \approx 10^{-10}$  with a separation of  $\Delta z_{max} \approx 1.4$  cm and a total interferometer time of  $T_{tot} \approx 2.4$  s. At this level of sensitivity, it begins to be competitive with other measurements which are on the same order [14]. That being said, this would be the best possible case and other technical limitations are likely to reduce the precision of our phase measurement.

# A | DB COPPER COIL CHIP

To produce the coils for the magnetic trap the following procedure was followed:

1. Cut the DBC (direct bond copper) Aluminum Nitride board into pieces the size of the desired chip dimensions (Approximately 1"X1"). Exact dimensions are not critical at this stage as the chip can be cleaned up later; however, it is important that at least one corner be squared to make mask alignment easier.
2. Sand the copper surfaces with course sandpaper using a small circular motion making sure that any burs are removed around the edges of the board. This will allow for good photoresist adhesion.
3. Rinse the board to remove any contaminants
  - i. Rinse first with Acetone,
  - ii. Then rinse with Water.
4. Immediately dry the board using the heat gun or an oven to prevent oxidation.

**NOTE: The following steps must be performed in a low light environment. All Fluorescent lamps and Incandescents over 40W can cause photoresist exposure.**

5. Apply MG Chemicals Dry Film Photoresist to the board:
  - i. Cut a piece of photoresist laminate large enough to cover both sides of the board.
  - ii. Fold laminate over the board such that all copper is covered.
  - iii. Run the covered board through a thermal laminator (3M Thermal Laminator) with the folded end of the photoresist entering first. (For this particular laminator the heat should be on the 5 mil setting.)
6. Examine the quality of the lamination:

Under a dim lamp (<40W incandescent), examine for large bubbles in the resist. If any are present, the photoresist should be removed with acetone and the process started over.
7. Expose photoresist to UV light:
  - i. Align the negative photomask with the board using the squared corner. This will allow a reference when lining up the opposite side of the board later.
  - ii. Tape the board to the photomask to prevent the board from moving during exposure.
  - iii. Place a piece of 1/4" clear acrylic over the board and photomask hold the board and mask in place.
  - iv. Expose the photoresist film with UV Source. Using a 250W Sunlamp placed 20" away from the board, the photoresist needs 10 minutes of exposure. (Exposure can also be performed using another source; however, the exposure time will need to be determined. It is also a good idea to have the UV source somewhat far from the board, such that the rays are close to collimated when they reach the board as this will create the cleanest lines in the resist.)
  - v. Align the mask on the other side of the board such that the patterns overlap properly.

vi. Repeat taping and exposure.

8. Develop photoresist:

- i. Place chip into MG Chemicals Dry Film Photoresist Developer solution, diluted as per the instructions found on the bottle for approximately one minute.
- ii. Using a soft foam swab soaked in the solution, gently scrub the non-exposed resist off of the board.
- iii. Continue scrubbing until only the exposed pattern remains. The developed portions should appear dark blue. Be sure the light blue (unexposed) portions are clean. This is easiest to see under a lamp, but exposure should be minimized to avoid UV hardening of the photoresist.

9. Examine board for quality of mask transfer:

Look for discoloration in the transferred pattern as well as spots that are visibly detached from the copper. The discoloration is the telltale sign of the mask not adhering well to the copper surface and is likely caused by air bubbles. If either of these things is present, gently rub the mask in those areas. If the areas flake off, then the mask should be completely removed and the board restarted.

**NOTE: At this point, the board may be exposed to normal lighting.**

10. Etch the Board:

- i. Mix the etchant: In a small container (preferably one that the board can fit flat on the bottom) mix 2 parts  $H_2O_2$



# B | WAVEGUIDE MECHANICAL DRAWINGS

Contained on the following pages are mechanical drawings for the magnetic trap parts as well as the parts for the support structure for the trap.

# Coil Chip

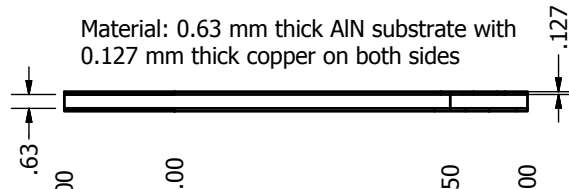
page 1 of 2

Date: 04/07/2011

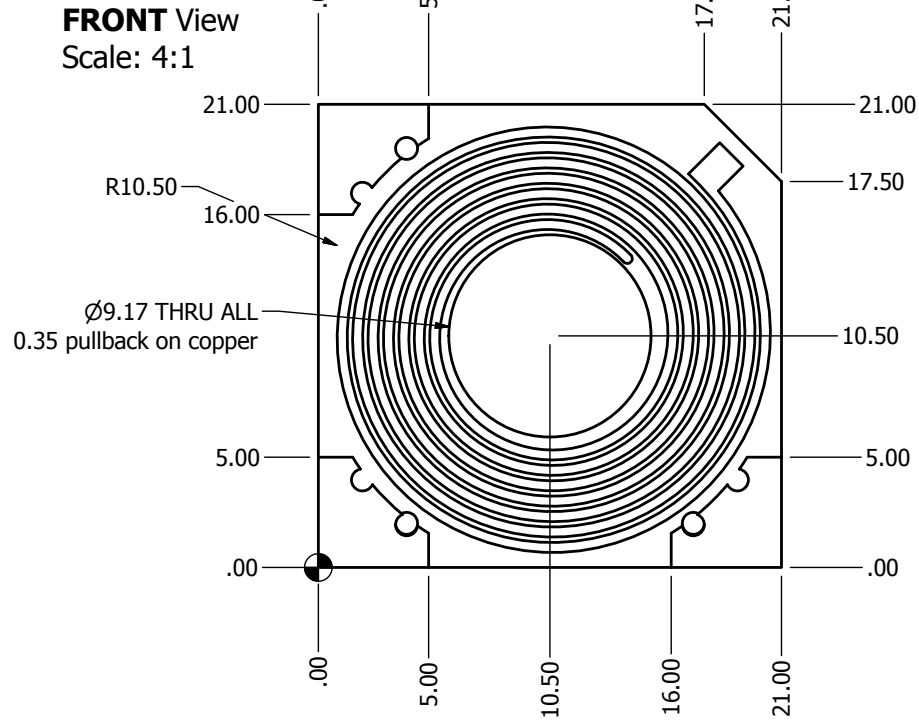
All dimensions are in mm unless noted

Contact: Robert Horne  
434-924-7520  
rah9w@virginia.edu

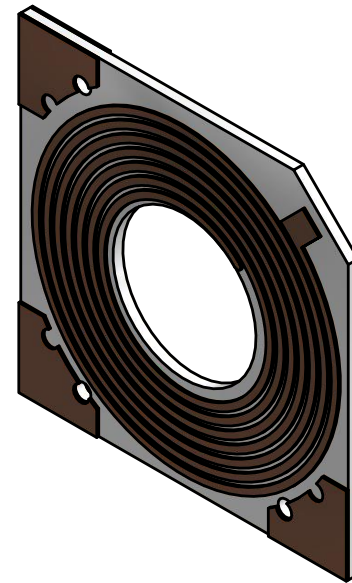
**SIDE View**  
Scale: 4:1



**FRONT View**  
Scale: 4:1



**ISO Top Right View**  
Scale: 4:1



# Coil Chip

page 2 of 2

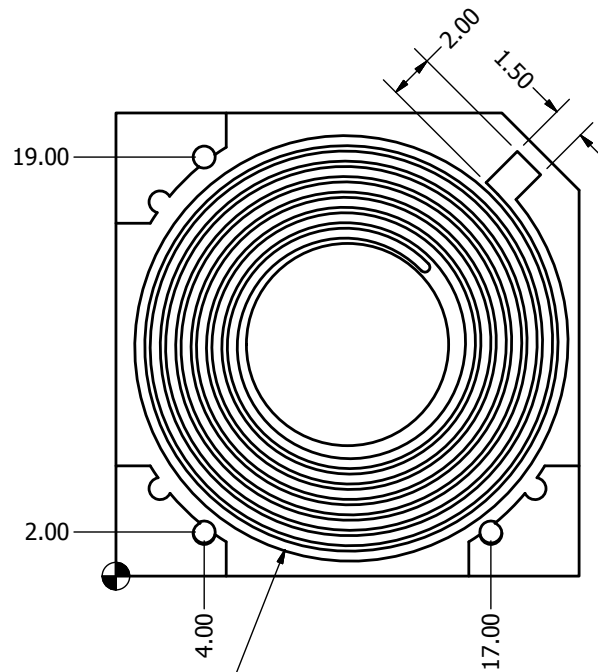
Date: 04/07/2011

All dimensions are in mm unless noted

## FRONT View

Focus on Spiral

Scale: 4:1



Spiral Turns: 7

Inner Radius: 4.963 mm (measured from center of hole to inside of copper trace)

Spiral Pitch: 0.7 mm

Trace Width: 0.4 mm

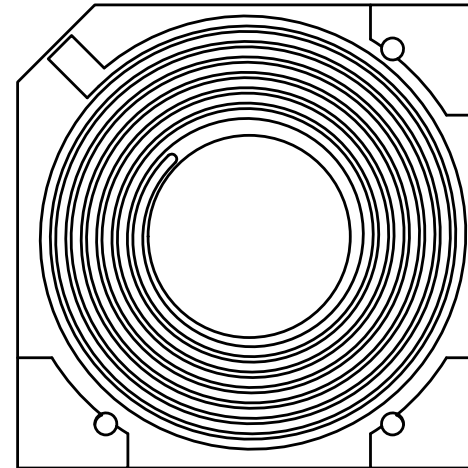
Contact: Robert Horne  
434-924-7520  
rah9w@virginia.edu

## BACK View

Focus on Spiral

Scale: 4:1

Front and Back patterns are the same with rotation



# TOP Trap Mount

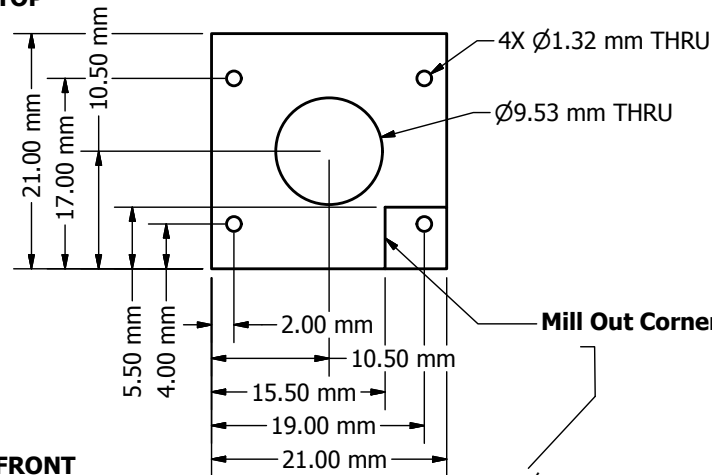
Material: Boron Nitride

Quantity: 1

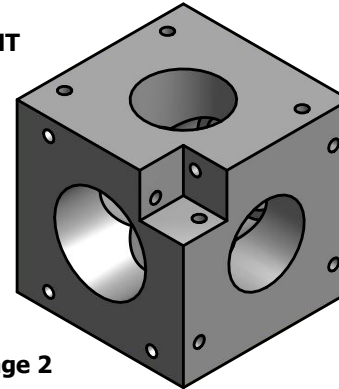
page: 1/2

Robert Horne  
rah9w@virginia.edu  
924-7520

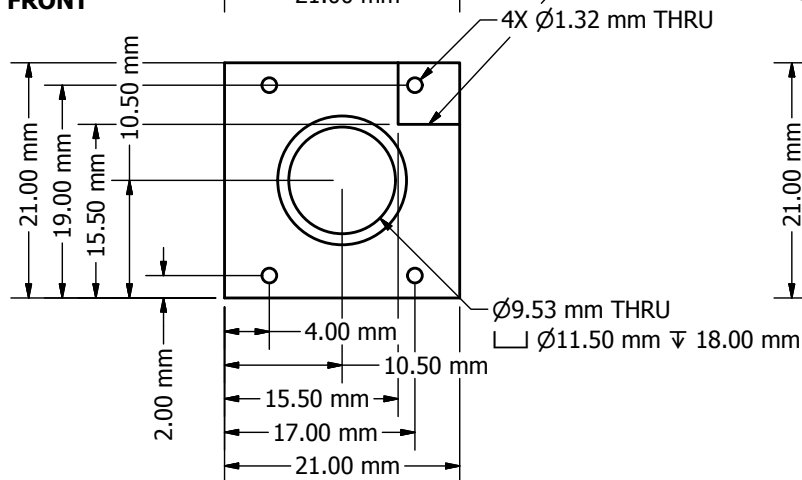
TOP



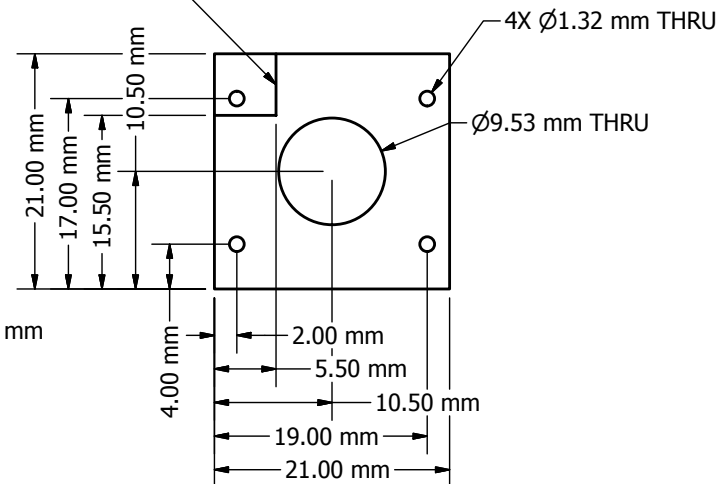
ISO TOP RIGHT



FRONT



RIGHT

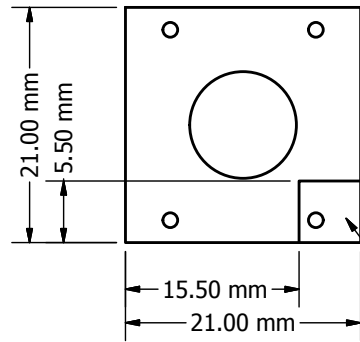


# TOP Trap Mount

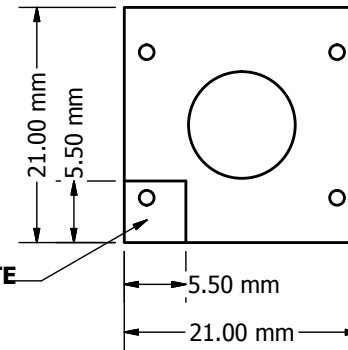
page: 2/2

Robert Horne  
rah9w@virginia.edu  
924-7520

BACK

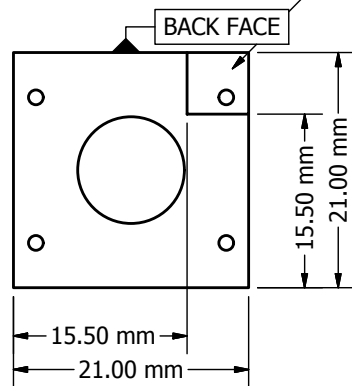


LEFT

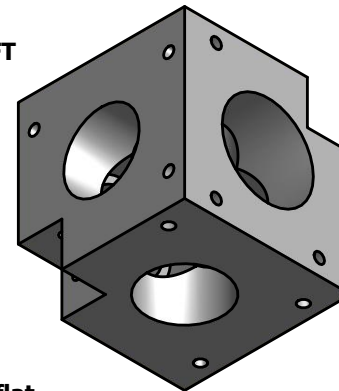


Mill Out Corner: see NOTE

BOTTOM



ISO BOTTOM LEFT



NOTE: Fillet edges as needed, but be sure areas around thru holes are flat

# Boron Nitride Arm

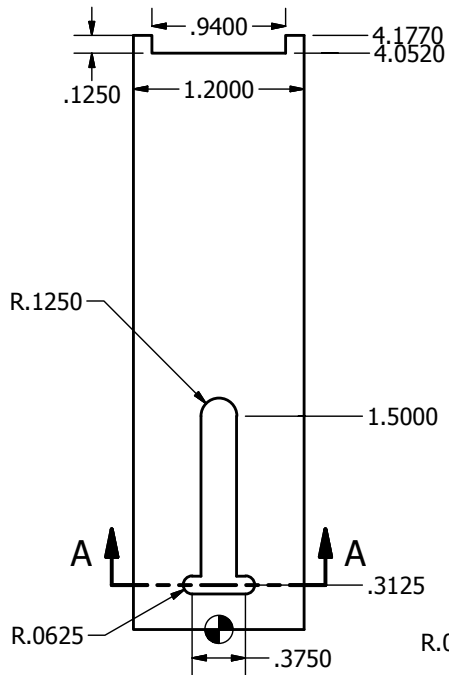
Material: Boron Nitride

Date: 6/23/2011

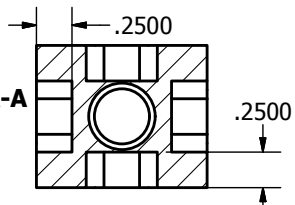
Page 1 of 1

Robert Horne  
rah9w@virginia.edu  
434-924-7520

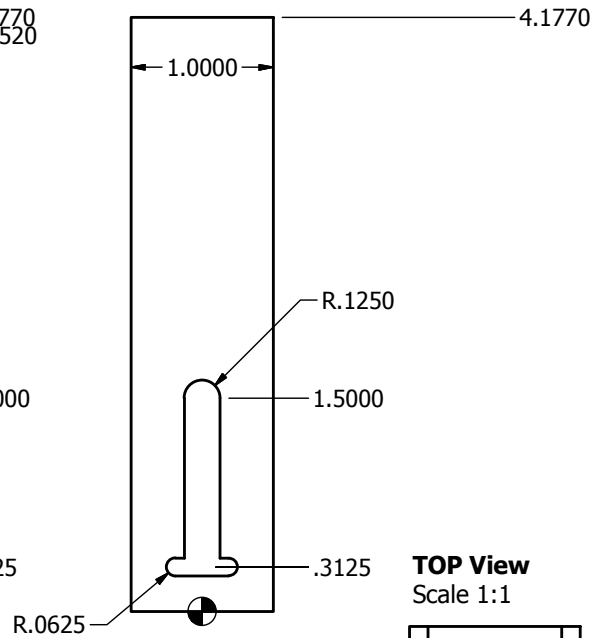
**FRONT View**  
Scale 1:1



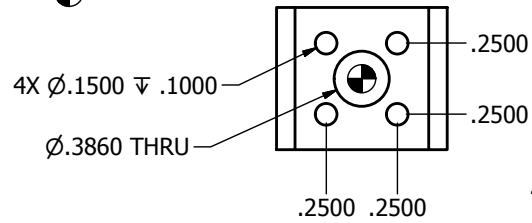
**SECTION A-A**  
SCALE 1 : 1



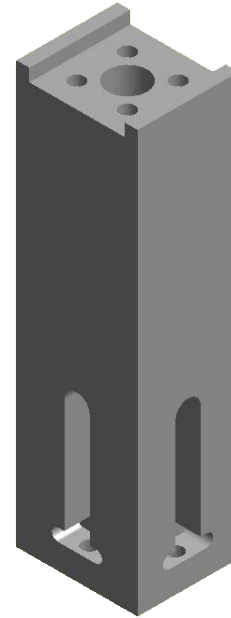
**RIGHT View**  
Scale 1:1



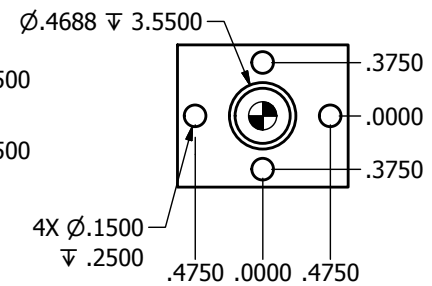
**TOP View**  
Scale 1:1



**ISO Top Right View**  
Scale 1:1



**BOTTOM View**  
Scale 1:1



# Vespel Parts

Material: Vespel  
 Date: 6/23/2011  
 Page 1 of 1

**Robert Horne**  
 rah9w@virginia.edu  
 434-924-7520

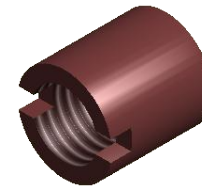
## Screw

**ISO Top Right View**  
 Scale 2:1

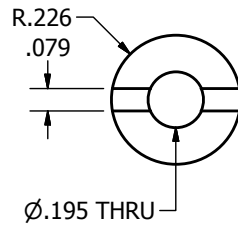


## Nut

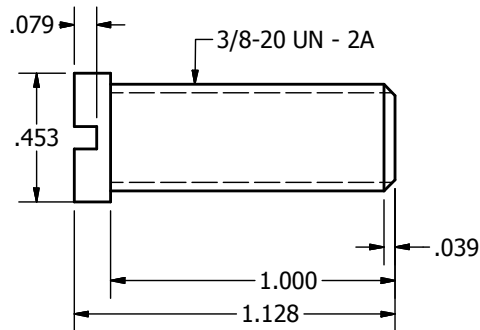
**ISO Top Right View**  
 Scale 2:1



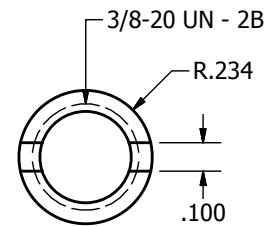
**FRONT View**  
 Scale 2:1



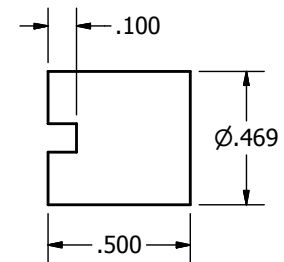
**RIGHT View**  
 Scale 2:1



**FRONT View**  
 Scale 2:1



**RIGHT View**  
 Scale 2:1



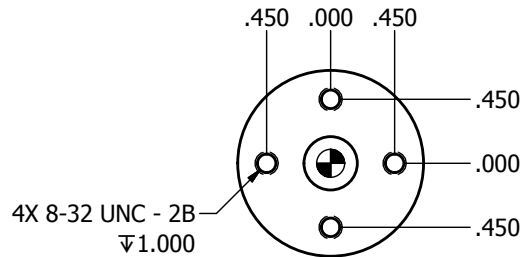
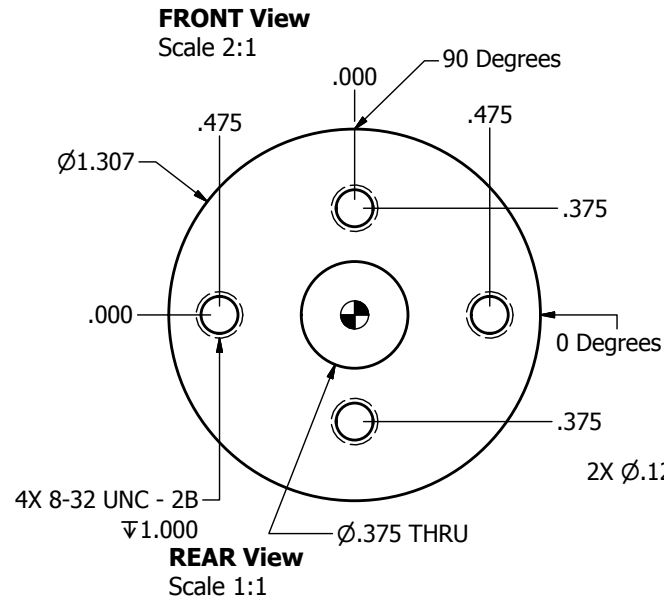
# Aluminum Arm

Material: Aluminum-6061

Date: 6/22/2011

Page 1 of 1

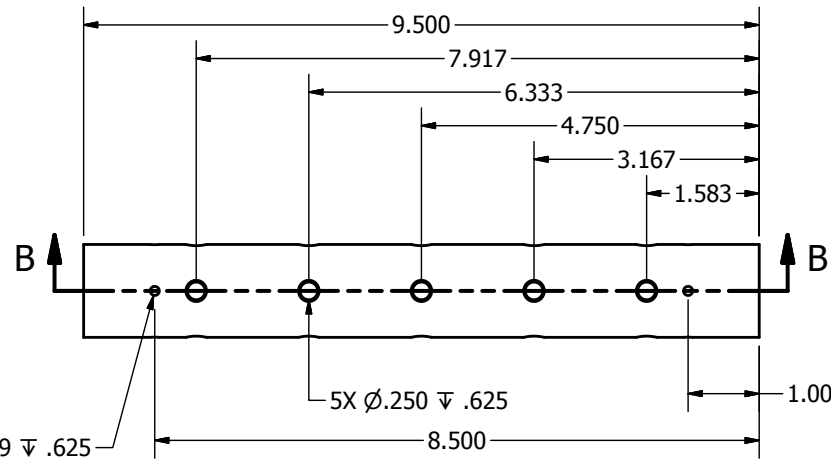
Robert Horne  
rah9w@virginia.edu  
434-924-7520



**0 DEGREE View**

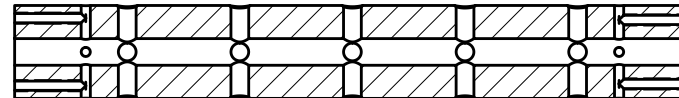
**\*\*Pattern repeated at 90 degree intervals around cylinder\*\***

Scale 1:2



**SECTION B-B View**

SCALE 1:2



# Pedestal

Material: Aluminum-6061

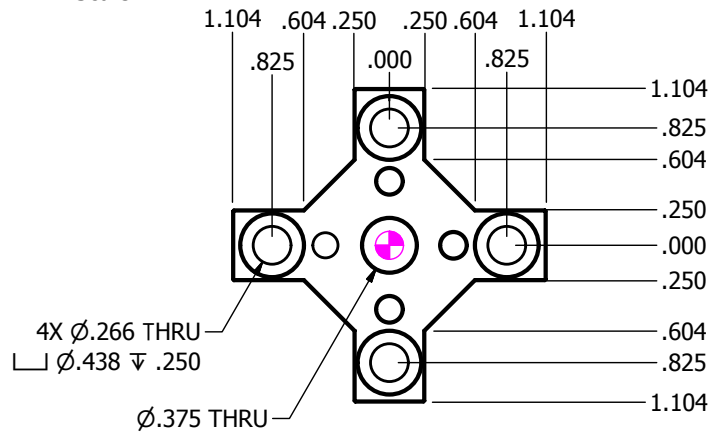
Date: 6/22/2011

Page 1 of 1

**Robert Horne**  
rah9w@virginia.edu  
434-924-7520

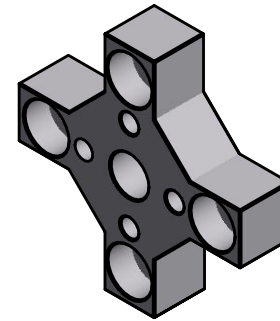
## FRONT View

Scale 1:1



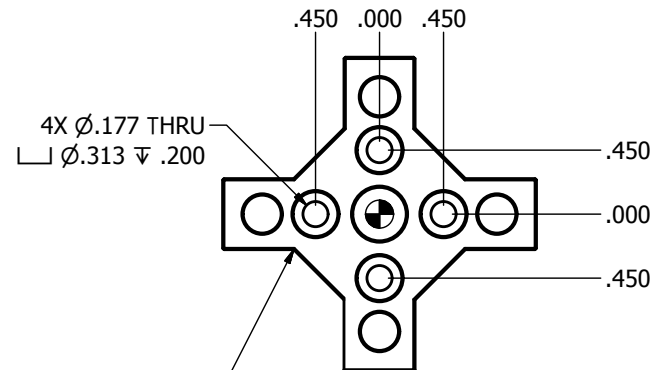
## ISO Top Right View

Scale 1:1



## REAR View

Scale 1:1

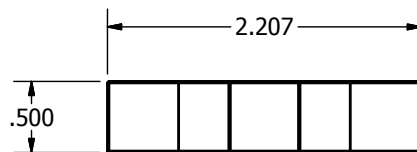


## SIDE View

**\*NOTE\***

**All sides are the same**

Scale 1:1



**\*Round Corners as Needed\***

# Vacuum Flange

Material: Stainless Steel, 440C

Date: 6/21/2011

Page 1 of 2

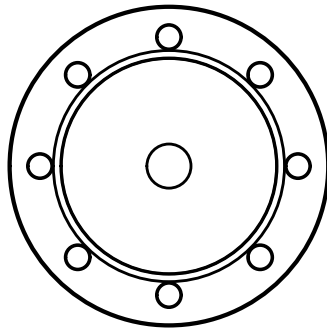
**\*\*Important\*\***

Please protect the knife edge on both sides of the flange

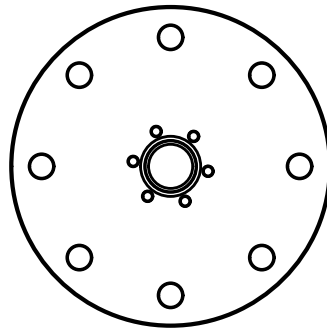
Robert Horne  
rah9w@virginia.edu  
434-924-7520

## Original

**FRONT View**  
Scale 1:2

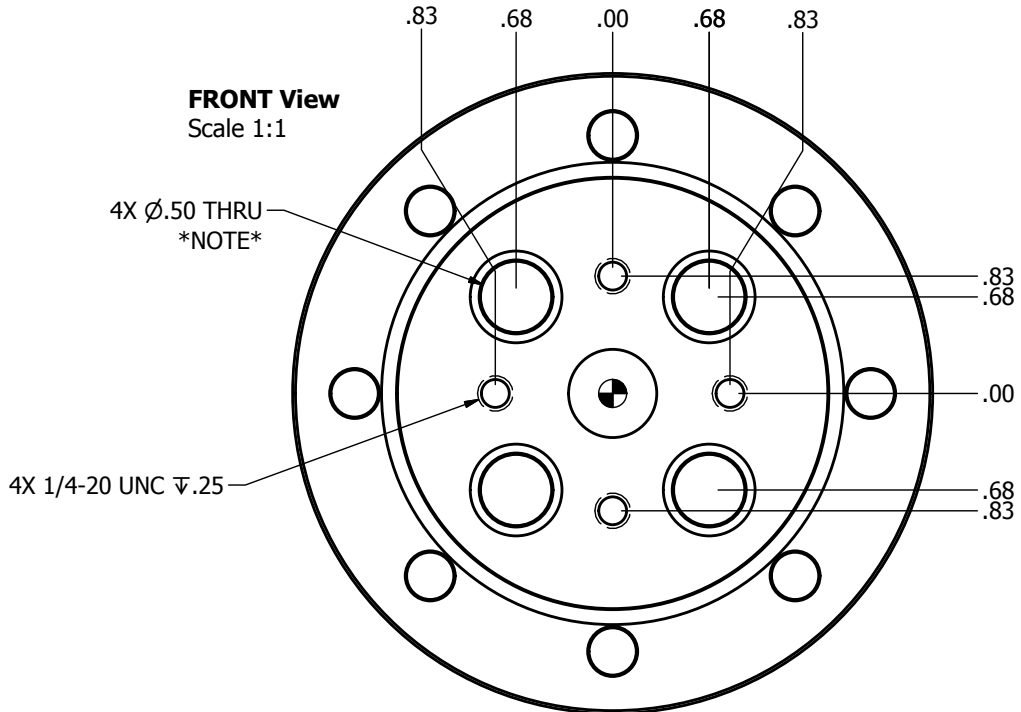


**REAR View**  
Scale 1:2



## Modifications

**FRONT View**  
Scale 1:1



### \*NOTE\*

The four 0.50" holes may need to be adjusted. The 0.50" electrical feedthroughs will be welded into these holes. For the 4-pin feedthroughs, please align the pins with the 0.5 holes on the flange (see page 2). Also, the ring around these holes is representative of a recession needed for welding. Please use a 1/16" endmill to make this recession.

# Vacuum Flange

Material: Stainless Steel, 440C

Date: 6/21/2011

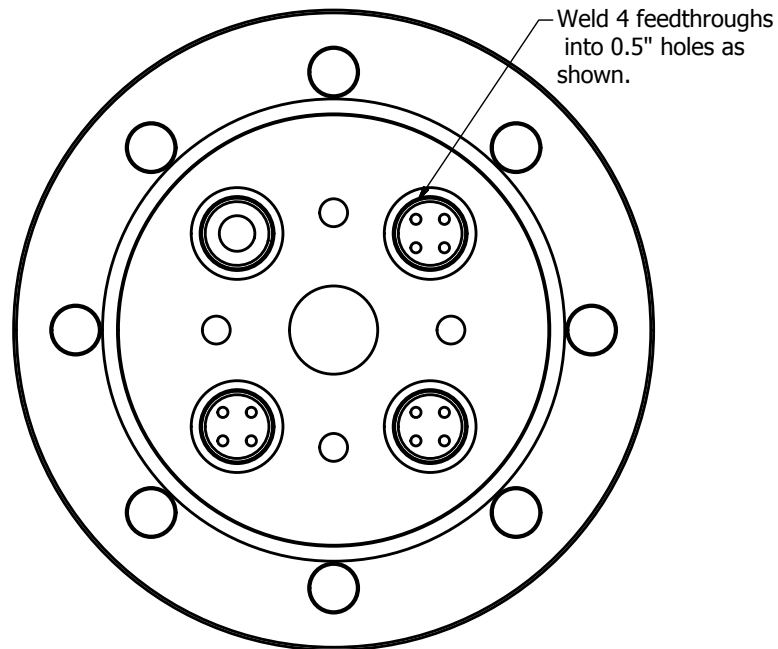
Page 2 of 2

**Robert Horne**  
rah9w@virginia.edu  
434-924-7520

## Welding

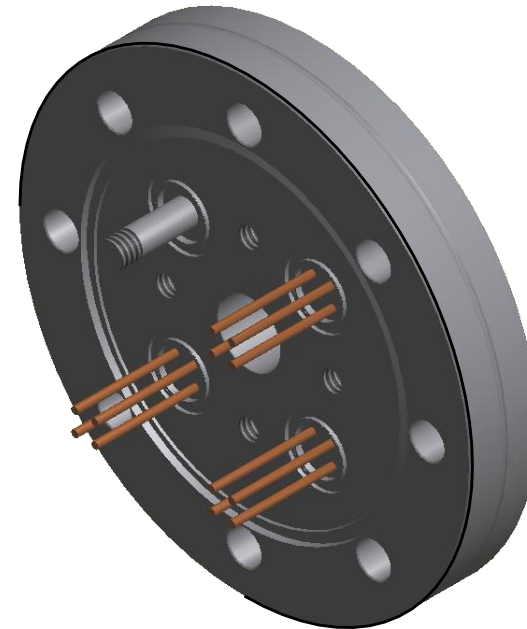
**FRONT View**

Scale 1:1



**ISO Top Right View**

Scale 1:1





# C | MAGNETIC TRAP DRIVE CIRCUIT

This appendix provides more detail on the voltage generation circuit for the magnetic trap described in chapter 3. Figure C.1 shows the layout of the front panel of the voltage generation box. The two function generator inputs ( $FG_1$  and  $FG_2$ ), the bias control voltage input ( $V_0$ ), the quadrupole control voltage input ( $V_1$ ) and a digital control input (Dig. Con.) which allows the outputs to be grounded are located on the front panel. Additionally, a monitor output for each signal is available. There are also three switch in a vertical line between the digital control and the output monitor BNCs. These allow the digital control of the X, Y, and both Z signals to be switched on, off or to computer control. The switch positions and corresponding settings are: UP is ON, DOWN is OFF, and MIDDLE is Computer controlled.

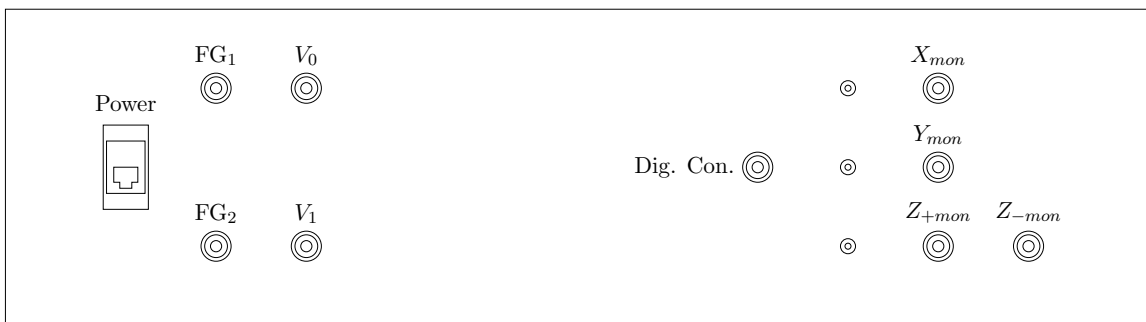


**Figure C.1: Front Panel layout for Magnetic Trap Voltage Generation Box.**

Figure C.2 shows the layout of the rear panel of the voltage generation box. This panel has on it the XLR connectors for output to the RMX850 Audio amplifiers as well as inputs

for the sense voltage for each signal to be feed through to the negative input of the audio amplifiers. Additionally, there are access holes to the ten adjustment potentiometers. The function of each of these potentiometers is discussed in C.1.

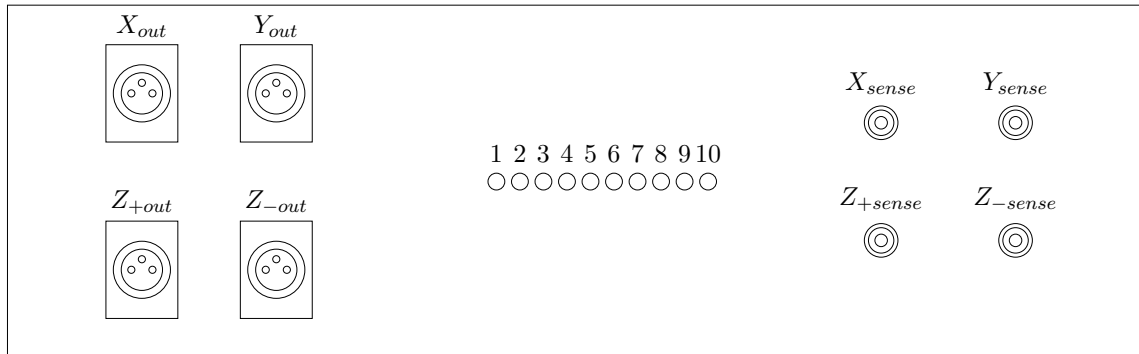


**Figure C.2: Rear Panel Layout for Magnetic Trap Voltage Generation Box.**

Pot. #	What it Adjusts
1	$V_{S2}$
2	$V_{C2}$
3	$V_{S1}$
4	$V_{C1}$
5	$V_{1z-}$
6	$V_{1z+}$
7	$V_{0z-}$
8	$V_{0z+}$
9	$\phi_2$
10	$\phi_1$

**Table C.1: Magnetic Trap Voltage Generation Box Potentiometer Adjustment Key.** This table provides a key to what each potentiometer on the voltage generation box actually adjusts for the output signals.

On the following pages are a detailed circuit diagram of voltage generation circuit shown in block form in figure 3.13. The quadrature sources are shown in figure C.3. The control voltage input buffers as well as the z summing and and difference amplifiers are shown in figure C.4. The multipliers configuration is shown in figure C.5. The output buffers, switches and monitors are shown in figure C.6.

Additionally, the pin connections for the Vector card on which the circuit was built is shown in table C.2 to aid in future debugging or circuit modification. All of the amplifiers shown in these diagrams were AD712 low-noise op amps. The multipliers used were AD534KDZ precision analog multipliers.

It is not shown in the circuit diagram but each sense input from the rear panel is connected to the corresponding negative output for each of the XLR connectors. These signals are shorted together on the circuit board.

Pin	Connection	Pin	Connection
A	Ground	1	NC
B	$FG_1$ Input	2	+15V Supply
C	Ground	3	NC
D	$FG_2$ Input	4	+5V Supply
E	Ground	5	NC
F	Bias Control Input ( $V_0$ )	6	NC
H	Ground	7	NC
J	Quadrupole Control Input ( $V_1$ )	8	NC
K	Ground	9	NC
L	X Digital Control Input ( $V_{xcon}$ )	10	+5V Output
M	Y Digital Control Input ( $V_{ycon}$ )	11	NC
N	Z Digital Control Input ( $V_{zcon}$ )	12	NC
P	X Output+ ( $V_{xout+}$ )	13	X Output- ( $V_{xout-}$ )
R	X Output+ Monitor ( $V_{xmon}$ )	14	X Sense ( $X_{sense}$ )
S	Y Output+ ( $V_{yout+}$ )	15	Y Output- ( $V_{yout-}$ )
T	Y Output+ Monitor ( $V_{ymon}$ )	16	Y Sense ( $Y_{sense}$ )
U	Z- Output+ ( $V_{z-out+}$ )	17	Z- Output- ( $V_{z-out-}$ )
V	Z- Output+ Monitor ( $V_{z-mon}$ )	18	Z- Sense ( $Z-sense$ )
W	Z+ Output+ ( $V_{z+out+}$ )	19	Z+ Output-
X	Z+ Output+ Monitor ( $V_{z+mon}$ )	20	Z+ Sense ( $Z+sense$ )
Y	NC	21	-15V Supply
Z	Ground	22	Ground

**Table C.2: Card Edge Connections.**

Prior to building the voltage generation circuit, the noise spectrum of the AD534KDZ multipliers was measured using two multipliers and a lock-in detector and spectrum analyzer. The setup used for these measurements is shown in figure C.7.

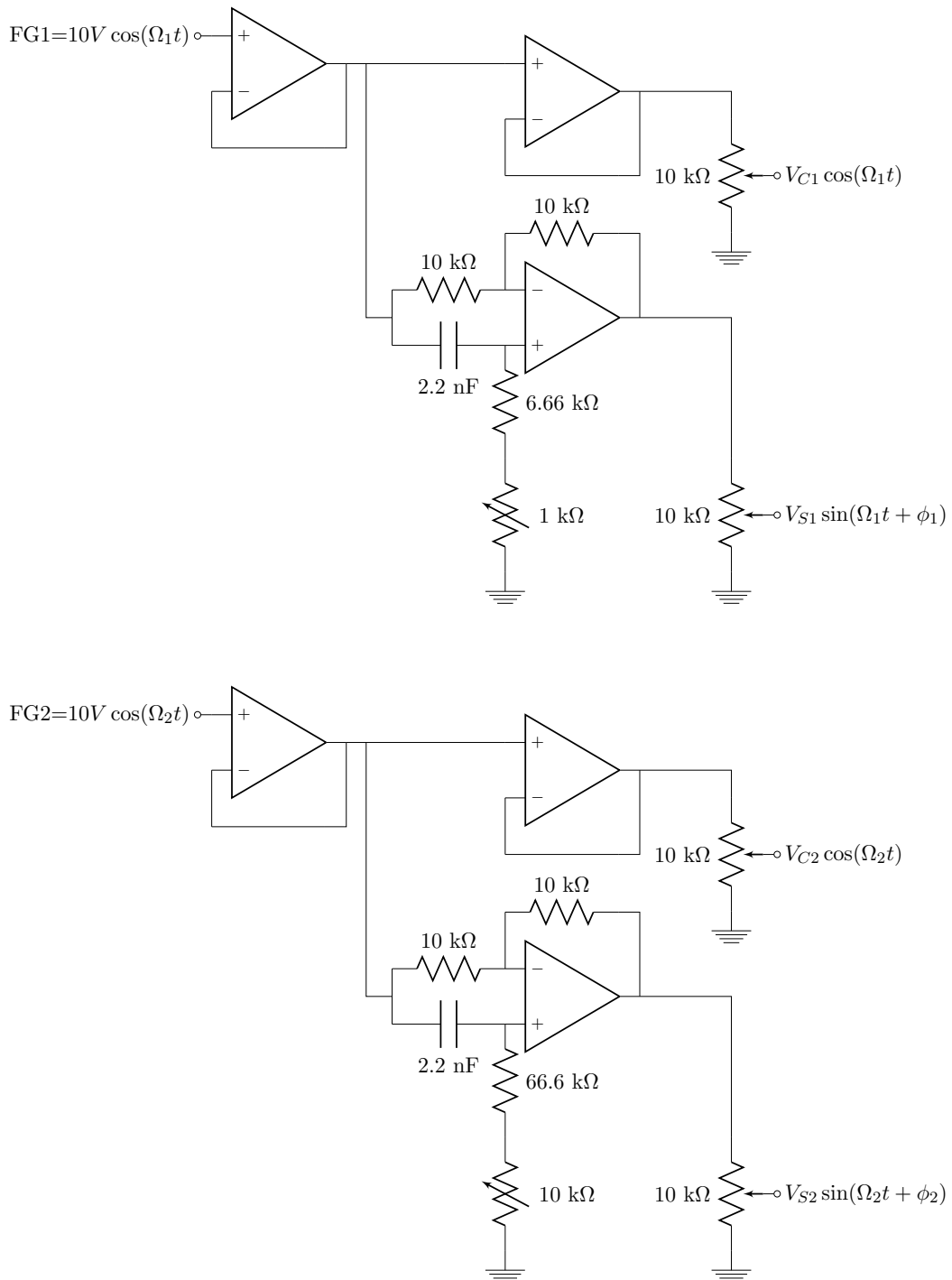


Figure C.3: Quadrature Sources.

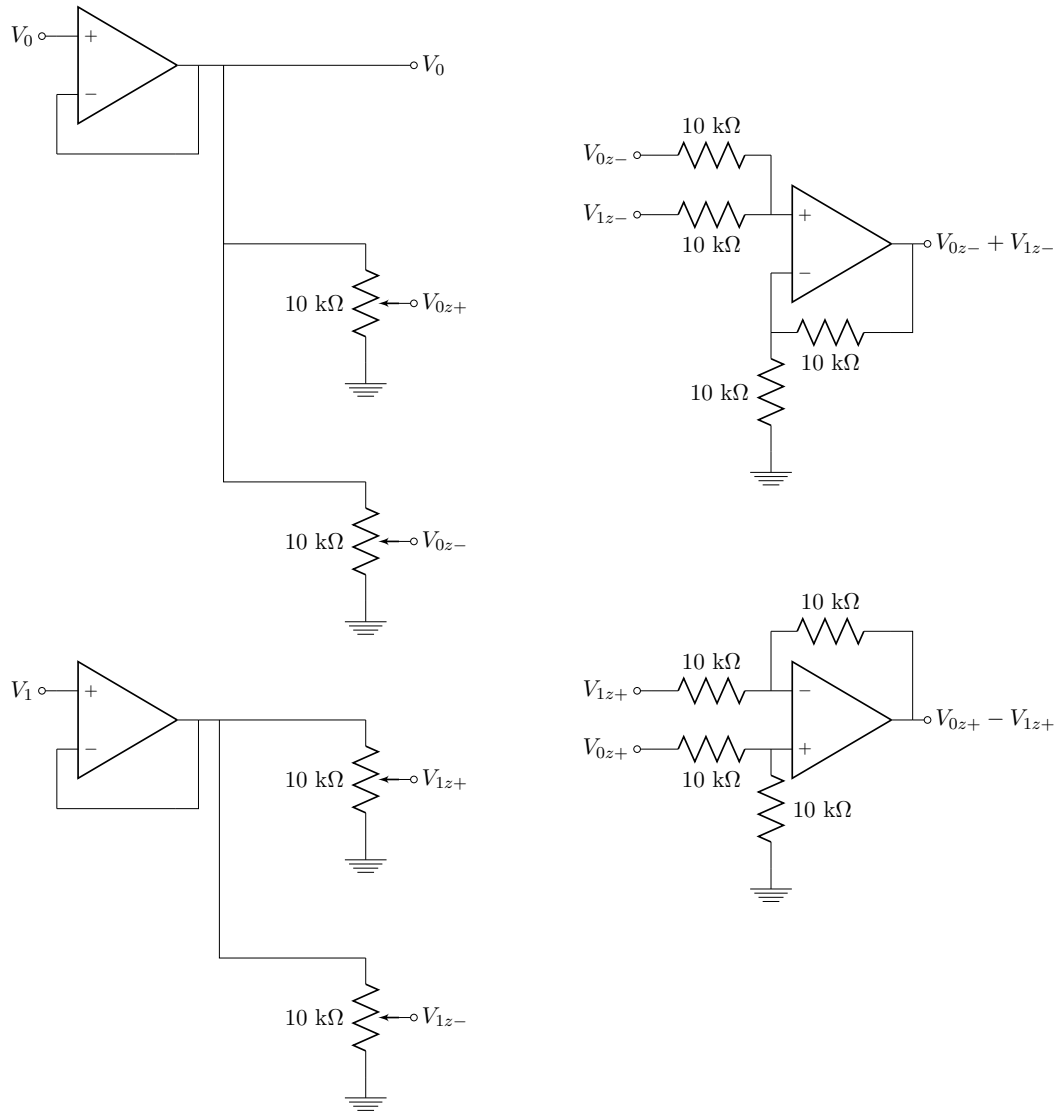
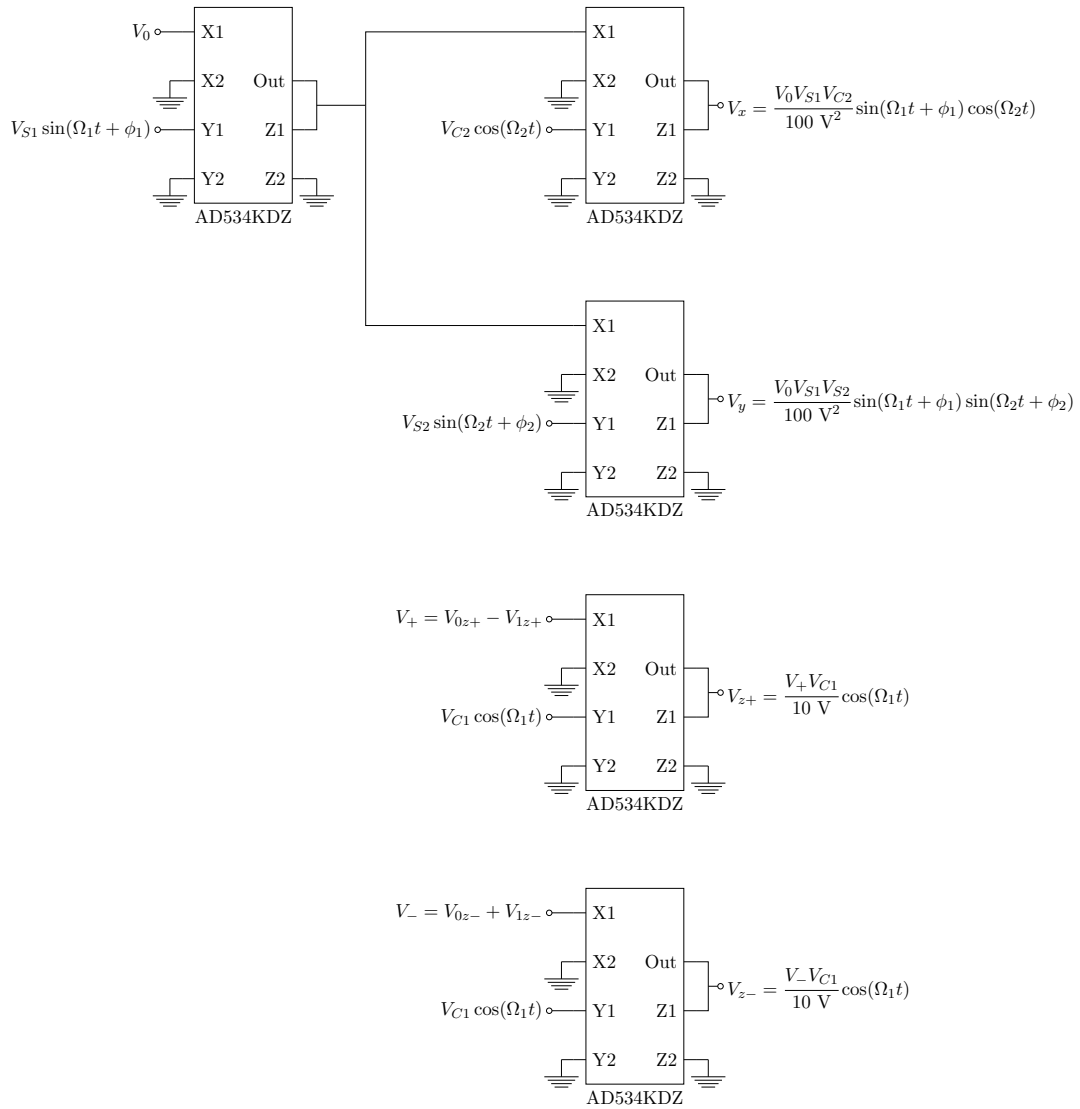
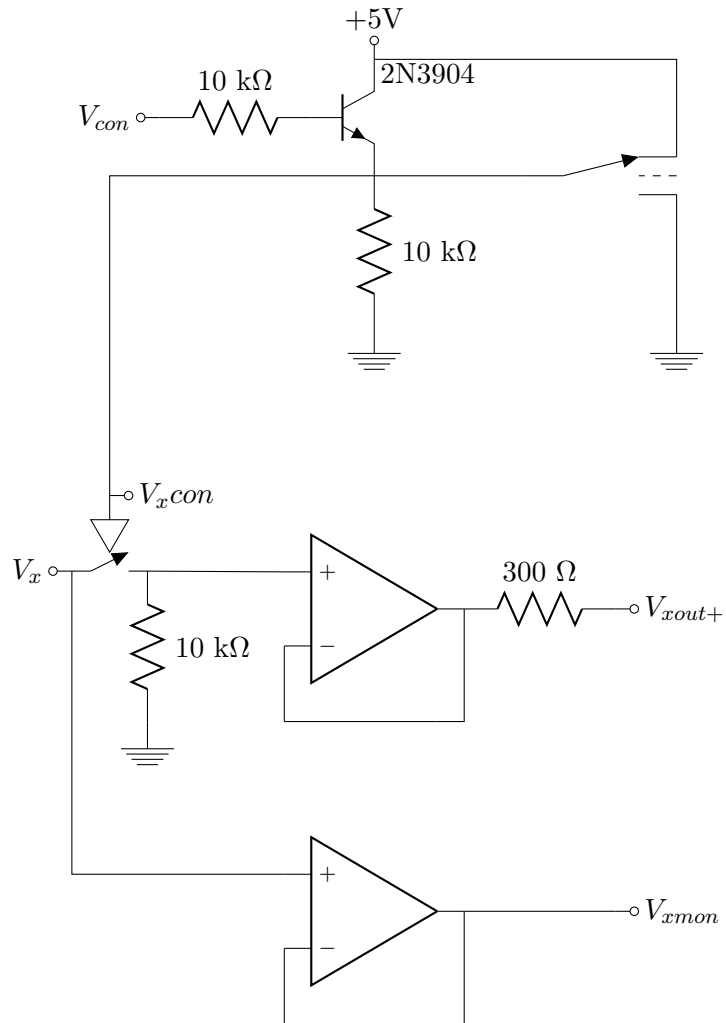


Figure C.4: Control Voltage Buffers and Summing and Difference Amplifiers.



**Figure C.5: Multiplier Configuration.**



**Figure C.6: Output Buffers and Switches.** This only shows the X signal output buffers and switches; however, the Y is identical and the  $Z_{\pm}$  are similar, but share the same switching signal to the output.

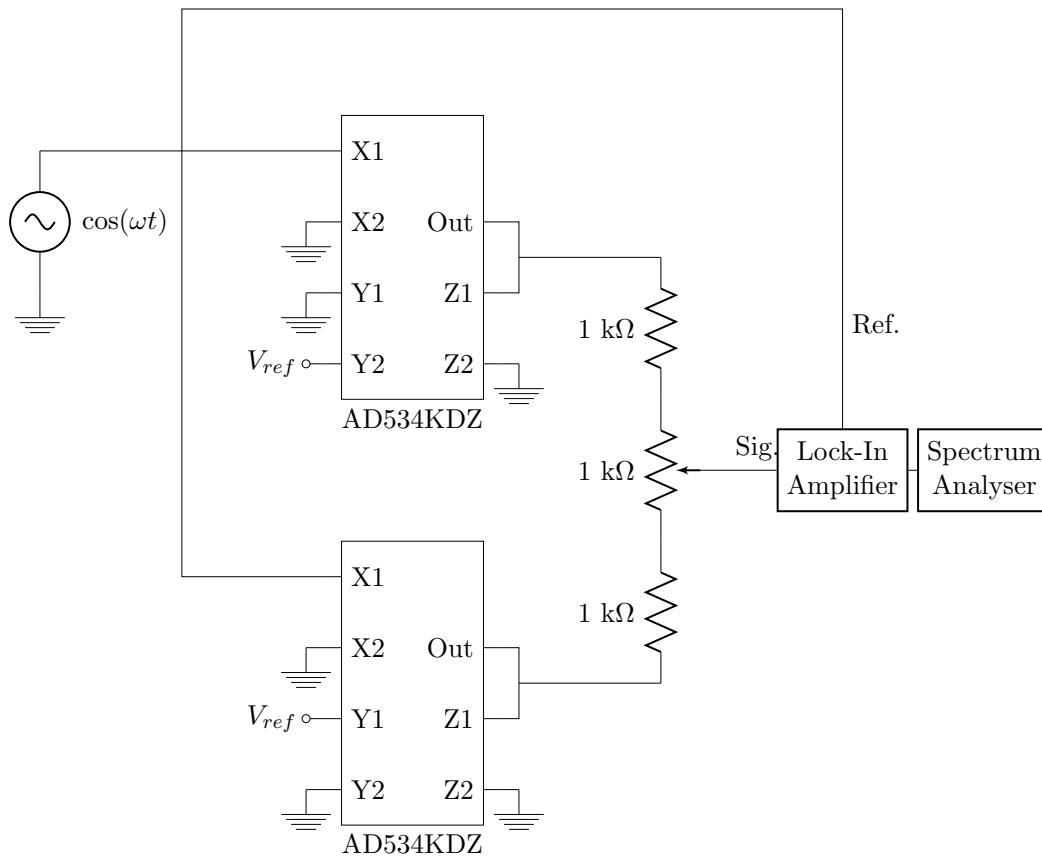


Figure C.7: Multiplier Noise Spectrum Measurement Setup.

Two sets of amplitude and phase noise spectra were measured at different reference voltages,  $V_{ref}$ . The 1X data sets were with  $V_{ref} = 10V$  and the 0.1X data sets were with  $V_{ref} = 1V$ . The other input was from an Agilent 33210A function generator outputting a sinusoidal waveform with  $20 V_{pp}$  signal at a frequency of  $f_0 = 12$  kHz. The noise spectral density measurements are shown in figure C.8.

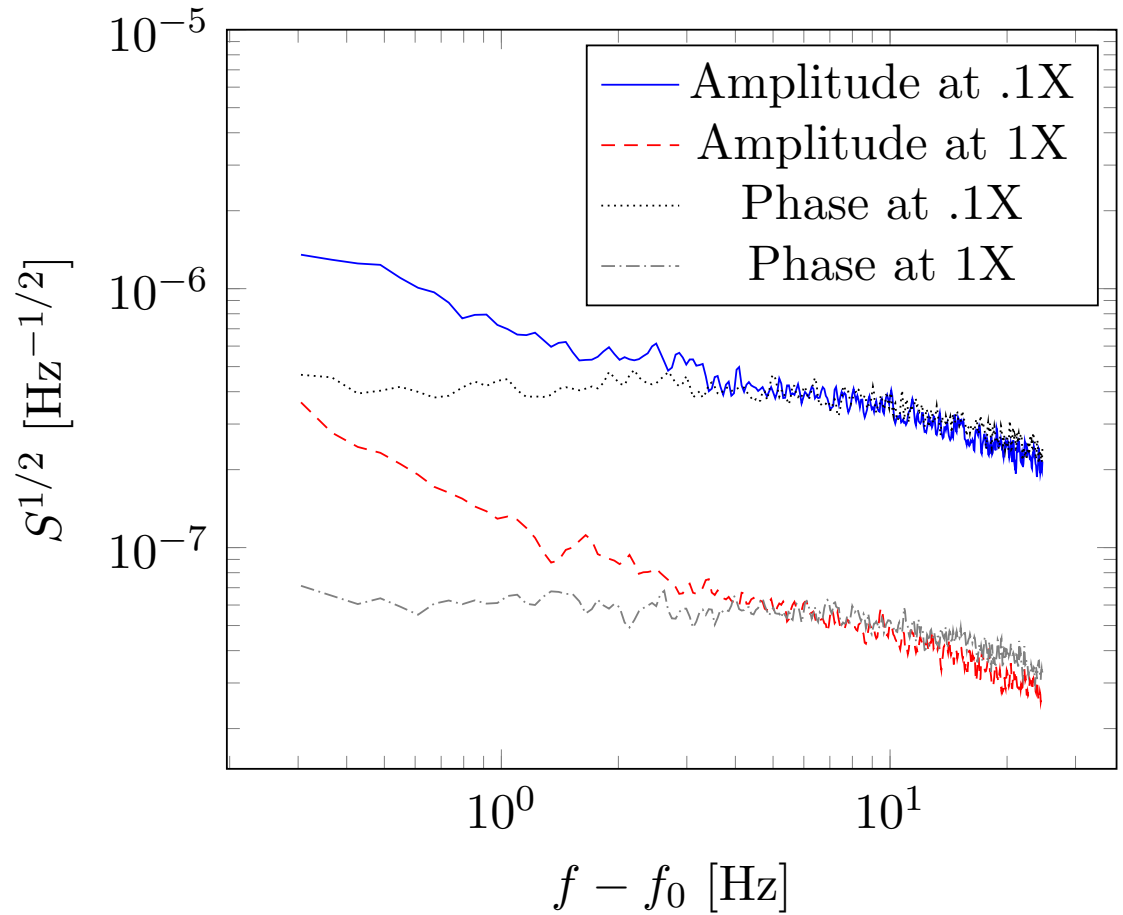


Figure C.8: Multiplier Noise Spectrum.  $f_0 = 12$  kHz.



## REFERENCES

- [1] L. V. de Broglie. *Recherches sur la thorie des Quanta*. PhD thesis, Paris, 1924.
- [2] C. Davisson and L. H. Germer. Diffraction of Electrons by a Crystal of Nickel. *Phys. Rev.*, 30(6):705–740, 1927.
- [3] I. Estermann and A. Stern. Beugung von Molekularstrahlen. *Z. Phys.*, 61:95, 1930.
- [4] D. W. Keith, M. L. Schattenburg, Henry I. Smith, and D. E. Pritchard. Diffraction of Atoms by a Transmission Grating. *Phys. Rev. Lett.*, 61(14):1580–1583, 1988.
- [5] P. J. Martin, B. G. Oldaker, A. H. Miklich, and D. E. Pritchard. Bragg Scattering of Atoms from a Standing Light Wave. *Phys. Rev. Lett.*, 60(6):515–518, 1988.
- [6] O. Carnal and J. Mlynek. Young’s Double-Slit Experiment with Atoms: A Simple Atom Interferometer. *Phys. Rev. Lett.*, 66(21):2689–2692, 1991.
- [7] D. W. Keith, C. R. Ekstrom, Q. A. Turchette, and D. E. Pritchard. An interferometer for atoms. *Phys. Rev. Lett.*, 66(21):2693–2696, 1991.
- [8] F. Riehle, Th. Kisters, A. Witte, J. Helmcke, and Ch. J. Bordé. Optical Ramsey Spectroscopy in a Rotating Frame: Sagnac Effect in a Matter-Wave Interferometer. *Phys. Rev. Lett.*, 67(2):177–180, 1991.

- 
- [9] M. R. Andrews, C. G. Townsend, H. J. Miesner and D. S. Durfee, D. M. Kurn, and W. Ketterle. Observation of Interference Between Two Bose Condensates. *Science*, 275(5300):637–641, 1997.
- [10] Pippa Storey and Claude Cohen-Tannoudji. The Feynman path integral approach to atom interferometry. A tutorial. *J. Phys. II France*, 4:1999–2027, 1994.
- [11] Alexander D. Cronin, Jörg Schmiedmayer, and David E. Pritchard. Optics and interferometry with atoms and molecules. *Rev. Mod. Phys.*, 81:1051–1129, Jul 2009.
- [12] Mark Kasevich and Steven Chu. Atomic interferometry using stimulated Raman transitions. *Phys. Rev. Lett.*, 67:181–184, Jul 1991.
- [13] Holger Müller, Sheng-wei Chiow, Quan Long, Sven Herrmann, and Steven Chu. Atom Interferometry with up to 24-Photon-Momentum-Transfer Beam Splitters. *Phys. Rev. Lett.*, 100:180405, May 2008.
- [14] A. Peters, K. Y. Young, and S. Chu. High-precision gravity measurements using atom interferometry. *Metrologia*, 38:25–61, 2001.
- [15] M. J. Snadden, J. M. McGuirk, P. Bouyer, K. G. Haritos, and M. A. Kasevich. Measurement of Earth’s Gravity Gradient with an Atom Interferometer-Based Gravity Gradiometer. *Phys. Rev. Lett.*, 81(5):971–974, 1998.
- [16] J. B. Fixler, G. T. Foster, J. M. McGuirk, and M. A. Kasevich. Atom Interferometer Measurement of the Newtonian Constant of Gravity. *Science*, 315:74–77, 2007.
- [17] T. L. Gustavson, P. Bouyer, and M. A. Kasevich. Precision Rotation Measurements with an Atom Interferometer Gyroscope. *Phys. Rev. Lett.*, 78(11):2046–2049, 1997.
- [18] J.M. Reeves, O. Garcia, B. Deissler, K.L. Baranowski, K.J. Hughes, and C.A. Sackett. Time-orbiting potential trap for Bose-Einstein condensate interferometry. *Phys. Rev. A*, 72:051605(R), 2005.

- 
- [19] O. Garcia, B. Deissler, K.J. Hughes, J.M. Reeves, and C.A. Sackett. Bose-Einstein condensate interferometer with macroscopic arm separation. *Phys. Rev. A*, 74:031601(R), 2006.
- [20] K. J. Hughes, J. H. T. Burke, and C. A. Sackett. Suspension of Atoms Using Optical Pulses, and Application to Gravimetry. *Phys. Rev. Lett.*, 102:150403, 2009.
- [21] Jeramy Hughes. *Optical manipulation of atomic motion for a compact gravitational sensor with a Bose-Einstein condensate interferometer*. PhD thesis, University of Virginia, 2008.
- [22] J. H. T. Burke and C. A. Sackett. Scalable Bose-Einstein-condensate Sagnac interferometer in a linear trap. *Phys. Rev. A*, 80:061603(R), 2009.
- [23] Eun Oh. *Asymmetric Splitting of Bose-Einstein Condensate*. PhD thesis, University of Virginia, 2014.
- [24] R. K. Pathria. *Statistical Mechanics*. Elsevier, Burlington, MA, 2nd edition, 1996.
- [25] C. J. Pethick and H. Smith. *Bose-Einstein Condensation in Dilute Gases*. University Press, Cambridge, 1st edition, 2002.
- [26] M. H. Anderson, J. R. Ensher, M. R. Matthews, C. E. Wieman, and E. A. Cornell. Observation of Bose-Einstein Condensation in a Dilute Atomic Vapor. *Science*, 269(5221):198–201, 1995.
- [27] K. B. Davis, M. O. Mewes, M. R. Andrews, N. J. van Druten, D. S. Durfee, D. M. Kurn, and W. Ketterle. Bose-Einstein Condensation in a Gas of Sodium Atoms. *Phys. Rev. Lett.*, 75(22):3969–3973, 1995.
- [28] C. C. Bradley, C. A. Sackett, J. J. Tollett, and R. G. Hulet. Evidence of Bose-Einstein Condensation in an Atomic Gas with Attractive Interactions. *Phys. Rev. Lett.*, 75(9):1687–1690, 1995.

- 
- [29] C. C. Bradley, C. A. Sackett, and R. G. Hulet. Bose-Einstein Condensation of Lithium: Observation of Limited Condensate Number. *Phys. Rev. Lett.*, 78(6):985–989, 1997.
- [30] Daniel A. Steck. Rubidium 87 D Line Data. Available online at <http://steck.us/alkalidata> (revision 2.1.4, 23 December 2010).
- [31] Jessica Reeves. *An Atom Waveguide For Interferometry With A Bose-Einstein Condensate of  $^{87}\text{Rb}$* . PhD thesis, University of Virginia, 2006.
- [32] K. B. MacAdam, A. Steinbach, and C. Wieman. A narrow-band tunable diode laser system with grating feedback, and a saturated absorption spectrometer for Cs and Rb. *Am. J. Phys.*, 60(12):1098–1111, 1992.
- [33] C. Wieman and Leo Hollberg. Using diode lasers for atomic physics. *Rev. Sci. Instrum.*, 62(1):1–20, 1991.
- [34] Harold J. Metcalf and Peter van der Straten. *Laser Cooling and Trapping*. Springer, New York, 1 edition, 1999.
- [35] J. Dalibard and C. Cohen-Tannoudji. Laser cooling below the doppler limit by polarization gradients: simple theoretical models. *J. Opt. Soc. Am. B*, 6(11):2023–2045, 1989.
- [36] Pierre Meystre. *Atom Optics*. Springer, New York, 2001.
- [37] W. Ketterle and N. J. van Druten. Evaporative Cooling of Trapped Atoms. *Advances in Atomic, Molecular, and Optical Physics*, 37:181–236, 1996.
- [38] E. Majorana. Atomi Orientati in campo magnetico variabile. *Il Nuovo Cimento*, 9:43, 1932.
- [39] D. E. Pritchard. Cooling Neutral Atoms in a Magnetic Trap for Precision Spectroscopy. *Phys. Rev. Lett.*, 51(15):1336–1339, 1983.

- 
- [40] J. J. Tollett, C. C. Bradley, C. A. Sackett, and R. G. Hulet. Permanent magnet trap for cold atoms. *Phys. Rev. A*, 51:R22–R25, 1995.
- [41] W. Petrich, M. H. Anderson, J. R. Ensher, and E. A. Cornell. Stable, Tightly Confining Magnetic Trap for Evaporative Cooling of Neutral Atoms. *Phys. Rev. Lett.*, 74(17):3352–3355, 1995.
- [42] A. Tonyushkin and M. Prentiss. Straight macroscopic magnetic guide for cold atom interferometer. *J. Appl. Phys.*, 108:094904, 2010.
- [43] S. Gupta, K. W. Muirch, K. L. Moore, T. P. Purdy, and D. M. Stamper-Kurn. Bose-Einstein Condensation in a Circular Waveguide. *Phys. Rev. Lett.*, 95:143201, 2005.
- [44] S. Wu, W. Rooijackers, P. Striehl, and M. Prentiss. Bidirectional propagation of cold atoms in a “stadium”-shaped magnetic guide. *Phys. Rev. A*, 70:013409, 2004.
- [45] Matthew B. Squires, James A. Stickney, Evan J. Carlson, Paul M. Baker, Walter R. Buchwald, Sandra Wentzell, and Steven M. Miller. Atom chips on direct bonded copper substrates. *Rev. Sci. Instrum.*, 82(2):–, 2011.
- [46] James F. Shakelford and William Alexander. *CRC Materials Science and Engineering Handbook*. CRC Press, Boca Raton, 3rd edition, 2000.
- [47] J. H. Dellinger. The Temperature Coefficient of Resistance of Copper. *Bulletin of the Bureau of Standards*, 7(1):71–101, 1910.
- [48] K. L. Baranowski and C. A. Sackett. A stable current source for magnetic traps. *J. Phys. B: At. Mol. Opt. Phys.*, 39:2949–2957, 2006.
- [49] K. J. Hughes, B. Deissler, J. H. T. Burke, and C. A. Sackett. High-fidelity manipulation of a Bose-Einstein condensate using an optical standing wave. *Phys. Rev. A*, 76:035601, 2007.

- 
- [50] M. Kozuma, L. Deng, E. W. Hagley, J. Wen, R. Lutwak, K. Helmerson, S. L. Rolston, and W. D. Phillips. Coherent Splitting of Bose-Einstein Condensed Atoms with Optically Induced Bragg Diffraction. *Phys. Rev. Lett.*, 82:871–875, Feb 1999.
- [51] N. F. Ramsey. A Molecular Beam Resonance Method with Separated Oscillating Fields. *Phys. Rev.*, 78:695–699, 1950.
- [52] Eugene Hecht. *Optics*. Addison Wesley, San Francisco, 4th edition, 2002.
- [53] Franco Dalfovo, Stefano Giorgini, Lev P. Pitaevskii, and Sandro Stringari. Theory of Bose-Einstein condensation in trapped gases. *Rev. Mod. Phys.*, 71:463–512, Apr 1999.
- [54] J. H. T. Burke, B. Deissler, K. J. Hughes, and C. A. Sackett. Confinement effects in a guided-wave atom interferometer with millimeter-scale arm separation. *Phys. Rev. A*, 78:023619, 2008.
- [55] David S. Weiss, Brenton C. Young, and Steven Chu. Precision measurement of the photon recoil of an atom using atomic interferometry. *Phys. Rev. Lett.*, 70:2706–2709, May 1993.
- [56] Sheng-wey Chiow, Sven Herrmann, Steven Chu, and Holger Müller. Noise-Immune Conjugate Large-Area Atom Interferometers. *Phys. Rev. Lett.*, 103:050402, Jul 2009.
- [57] Malo Cadoret, Estefania de Mirandes, Pierre Cladé, Saïda Guellati-Khélifa, Catherine Schwob, François Nez, Lucile Julien, and François Biraben. Combination of Bloch Oscillations with a Ramsey-Bordé Interferometer: New Determination of the Fine Structure Constant. *Phys. Rev. Lett.*, 101:230801, Dec 2008.
- [58] M. Horikoshi and K. Nakagawa. Suppression of Dephasing due to a Trapping Potential and Atom-Atom Interactions in a Trapped-Condensate Interferometer. *Phys. Rev. Lett.*, 99(18):1080401, 2007.

- 
- [59] T. L. Gustavson, A. Landragin, and M. A. Kasevich. Rotation sensing with a dual atom-interferometer Sagnac gyroscope. *Class. Quantum Grav.*, 17:2385–2398, 2000.
- [60] T. Kovachy, S. Chiow, and M. A. Kasevich. Adiabatic-rapid-passage multiphoton Bragg atom optics. *Phys. Rev. A*, 86:011606, 2012.